UNIVERSITY OF CALIFORNIA, SAN DIEGO

# Aerosol Measurements with Laser-Induced Breakdown Spectroscopy

A dissertation submitted in partial satisfaction of the

requirements for the degree Doctor of Philosophy

in

Engineering Sciences (Mechanical Engineering)

by

Gregg Arthur Lithgow

Committee in Charge:

Professor Steven Buckley, Chair
Professor Farhat Beg
Professor Kimberly Prather
Professor Lynn Russell
Professor George Tynan

2007

The dissertation of Gregg Arthur Lithgow is approved, and it is acceptable in quality and form for publication on microfilm:

_____

_____

_____

_____

_____

Chair

University of California, San Diego

2007

TABLE OF CONTENTS

LIST OF FIGURES

LIST OF TABLES

ACKNOWLEDGEMENTS

I sincerely thank my advisor, Steven Buckley, for all of the help and support he has provided during my graduate career. When he personally called me to discuss the possibility of joining his group - before I had even been accepted to graduate school - I knew that he would be a special person to work with. I'm particularly grateful for his knack for finding ways to make life as a graduate student easy, so that all I had to worry about was my work.

I have been fortunate to work with many wonderful and talented people at the University of Maryland, and the University of California, San Diego. I would like to thank Ali Rangwala, Mohamadreza Gharavi, Erin Simpson, Zuhair Ibrahim, Jayakumar Patil, Sivasankar Pandetti, Francesco Ferioli, Melanie Zauscher, Craig Wildman, Kyle Kratszch, Sam Krehnbrink, Diogo Bolster, Bruce Thomas, Nancy Bastian, Bruno Etchepare, and the members of my committee, for the many ways that have helped my work and enriched my life.

I would like to thank my parents, Jane and David, and brothers, John and Jay, for being the best family any kid could wish for. Their love, support, and guidance have made me who I am today. Finally, I thank Marie Sohsman for balancing me so well and loving me so much.

Chapter 3, in full, is a reprint of material as it appears in Applied Spectroscopy, vol. 57, no. 10, p. 1207, 2003, Hybl, J., Lithgow, G.A., and Buckley, S.G.

Chapter 4, in full, is a reprint of material as it appears in Atmospheric Environment, vol. 38, no. 20, p. 3319, 2004, Lithgow, G.A., Robinson, A.L., and Buckley, S.G.

Chapter 5, in full, is a reprint of material as it appears in Applied Physics Letters, vol. 87, no. 1, art. no. 011501, 2005, Lithgow, G.A., and Buckley, S.G.

Chapter 6, in full, is a reprint of material as it appears in Spectrochimica Acta Part B, vol. 60, nos. 7-8, p. 1060, 2005, Lithgow, G.A., and Buckley, S.G.

## VITA

| | |
|---|---|
| 1999 | Bachelor of Science, Bucknell University |
| 2001-2003 | Research Assistant, University of Maryland, College Park |
| 2003-2007 | Research Assistant, Teaching Assistant,<br>University of California, San Diego |
| 2005 | Candidate in Philosophy, University of California, San Diego |
| 2007 | Doctor of Philosophy, University of California, San Diego |

## PUBLICATIONS

J. Hybl, G.A. Lithgow, and S.G. Buckley, "Laser-Induced Breakdown Spectroscopy Detection of Biological Aerosols," Applied Spectroscopy, vol. 57, issue 10, pp 1207-1215 (2003).

G.A. Lithgow, A.L. Robinson, and S.G. Buckley, "Ambient Measurements of Metal-Containing PM 2.5 in an Urban Environment Using Laser-Induced Breakdown Spectroscopy," Atmospheric Environment, vol. 38, issue 20, pp 3319-3328 (2004).

G.A. Lithgow and S.G. Buckley, "Effects of Focal Volume and Spatial Inhomogeneity on Uncertainty in Single-Aerosol Laser-Induced Breakdown Spectroscopy Measurements," Applied Physics Letters, vol. 87, issue 1, article no. 011501 (2005).

G.A. Lithgow and S.G. Buckley, "Influence of Particle Location Within Plasma and Focal Volume on Precision of Single-Particle LIBS Measurements," Spectrochimica Acta. Part B, vol. 60, issue 7-8, pp 1060-1069 (2005).

ABSTRACT OF THE DISSERTATION

Aerosol Measurements with Laser-Induced Breakdown Spectroscopy

by

Gregg Arthur Lithgow

Doctor of Philosophy in Engineering Sciences (Mechanical Engineering)

University of California, San Diego, 2007

Professor Steven Buckley, Chair

Laser-Induced Breakdown Spectroscopy (LIBS) is a fast and simple analytic technique that is finding use in a range of applications. With LIBS, a pulsed laser of sufficient energy is focused to a spot, at which point the material is ionized and heated to temperatures in excess of 15,000 K. Light from this laser-induced plasma is then collected into a spectrometer and analyzed. LIBS is an extremely versatile technique that may be used to analyze virtually any material and deployed in even the harshest environments. Recently, interest in the technique has been rapidly expanding and many new applications have been developed. One area that has received relatively little attention is the measurement of aerosols. In this work, attempts at two applications of LIBS for aerosol measurements are presented, along with a fundamental investigation of sources of uncertainty unique to aerosol measurements.

In the first application, LIBS is examined as a potential method for detecting airborne biological agents. Laboratory measurements of some common biological agent simulants are compared to those of common, naturally occurring biological aerosol

components (pollen and fungal spores) to determine the potential of LIBS for discriminating biological agents from natural background aerosols. In the second application, metal species in ambient particulate matter were continuously monitored during a week-long field trial. Average and temporally resolved concentrations of seven metals were measured, and individual particles containing multiple species were detected.

After attempting several new applications, it was discovered that previously unknown effects unique to aerosol measurements introduce significant uncertainty into the LIBS signal, which substantially limit the usefulness of the technique. A fundamental investigation is presented that identifies the location of individual particles within the LIBS plasma as a significant source of uncertainty. Several experiments and modeling efforts demonstrate that the optical systems typically used in LIBS devices do not collect light uniformly across the plasma volume, and that these optical effects dominate other phenomena contributing to the final signal. Finally, methods of improving the performance of LIBS aerosol measurements by changing the optical design or introducing a particle triggering system to reduce the variation in particle location are discussed.

# 1. INTRODUCTION

Laser-induced breakdown spectroscopy (LIBS), also known as laser-induced plasma spectroscopy, is emerging as a powerful spectrochemical analysis technique with a wide range of applications. With LIBS, a focused laser pulse is used to vaporize and ionize a sample of material, creating a luminous plasma. Light from the laser-plasma is collected into a spectrometer, resolved by wavelength, and recorded with a detector. Because of its attractive characteristics, interest in the technique has rapidly spread in recent years. In some applications, LIBS offers an improvement over traditional analytical techniques. In other cases, LIBS is finding use in places where no other instruments are suitable. The measurement of aerosols is one application where LIBS could prove to be very useful. LIBS may be used to measure the elemental composition of individual submicron particles in real-time and in difficult environments *in situ*. The possibility of opening new scientific and commercial opportunities has generated much excitement about the technique.

LIBS offers a unique combination of versatility, simplicity, speed and economy. There are many chemical analysis techniques in use for scientific and industrial applications and for each application the relative merits of LIBS must be evaluated case by case. Generally speaking however, the strengths of LIBS can be stated on their own. LIBS is an atomic emission technique that can be used for detection of essentially any element. Virtually any material can be analyzed, whether originally in solid, liquid or

gaseous states. In many cases, no sample preparation is required and samples can be any size or shape, including powders and aerosols. LIBS devices are relatively simple, can be made robust and portable, and can be deployed in harsh environments. Only optical access to the sample is required, and measurements can be made from distances of tens of meters. Data analysis is rapid and the operation of a LIBS instrument can be automated. LIBS devices can be inexpensive compared to some techniques, and they use no solvents or filters. With these attractive characteristics, applications of LIBS will surely continue to grow during the foreseeable future.

### 1.1 The Development of LIBS

The advent of the laser, the first of which was built by Maiman in 1960 [1], was the fundamental breakthrough that enabled the development of LIBS. Considering the great scientific importance of the laser and the many useful technologies that it has spawned, it is interesting to note that LIBS was one of the first areas where the laser was applied. Within two years, Brech and Cross [2] reported that a laser pulse focused on a surface would vaporize material and create a plasma that could be used for spectroscopic analysis. They were primarily interested in using the laser to vaporize material to be analyzed with an electric spark spectrometer, but their work contained the elements of what would come to be known as LIBS. From that point, interest spread quickly as a number of researchers began investigating the phenomenon. In 1963, Debras-Guedon and Liodec [3] recognized explicitly that the laser pulse alone was sufficient to vaporize and excite solid material for spectrochemical analysis without the use of an electrode spark. The same year, Meyerand and Haught [4] and Marker *et al*. [5] first observed laser-plasmas in gases. In 1964, Runge *et al*. produced linear calibrations for

measurements of nickel and chromium concentrations in samples of stainless steel [6]. Although the basic concept of the technique was fully realized by this point, there were many details to be worked out before useful, quantitative measurements could be made.

Interest in laser-plasmas quickly spread during the early 1960's. Much work was dedicated to understanding the basic physics of the process. A main area of interest was understanding the mechanisms by which high intensity laser light causes dielectric breakdown of gases that are transparent at lower intensities [7-11]. There were also many experiments studying the characteristics of the plasmas generated by gas breakdown [12-15]. Others looked into the vaporization mechanisms and properties of plasmas created from solid surfaces [16-18]. Many of these researchers were interested in the fundamental physics of the phenomena and were not necessarily concerned with using it as a chemical analysis technique. These fundamental processes are complicated and continue to be studied today.

Researchers also continued to explicitly pursue spectroscopic measurements with laser-plasmas. For example, Runge *et al*. measured molten metal in a furnace and touted the ability to make measurements in harsh environments [19]. In a review paper in 1968, Margoshes and Scribner were impressed with the rapidly growing use of laser plasmas for analysis [20]. During the later half of the decade however, limitations of the technique started to become apparent, and LIBS could not compete with other analytic techniques. In 1967, Rasberry *et al*. found difficulty making quantitative measurements of metals [21,22]. Plagued by poor detection limits and lack of quantitative ability, the analytical community turned its focus more towards the fundamental questions of

vaporization and plasma plume expansion, and how they affected the resulting emission spectra [23, 24].

Progress was incremental until researchers at Los Alamos National Labs made important breakthroughs in the 1980's. Along with coining the acronym LIBS [25], Loree and Radziemski made use of newly available, much improved optical detectors to record time-resolved spectra [26]. This was a crucial development that allowed for significant improvement in the performance of the technique. During the previous years, spectra had been recorded with photographic plates, streak cameras, or photomultiplier tubes (PMT). With these methods, it was not possible to record a full spectrum from a single laser shot with micro-second temporal resolution. By using a photodiode array with a multichannel plate (MCP) intensifier, Loree and Radziemski were able to record a full spectrum with high temporal resolution. They found that at early times the spectra were dominated by a bright continuum background and broadened ionic lines. At longer delay times, the background reduced and sharp neutral lines became visible, resulting in a greatly improved signal.

Led by Radziemski and Cremers, the Los Alamos group took advantage of their improved LIBS device and published a series of important papers during the 1980's. They were primarily interested in detecting and monitoring hazardous materials used in Los Alamos laboratories and found success with LIBS. They were able to detect beryllium aerosol particles [27], chlorine and fluorine in air [28], and uranium and other metals in liquid solutions [29,30]. They also worked on designing instruments that could be used in difficult environments. They built a portable a device that could sample material from several meters away [31], and incorporated fiber optics for ease of use [32].

The work at Los Alamos helped to revive interest in LIBS, and as research efforts increased during the 1990's, successful applications proliferated. The most successful and widespread application has been in measuring the composition of solid metals. The quantitative performance is now competitive with other techniques [33-35]. Due to its speed and simplicity, LIBS has found success as an on-line process monitor in the steel industry [36]. In 1993, Aragon *et al*. made quantitative measurements of molten steel in a furnace, fulfilling the promise made by Runge almost thirty years earlier [37]. The versatility of LIBS has also brought it to the fore for applications in harsh environments. For example, LIBS has been used to identify archeological artifacts under seawater [38,39], and to measure corrosion on heat exchanger tubes in the superheater of a nuclear power plant [40]. The use of LIBS in space exploration has been investigated [41], and the next Mars Rover is scheduled to carry a LIBS device that will be able to remotely identify the composition of rocks within a five meter radius of the vehicle.

At present, LIBS has reached an intermediate stage of maturity. A number of applications have become well established and there are several commercially packaged instruments on the market. However, ever better performance is demanded even in the most well established applications, and progress is limited because the fundamental processes of material ablation and plasma formation are still not fully understood. The laser-material, laser-plasma, and plasma-material interactions are non-linear processes with a large number of variables. There is much to learn before these processes can be controlled to optimize the resulting spectroscopic signal. Furthermore, as new applications continue to develop new questions continually arise as aspects of instrument design, calibration, and data analysis need to be tailored to each application.

## 1.2 Introduction to Aerosols

Aerosol science is a broad field that spans such areas as atmospheric science, public and occupational health, and nanotechnology. An aerosol is defined as a suspension of solid particles or liquid droplets (hereafter referred to as particles) in a gas. Strictly speaking, the term aerosol refers to the system of condensed and gas phases together, but it is commonly used to refer specifically to the particles if they are of primary interest. A few examples of aerosols will be discussed, with a focus on properties of interest and whether LIBS is a suitable method for measuring those properties.

Atmospheric aerosols have important impacts on the global climate and public health. Aerosols can directly affect the atmospheric radiation balance by scattering and absorbing light, or particles can indirectly alter the Earth's albedo by serving as nucleation sites for water droplets and influencing cloud formation [42-47]. Exposure to particles in the atmosphere has also long been known to adversely affect public health [48,49] . Atmospheric aerosols are a complicated mixture of many types of particles. Some of the important components include organic and elemental carbonaceous species, sulfates, nitrates, ammonium, sea salts, heavy metals, and biological material. Aerosols are the product of both natural and man-made processes, and can be directly emitted into the atmosphere (primary aerosols) or formed in the atmosphere from gaseous precursors (secondary aerosols) [50-52].

The Earth's atmosphere is a complex system and there are many open questions related to atmospheric aerosols. The sources of primary aerosols, the formation processes of secondary aerosols, and the transport and aging of aerosols throughout their suspended

lifetime are all active areas of inquiry. Although it has long been known that aerosols cause detrimental health affects, the detailed understanding of human exposure and correlations of size and composition to morbidity and mortality endpoints are still being worked out. Finally, as understanding of the above questions improves, optimized monitoring and control methods need to be implemented to reduce the most harmful aerosols.

When measuring atmospheric aerosols, the most important characteristics are concentration, size distribution, and composition. There are two common metrics for concentration: the total mass of particulate per mass or volume of carrier gas (mass concentration), or the number of particles per volume of gas (number concentration). There are several parameters that can be used to characterize the size of particles including the mass, the physical dimension, the electrical mobility diameter, and the aerodynamic diameter. The mobility diameter is characterized by the velocity that a charged particle will move through the fluid in the presence of an electric field. The aerodynamic diameter is characterized by the particle's response to an acceleration of the surrounding fluid. For spherical particles of unit density, the physical, mobility, and aerodynamic diameters are equivalent. However, the mobility diameter is a function of the shape of the particle and the aerodynamic diameter is a function of both the shape and density. Aerosols often have complicated shapes and significantly vary in density, so care must be used when characterizing their size. The aerodynamic diameter is most often the significant size parameter governing the motion of aerosols. Other important properties of atmospheric aerosols include shape, surface characteristics and optical properties.

A second interesting class of aerosols are biological aerosols. There is acute interest in developing systems that can continuously monitor and rapidly detect biological aerosols following the 2001 anthrax attacks. To be effective, a device must be able to monitor particles in ambient air and distinguish pathogens from the complicated atmospheric background described above, including non-pathogenic biological aerosols. Definitive identification typically involves a wet-chemistry protein detection that cannot be used as a continuous monitoring device. Therefore, a device that could run continuously and rapidly identify suspicious particles would be useful as a warning trigger for a more elaborate and conclusive technique. Additional bioaerosol detection applications include monitoring disease-causing bacteria in hospitals or allergy-causing pollen and mold. The relevant characteristics of biological aerosols are very different than other aerosols. Biologically important features such as genetic sequences and protein structures are responsible for the infectious and toxic qualities of biological aerosols. However, some differences in elemental composition have been observed in biological organisms, and may possibly be used for rough classifications.

Finally, aerosols are important in a number of industrial settings. Materials pass through an aerosol stage in the manufacturing processes of optical fibers, ceramic powders, semiconductor devices, and other high tech products. In many cases, the quality of the end product depends on carefully controlling the aerosol properties during the manufacturing processes. Aerosol measurements are necessary for characterizing the aerosol production methods in these processes or for on-line process control. Additionally, monitoring the levels of toxic aerosols is important in many occupational settings. In industrial applications, the aerosols tend to be much simpler than the cases

described above because they are produced and controlled for a specific purpose in a confined space. However, instrument design can be a significant challenge when dealing with confined spaces, high temperatures, need for automation and rapid feedback, and other aspects of industrial processes.

### 1.3 Aerosol Measurement Techniques

There are countless kinds of aerosols with many different properties of interest. There are a correspondingly large number of instruments used to measure aerosols. The array of aerosol instruments have been discussed in detail in numerous books and review articles [53-62]. The discussion here will be limited to compositional analysis techniques, since that is the category that LIBS falls into. Also, it should be noted that some instruments are combinations of several techniques, allowing them to simultaneously measure multiple properties. LIBS lends itself to this strategy also. For example, it is possible to include an aerodynamic sizing device into the particle sampling apparatus of a LIBS system, allowing simultaneous size and composition measurements.

Measuring the composition of aerosols can be a significant challenge because they often consist of complicated, inhomogeneous mixtures of different types of particles. When measuring aerosols, either the overall composition of all the particles can be measured, the particles can be sorted and measured by size category, or the composition of individual particles can be measured. Until fairly recently, only bulk measurements of either the total aerosol, or of size-selected particles have been possible. In either of these cases, particles are typically collected onto a filter or other substrate, or into solution, then taken to an analytical instrument. With this strategy, essentially the full range of analytical techniques are available. The many varieties of mass spectrometry,

chromatography, and optical and X-ray spectroscopy can be used to measure aerosols this way. In this case, the challenge lies in controlling how the aerosols are sampled, in terms of sorting particles by size and in capturing the temporal changes of the aerosol system. Errors can be introduced as particles absorb, evaporate, or react with species while on the filter. Filter-based methods are limited in temporal resolution due to the sampling time needed to collect a sufficient number of particles. Also, the analysis can be slow because samples need to be physically moved, and sometimes chemically prepared for the analytical instrument. LIBS may be used to analyze collected particles, but the real advantage of LIBS is that it may be used for on-line, single-particle analysis.

In many applications, it is desirable to have on-line and single-particle composition measurements. On-line measurement refers to methods that perform the analysis with high temporal resolution, no sample preparation, and with minimal processing time. Sufficiently high temporal resolution is necessary to analyze short time-scale processes involved with particle formation, evolution and transport. Rapid analysis is useful for emission monitoring, occupational health monitoring, and process control. Furthermore, single-particle techniques are useful for obtaining detailed information about relationships between size and composition and for 'fingerprinting' in source identification and particle tracking. Finally, since on-line techniques sample particles directly into the instruments, errors due to particle handling and preparation are avoided.

In contrast to the variety of bulk analysis techniques, there are few on-line and single particle techniques available. An excellent review by Sullivan and Prather details the recent developments of on-line methods for atmospheric aerosols [63]. The main category of on-line instruments are based on mass spectrometry. There are several types

of single particle mass spectrometers (SPMS), distinguished mainly by the technique used to ionize the particles, such as laser desorption/ionization (LDI), two-step LDI, thermal desorption with electron ionization and chemical ionization. These instruments can measure organic and inorganic species in single particles, rapidly and with good detection limits. The science of mass spectrometry is mature and well-established. The challenge has been to adapt the technique to single-particle measurements, and much progress has been made on that front. SPMS instruments are developing rapidly and finding much success [64-68]. Demonstrating the sensitivity a single-particle aerosol time-of-flight mass spectrometer (ATOFMS), Whiteaker and Prather were able to detect pesticide residues on soil particles at the attamole level ($10^{-18}$ mole) [65], and differentiate between various pesticides. The ability to classify a large range of types of materials has also made the ATOFMS an excellent tool for source apportionment [69-72]. It will be a challenge for LIBS to match the analytical capability of these instruments. However, they do have some limitations. Mass spectrometers must draw particles into a vacuum chamber before ionization and there is significant cost, size and complexity associated with the pumping system. Ever improving instrument design will expand the versatility and portability of these systems, however, it is likely that LIBS instruments will be a more easily deployable in challenging environments.

Laser-induced fluorescence is another spectroscopic technique that can be used for on-line and single particle measurements [73]. With LIF, a short-wavelength laser is used to electronically excite species, then as the electrons relax, they emit light. With LIF, species are excited through direct absorption of photons rather than by creating plasma. Operationally, LIF is very similar to LIBS, and they are complementary

techniques. LIF is primarily used for molecular species, especially organics, while LIBS typically measures atomic composition. Because of the similarity of instrumentation and the complementary nature of their analytical abilities, it may be possible to combine LIF and LIBS into a single instrument [74].

Other on-line techniques have been proposed and are in the early stage of development. Seltzer and co-workers have used a customized ICP system to monitor metal emissions from an incinerator [75]; this process has met the EPA relative accuracy requirements and is commercially available. However, the instrument is unable to measure individual particles. Similar investigations on another continuous metals emissions monitor based on an atmospheric microwave plasma are underway by Woskov and co-workers [76]. Ondov's group at the University of Maryland has developed a wet chemistry technique called SEAS (Semi-continuous Elements in Aerosol System), in which particles of all sizes entering the instrument are grown by condensation in supersaturated water vapor, and then separated using a virtual impactor [77]. The particle-laden stream is collected in impingers, and the metal content of the wash is analyzed using an ICP or other elemental analysis method. Time-resolved samples can be collected along with corresponding meteorological data to perform source apportionment [78]. However, there is a substantial time lag between data collection and analysis using this technique as currently configured.

### 1.4 LIBS Aerosol Measurements

A number of studies have investigated aerosol measurements with LIBS, although the topic has received relatively little attention compared to other LIBS applications. The first measurements were by the Los Alamos group, who were motivated by the need to

monitor toxic metal particles to ensure the safety of workers at the laboratories [27,79,80]. Zhang *et al*., and Buckley *et al*. independently investigated LIBS as a continuous emissions monitor (CEM) for use with a rotary kiln waste incinerator [81,82]. The groups of Schechter and Panne also investigated ways of making quantitative aerosol measurements and suggested their utility for a variety of environmental and industrial applications [83,84]. Two early attempts to at single-particle measurements were made by Archontaki and Crouch [85] and Ottesen *et al*. [86], but most of the single-particle work has been done by Hahn since the late-1990's. Hahn studied the sampling statistics and strategies associated with single-particle measurements [87-89], the precision of single-particle measurements [90], the maximum size of particle that can be vaporized in a LIBS plasma [91], and used LIBS to monitor ambient particulate matter (PM) [92].

All of the above researchers expressed optimism over the potential of LIBS aerosol measurements to be useful for environmental and industrial applications. However, the usefulness for aerosol measurements has been limited by its performance. Highly quantitative measurements can be made in the laboratory with a steady, high-concentration calibrated aerosol stream when it is possible to average together many spectra. However, the sensitivity is relatively poor, especially for non-metal species and the precision is significantly reduced with single-particle measurements when spectral averaging is not possible. Therefore, the most recent work on aerosols, which will be discussed later in this manuscript, has focused on fundamentally improving the performance of the technique.

### 1.5 Contributions of this Dissertation

This dissertation addresses the use of LIBS for aerosol measurements. The intermediate stage of LIBS understanding is reflected in the progression of this manuscript. First, two attempts at new applications of aerosol measurements will be presented. Lessons learned about the limitations of the technique will then be discussed, and provide the motivation for efforts to improve the basic performance of aerosol measurements. Chapter 3 details the use of LIBS for measurements of ambient particulate matter. This expands on the previous work of Hahn by extending the number of metals monitored, selecting only fine particulate matter (particles with diameter < 2.5 μm, $PM_{2.5}$) and implementing LIBS as a continuous monitor. Chapter 4 presents the first reported use of LIBS to detect biological aerosols. The remaining chapters focus on experiments that identify the location of particles within the plasma volume and the focal volume of the collection optics as an important source of uncertainty in single-particle measurements. Finally, strategies for improving the performance of LIBS aerosol measurements will be discussed.

**References**

1. T.H. Maiman, Stimulated Optical Radiation in Ruby. *Nature*, vol.187, no. 4736, p. 493, 1960.

2. F. Brech, L. Cross, Optical microemission stimulated by a ruby laser. *Appl Spectrosc,* vol. 16, p. 59, 1962.

3. J. Debras-Guedon, N. Liodec, De l'utilisation du faisceau d'un amplificateur a ondes lumineuses par emission induite de rayonnement (laser a rubis), comme source energetique pour l'excitation des spectres d'emission des elements. *C.R. Acad. Sci*. vol. 257, no. 21, p. 3336, 1963.

4. R.G Meyerand, A.F. Haught, Gas Breakdown at optical frequencies. *Phys Rev Lett*, vol. 11, no. 9, p. 401, 1963.

5. P.D. Maker, R.W. Terhune, C.M. Savage, Proc. 3rd Int Conf. on Quantum Electronics. Columbia University Press, New York, pp. 1559-65, 1963.

6. E.F. Runge, R.W. Minck, F.R. Bryan, Spectrochemical Analysis Using a Pulsed Laser Source. *Spectrochimica Acta*, vol. 20, no. 4, p. 733, 1964.

7. R.W. Minck, Optical Frequency Electrical Discharges in Gases. *Journal of Applied Physics*, vol. 35, no. 1, p. 252, 1964.

8. S.A. Ramsden , P. Savic, Radiative Detonation Model for Development of Laser-Induced Spark in Air. *Nature*, vol. 203, no. 4951, p. 1217, 1964.

9. J.K. Wright, Theory of the Electrical Breakdown of Gases by Intense Pulses of Light. *Proc Phys Soc*, vol. 84, no. 1, p. 41, 1964.

10. Y.B. Zel'dovich, Y.P. Raizer, Cascade Ionization of a Gas By a Light Pulse. *Soviet Physics, JETP*, vol. 20, no. 3, p. 772, 1965.

11. B.A. Tozer, Theory of ionization of gases by laser beams. *Physical Review*, vol. 137, no. 6A, p. A1665, 1965.

12. R.G. Meyerand, A.F. Haught, Optical-energy absorption and high-density plasma production. *Physical Review Letters*, vol. 13, no. 1, p. 7, 1964.

13. S.A. Ramsden, W.E.R. Davies, Radiation Scattered from the Plasma Produced by a Focused Ruby Laser Beam. *Physical Review Letters*, vol. 13, no. 7, p. 227, 1964.

14. P. Nelson *et al.*, Experimental and theoretical studies of air breakdown by intense pulse of light. *Physics Letters*, vol. 13, no. 3, p. 226, 1964.

15. M. Young, M. Hercher, C.Y. Yu, Some characteristics of laser-induced air sparks. *Journal of Applied Physics*. vol. 37, p. 4938, 1966.

16. J.F. Ready, Development of plume material vaporized by giant-pulse laser. *Applied Physics Letters,* vol. 3, no. 1, p. 11, 1963.

17. W. Linlor, Ion energies produced by laser giant pulse. *Applied Physics Letters*, vol. 3, no. 11, p. 210, 1963.

18. N.R. Isenor, Metal ion emission velocity dependence on laser giant pulse height. *Applied Physics Letters*, vol. 4, no. 8, p. 152, 1964.

19. E.F. Runge, Spectrochemical analysis of molten metal using a pulsed laser source. *Spectrochimica acta*, vol. 22, no. 9, p. 1678, 1966.

20. M. Margoshes, B.F. Scribner, Emission Spectrometry. *Analytical Chemistry*, vol. 40, no. 5, p 223, 1968.

21. S.D. Rasberry, B.F. Scribner, M. Margoshes, Laser probe excitation in spectrochemical anlysis I: Characteristics of the source. *Applied Optics*, vol. 6, no. 1, p. 81, 1967.

22. S.D. Rasberry, B.F. Scribner, M. Margoshes, Laser probe excitation in spectrochemical anlysis II: Investigation of quantitative aspects. *Applied Optics*, vol. 6, no. 1, p. 87, 1967.

23. E.H. Piepmeier, H.V. Malmstadt, Q-Switched laser energy absorption in the plume of an aluminum alloy. *Analytical Chemistry*, vol. 41, no. 6, p. 701, 1969.

24. R.H. Scott, A. Strasheim, Laser induced plasmas for analytic spectroscopy. *Spectrochimcia Acta*, vol. 25B, p. 311, 1970.

25. T.R. Loree, L.J. Radziemski, Laser-Induced Breakdown Spectroscopy: Time Integrated Applications. *J. Plasma Chem. Plasma Proc.*, vol. 1, no. 3, p. 271, 1981.

26. T.R. Loree, L.J. Radziemski, Laser-induced breakdown spectroscopy: time-resolved applications, *J. Plasma Chem. Plasma Proc*., vol. 1, no. 3, p. 281, 1981.

27. L.J. Radziemski, D.A. Cremers, T.R. Loree, Detection of beryllium by laser-induced breakdown spectroscopy. *Spectrochimica Acta,* vol. 38B, nos. 1-2, p. 349, 1983.

28. D.A. Cremers, L.J. Radziemski, Detection of chlorine and fluorine in air by laser-induced breakdown spectrometry. *Anal. Chem.*, vol. 55, no. 8, p. 1252, 1983.

29. D.A. Cremers, L.J. Radziemski, T.R. Loree, Spectrochemical analysis of liquids using the laser spark. *Appl. Spectrosc*., vol. 38, no. 5, p. 721, 1984.

30. J.R. Wachter, D.A. Cremers, Determination of uranium in solution using laser-induced breakdown spectroscopy. *Applied Spectroscopy*, vol. 41, no. 6, p. 1042, 1987.

31. D.A. Cremers, The analysis of metals at a distance using laser-induced breakdown spectroscopy. *Applied Spectroscopy*, vol. 41, no. 4, p. 572, 1987.

32. B.J. Marquardt *et al.*, Novel probe for laser-induced breakdown spectroscopy and Raman measurements using an imaging optical fiber. *Applied Spectroscopy*, vol. 52, no. 9, p. 1148, 1998.

33. J.A. Aguilera, C. Aragon, J. Campos, Determination of carbon content in steel using laser-induced breakdown spectroscopy. *Applied Spectroscopy*, vol. 46, p. 1382, 1992.

34. M. Sabsabi, P. Cielo, Quantitative analysis of aluminum alloys by laser-induced breakdown spectroscopy and plasma characterization. *Appl. Spectrosc.*, vol. 49, p. 499, 1995.

35. A. Gonzalez, M. Ortiz, J. Campos, Determination of sulfur-content in steel by laser-produced plasma-atomic emission-spectroscopy. *Applied Spectroscopy*, vol. 49., p. 1632, 1995.

36. R. Noll *et al.*, Laser-induced breakdown spectrometry applications for production control and quality assurance in the steel industry. *Spectrochim. Acta Part B.* vol. 56, p. 637, 2001.

37. C. Aragon, J.A. Aguilera, J. Campos, Determination of carbon content in molten steel using laser-induced breakdown spectroscopy. *Appl. Spectrosc.*, vol. 47, p. 606, 1993.

38. A.E. Pichahchy, Elemental analysis of metals under water using laser-induced breakdown spectroscopy. *Spectrochimica Acta Part B*, vol. 52, no. 1, p. 25, 1997.

39. V. Lazic, Recognition of archeological materials underwater by laser induced breakdown spectroscopy. *Spectrochimica Acta Part B*, vol. 60, nos. 7-8, p. 1014, 2005.

40. A.I. Whitehouse *et al.*, Remote materials analysis of nuclear power station steam generator tubes by laser-induced breakdown spectroscopy. *Spectrochimica Acta Part B*, vol. 56, p. 821, 2001.

41. A.K. Knight, Characterization of laser-induced breakdown spectroscopy (LIBS) for application to space exploration. *Applied spectroscopy*, vol. 54, no. 3, p. 331, 2000.

42. J.A. Coakley, R.D. Cess, Response of the NCAR Community Climate Model to the radiative forcing by the naturally-occurring tropospheric aerosol. *J. Atmos. Sci.*, vol. 42, p. 1677, 1985.

43. R.J. Charlson *et al.*, Perturbation of the Northern Hemisphere radiative balance by backscattering from anthropogenic sulfate aerosols. *Tellus, Ser. A*, vol. 43, p. 152, 1991.

44. S. Twomey, Atmospheric Aerosols. New York : Elsevier Scientific Publishing Co., 1977.

45. B.A. Albrecht, Aerosols, cloud microphysics, and fractional cloudiness. *Science*, vol. 245, p. 1227, 1989.

46. J. Hansen, M. Sato, R. Ruedy, Radiative forcing and climate response. *J. Geophys. Res.*, vol. 102, p. 6831, 1997.

47. V. Ramanathan *et al.*, Indian Ocean Experiment: An integrated analysis of the climate forcing and effects of the great Indo-Asian haze. *J. Geophys. Res.*, vol. 106, no. D22, p. 28,371, 2001.

48. D.W. Dockery *et al.*, An association between air-pollution and mortality in 6 United States cities. *New England Journal of Medicine*, vol. 329, no. 24, p. 1753, 1993.

49. D.W. Dockery, C.A. Pope, Acute respiratory effects of particulate air-pollution. *Annual Review of Public Health*, vol. 15, p. 107, 1994.

50. S.N. Pandis *et al.*, Secondary organic aerosol formation and transport. *Atmospheric Environment Part A*, vol. 26, no. 13, p. 2269, 1992.

51. B.J. Turpin, J.J. Huntzicker, Identification of secondary organic aerosol episodes and quantitation of primary and secondary organic aerosol concentrations during SCAQS. *Atmospheric Environment*, vol. 29, no. 23, p. 3527, 1995.

52. A.L. Robinson *et al.*, Rethinking organic aerosols: Semivolatile emissions and photochemical aging. *Science*, vol. 315, p. 1259, 2007.

53. S.K. Friedlander, Smoke, dust, and haze: Fundamentals of aerosol dynamics. New York : Oxford University Press, 2000.

54. W.C. Hinds, Aerosol technology: Properties, behavior, and measurement of airborne particles. New York: Wiley, 1999.

55. D.Y.H. Pui, D.Y Liu, Aerosol generation and calibration of instruments. Minneaplolis, Minn.: University of Minnesota Press, 1978.

56. J.H. Vincent, Aerosol sampling: Science and practice. Chichester; New York: Wiley, 1989.

57. C.A. Noble, K.A. Prather, Real-time single particle mass spectrometry: A historical review of a quarter century of the chemical analysis of aerosols. *Mass Spectrometry Reviews*, vol. 19, no. 4, p. 248, 2000.

58. P.J. Ziemann, Particle mass and size measurements using mass spectrometry. *TrAC-Trends in Analytical Chemistry*, vol. 17, no. 6, p. 322, 1998.

59. J.F. de la Mora *et al.*, Differential mobility analysis of molecular ions and nanometer particles. *TrAC-Trends in Analytical Chemistry*, vol. 17, no. 6, p. 328, 1998.

60. J.F. Wildmann *et al.*, Microparticle Raman spectroscopy. *TrAC-Trends in Analytical Chemistry*, vol. 17, no. 6, p. 339, 1998.

61. S.H. Wood, K.A. Prather, Time-of-flight mass spectrometry methods for real time analysis of individual aerosol particles. *TrAC-Trends in Analytical Chemistry*, vol. 17, no. 6, p. 346, 1998.

62. D.T. Suess, K.A. Prather, Mass spectrometry of aerosols. *Chemical Reviews*, vol. 99, no. 10, p. 3007, 1999.

63. R.C. Sullivan, K.A., Prather, Recent advances in our understanding of atmospheric chemistry and climate made possible by on-line aerosol analysis instrumentation. *Analytical Chemistry*, vol. 77, p. 3861, 2005.

64. K.A. Prather, T. Nordmeyer, K. Salt, Real-time characterization of individual aerosol-particles using time-of-flight mass-spectrometry. *Analytical Chemistry*, vol. 66, no. 9, p. 1403, 1994.

65. Z. Ge, A.S. Wexler, M.V. Johnston, Laser desorption/ionization of single ultrafine multicomponent aerosols. *Environmental Science and Technology*, vol. 32, p. 3218, 1998.

66. E.E. Gard *et al.*, Direct observation of heterogeneous chemistry in the atmosphere. *Science*, vol. 279, no. 5354, p. 1184, 1998.

67. D.J. Phares, K.P. Rhoads, A.S. Wexler, Performance of single ultrafine particle mass spectrometer. *Aerosol Science and Technology*, vol. 36, no. 5, p. 583, 2002.

68. J.R. Whiteaker, K.A. Prather, Detection of pesticide residues on individual particles. *Analytical Chemistry*, vol. 75, no. 1, p. 49, 2003.

69. P.V. Bhave *et al.*, Source apportionment of fine particulate matter by clustering single-particle data: Tests of receptor model accuracy. *Environmental Science and Technology*, vol. 35, no. 10, p. 2060, 2001.

70. X.H. Song *et al.*, Source apportionment of gasoline and diesel by multivariate calibration based on single particle mass spectral data. *Analytica Chimica Acta*, vol. 446, nos. 1-2, p. 329, 2001.

71. L.S. Hughes *et al.*, Size and composition distribution of atmospheric particles in southern California. *Environmental Science and Technology*, vol. 33, p. 3506, 1999.

72. S.M. Toner, D.A. Sodeman, K.A. Prather, Single particle characterization of ultrafine and accumulation mode particles from heavy duty diesel vehicles using aerosol time-of-flight mass spectrometry. *Environmental Science and Technology*, vol. 40, no. 12, p. 3912, 2006.

73. R.G. Pinnick *et al.*, Fluorescence spectra of atmospheric aerosol at Adelphi, Maryland, USA: Measurement and classification of single particles containing organic carbon. *Atmospheric Environment*, vol. 38, p. 1657, 2004.

74. J.D. Hybl *et al.*, Laser-induced fluorescence-cued, laser-induced breakdown spectroscopy biological-agent detection. *Applied Optics*, vol. 45, no. 34, p. 8806, 2006.

75. M. Seltzer, Performance Testing of a Multimetals Continuous Emissions Monitor. *Journal of the Air and Waste Management Association*, vol. 50, no. 6, p. 1010, 2000.

76. P.P. Woskov *et al.*, Accurate and Sensitive Metals Emissions Monitoring with an Atmospheric Microwave-Plasma Having a Real-Time Span Calibration. *Waste Management*, vol. 20, nos. 5-6, p. 395, 2000.

77. C. Kidwell, J. Ondov, Development and Evaluation of a Prototype System for Collecting Sub-Hourly Ambient Aerosol for Chemical Analysis. *Aerosol Science and Technology*, vol. 35, no. 1, p. 596, 2001.

78. A. Suarez, J. Ondov, Ambient Aerosol Concentrations of Elements Resolved by Size and by Source: Contributions of Some Cyokine-Active Metals from Coal- and Oil-Fired Power Plants. *Energy and Fuels*, vol. 16, no. 3, p. 562, 2002.

79. L.J. Radziemski *et al.*, Time-resolved laser-induced breakdown spectrometry of aerosols. *Analytical Chemistry*, vol 55, p. 1246, 1983.

80. M. Essien, L.J. Radziemski, Detection of cadmium, lead and zinc in aerosols by laser-induced breakdown spectrometry. *Journal of Analytical Atomic Spectrometry*, vol. 3, p. 985, 1988.

81. H. Zhang *et al*., Laser-Induced Breakdown Spectrometry as a Multimetal Continuous Emissions Monitor. *Applied Optics*, vol. 38, no. 9, p. 1459, 1999.

82. S.G. Buckley *et al.*, Laser-Induced Breakdown Spectroscopy as a Continuous Emission Monitor for Toxic Metals in Thermal Treatment Facilities. *Waste Management,* vol. 20, p. 455, 2000.

83. X. Liang *et al.*, Absolute analysis of particulate materials by laser-induced breakdown spectroscopy. *Analytical Chemistry*, vol. 69, p. 2103, 1997.

84. R.E. Neuhauser *et al.*, On-line and in-situ detection of lead aerosols by plasma-spectroscopy and laser-excited atomic fluorescence spectroscopy. *Analytica Chimica Acta*, vol. 346, p. 37, 1997.

85. H.A. Archontaki, S.R. Crouch, Evaluation of an isolated droplet sample introduction system for laser-induced breakdown spectroscopy. *Applied Spectroscopy*, vol. 42, no. 5, p. 741, 1988.

86. D.K. Ottesen, J.C.F. Wang, L.J. Radziemski, Real-time laser spark spectroscopy of particulates in combustion environments. *Applied Spectroscopy*, vol. 43, no. 6, p. 967, 1989.

87. D.W. Hahn, W.L. Flower, K.R. Hencken, Discrete particle detection and metal emissions monitoring using laser-induced breakdown spectroscopy. *Applied Spectroscopy*, vol. 51, no. 12, p. 1836, 1997.

88. J.E. Carranza, D.W. Hahn, Sampling statistics and considerations for single-shot analysis using laser-induced breakdown spectroscopy. *Spectrochimica Acta Part B*, vol. 57, p. 779, 2002.

89. J.E. Carranza, D.W. Hahn, Conditional data processing for single-shot spectral analysis by use of laser-induced breakdown spectroscopy. *Applied Optics*, vol. 42, no. 30, p. 6022, 2003.

90. D.W. Hahn, Laser-induced breakdown spectroscopy for sizing and elemental analysis of discrete aerosol particles. *Applied Physics Letters*, vol. 72, no. 23, p. 2960, 1998.

91. J.E. Carranza, D.W. Hahn, Assessment of the upper particle size limit for quantitative analysis of aerosols using laser-induced breakdown spectroscopy. *Analytical Chemistry*, vol. 74, p. 5450, 2002.

92. J.E. Carranza *et al.*, On-line analysis of ambient air aerosols using laser-induced breakdown spectroscopy. *Spectrochimica Acta Part B*, vol. 56, p. 851, 2001.

# 2. FUNDAMENTALS OF LIBS

Although the operation of a LIBS device is relatively simple, the underlying phenomena involved with the technique are quite complicated. After many years of development, it remains difficult to make quantitative measurements with LIBS. This difficulty is due to the fact that the complex process of the plasma formation is not fully understood and cannot be easily controlled. One example of the challenges encountered with aerosol measurements is the probabilistic nature of the location of the particles within the surrounding gas. When the laser-plasma is formed, the initial ionization process depends on whether it occurs in the gas or on the surface of a particle. Once initiated, the growth of the plasma involves a non-linear avalanche effect in which a small difference in the initial conditions can have a large effect on the final state of the system. The final properties of the plasma ultimately affect the features of a LIBS spectrum and the resulting measured signal.

This Chapter will introduce some of the basic processes of the plasma formation and their effects related to emission spectroscopy. Also, the components of a LIBS instrument will be briefly discussed, with a focus on what features are important when designing a LIBS apparatus for aerosol measurements. The discussion here is a brief overview of the phenomena essential to the LIBS aerosol measurements. More detail may be found in many texts addressing emission spectroscopy [1-7], plasmas [8-17], and laser-matter interactions [19-22]. Additionally, two recent books devoted to laser-induced breakdown spectroscopy [23,24] provide overviews of the fundamental

processes of LIBS and include details of instrument design and experimental methods for many applications.

**2.1 Fundamental Processes**

LIBS is an atomic emission spectroscopy technique, whereby the elemental composition of a material is determined by identifying characteristic wavelengths of light emitted by the material. For emission to occur, the material must be vaporized, dissociated into elemental form, and electronically excited. Once an excited state has been reached, high-energy electrons will spontaneously decay to a lower energy state, emitting light of a characteristic wavelength. The identification of elements present in a material is often quite simple with LIBS, however, quantification of the relative or absolute amounts of each element is more difficult. If done properly, the quantity of each element may be determined by the intensity of the spectral lines. To optimize the performance of LIBS, it is necessary to bring material to a state favorable for strong emission, and this process must be reliable and repeatable.

With LIBS, the laser provides energy for the vaporization, dissociation, and excitation of the analyte. The energy transfer may proceed through several paths that may occur sequentially or simultaneously. For example, when making aerosol measurements, the energy required to vaporize a solid particle may be transferred through direct absorption of monochromatic laser light, by impingement of a shock wave at the edge of an expanding plasma, through absorption of broadband radiation from the plasma, or through conduction from the plasma. Furthermore, due to the high energy transfer rates and the possibility of resonant processes, the state evolution may be non-equilibrium. Finally, all of these processes depend on the properties of the material itself.

To improve the performance of LIBS, it is necessary to more fully understand the relationship of the plasma formation to the many parameters involved, and to develop strategies to control those parameters that affect the resulting spectral signal.

### *2.1.1 Plasma Formation*

The formation of a laser-induced plasma typically follows an avalanche, or cascade, process [23]. It begins with the generation of a few initial free electrons and ions in the focal volume of the laser. Subsequently, the free electrons absorb laser photons providing energy for the growth of the plasma. The initial free electrons may be generated by several different processes. In pure air, and for laser wavelengths from the ultraviolet (UV) to near infra-red (NIR), the ionization potential of the gas molecules is greater than the photon energy. Therefore, free electrons are produced by multiphoton ionization, whereby a bound electron is ionized by absorbing several photons almost simultaneously. This is generally not a resonant process and the photon energy need not match any electronic transition. Significant multiphoton ionization will only occur at irradiances above a certain threshold. The breakdown threshold depends on the pressure and composition of the gas, and the wavelength of the laser, but typical values for air at atmospheric pressure are on the order of $10^{10}$ W $cm^{-2}$ [23,24]. If the air has impurities with low ionization potential, such as organic vapors or non-conductive particles, electrons may be ejected by single photon ionization, and the rate of free electron production can be significantly larger than for multiphoton process, thus reducing the breakdown threshold. Plasma initiation is most rapid when conductive particles are present in the gas, with free electrons immediately available to absorb laser energy.

The photon absorption cross-section of free electrons and ions is higher than the initial gas and the avalanche effect proceeds as the free electrons gain kinetic energy by absorption of laser energy (free-free, inverse Bremsstrahlung). The energetic electrons then heat and ionize the neighboring gas through collisions, generating more electron-ion pairs which further absorb laser energy. The initial ionization forms a hot plasma kernel that will preferentially grow towards the laser as it absorbs laser energy, but will also expand in all directions due to its increased pressure. As the pressure increases further, a shock wave develops which heats the gas rapidly as it propagates. The shock wave itself will ionize gas as it propagates, further providing electrons for laser absorption.

The propagation of the plasma front towards the laser have been modeled in several ways [22, 23, 25-29]. In the laser-supported detonation (LSD) model, the expansion of the plasma produces a strong shock wave that heats and ionizes the gas in front of the plasma, which then becomes optically thick and absorbs laser energy, further supporting the shock front. With the laser-supported radiation wave (LSR) model, the dominant mechanism of energy transfer is through radiation from the plasma itself. The plasma radiation is strong enough to heat and ionize the gas in front of it, which then absorbs the incoming laser light. Finally, in the laser-supported combustion (LSC) model both of the above mechanisms are included. At low laser irradiance above the breakdown threshold, the LSD model is more appropriate. At high irradiance, the LSR model better describes the plasma expansion. The propagation and ionization of the shock wave away from the laser beam is described by a Taylor-Sedov blast wave [25].

### *2.1.2 Material Ablation and Transport*

Perhaps the least well-characterized aspect of LIBS, especially with aerosol measurements, is the vaporization and ablation of solid material. It has been observed that the vaporization time of particles of interest are comparable to the lifetime of the LIBS plasma, and the maximum size particle that can be fully vaporized is on the order of several micrometers [30-32]. As will be discussed in Chapters 5, 6, and 7, it has also been observed that mass transport length scales are smaller than the dimensions of the plasma, and material vaporized from a particle remains localized in a region near its original position. Understanding the processes of particle vaporization and transport, and learning how to control them properly, is the most important step towards improving the performance of LIBS aerosol measurements.

At relatively low power densities, less than approximately $10^6$-$10^8$ W cm$^{-2}$, material remains in quasi-equilibrium as it is heated, and has a well defined temperature [23,24]. In this case, the phase transformations, including melting, boiling and vaporization, are well described by classical thermodynamics. Material is vaporized from the surface and the vapor will have defined temperature and kinetic energy distribution. One undesirable feature of this type of vaporization is that fractionation may occur, where different elements are vaporized at different rates depending on their volatility. Another drawback is that this process can be relatively slow, and the total amount of material that can be vaporized during the finite lifetime of the plasma is less than with higher power density processes. However, the peak intensity of the focused laser pulses used in LIBS typically exceeds $10^{10}$ W cm$^{-2}$. At such high laser intensity, the absorption of photons by inverse Bremsstrahlung, photo-ionization, and photo-dissociation result in a non-equilibrium state of the material during the laser pulse. In this

case, material is rapidly heated above boiling point, at a depth corresponding to the optical penetration, and a volume of bulk material will undergo phase explosion [24, 33, 34]. Material ejected from the surface in this manner may not initially have a well defined temperature. This type of ablation has the advantages that phase transformation may occur more quickly and fractionation may be reduced.

Once material is vaporized, it is transported both by bulk fluid motion and by diffusion. Early on as the shock wave is propagating, the rapid fluid expansion will dominate. However, the vaporization of aerosol particles often continues well after the passage of the shock wave, and diffusion plays an important role in transport of the material in latter stages of the plasma evolution. Again, when considering aerosol measurements, the transport processes are highly dependent on the time-history of the temperature and motion of the plasma specifically surrounding the particle. With aerosols, both the vaporization and transport of particle material depends on the location of the particle with respect to the incident laser beam and the developing plasma. Understanding these processes in detail is challenging, but it is also crucial to the progress of LIBS aerosol measurements.

*2.1.3 Plasma Emission*

Within a local region of plasma, if collisional processes are sufficiently rapid, it may be said to be in local thermodynamic equilibrium (LTE). This is true even if there are spatial and temporal gradients such that the overall plasma is not in equilibrium. A state of LTE implies that the particles follow the Maxwell velocity distribution, Boltzmann electronic excitation distribution, and the Saha ionization distribution [17]. In this case radiative processes are not necessarily in equilibrium, so the rate of de-

excitation of electrons through spontaneous emission is not generally balanced by the reverse process of excitation through absorption. This is important because the intensity of emission from a specific electronic transition depends on the population of electrons at the specified energy level. In LTE, the radiative de-excitation will be balanced by collisional excitation, and the emission of a given transition will depend only on the plasma temperature and density. If LTE is not maintained, the electronic population, and hence the emission, will depend on the time history of the excitation and de-excitation processes.

A number of studies suggest that LIBS plasmas [35-37] approach LTE during the time scales when emission measurements are made. Assuming local thermodynamic equilibrium, the intensity of a specified atomic emission line will depend only on the concentration of the element, the temperature of the plasma and the electron density. Even if LTE holds however, there may be spatial gradients in both the plasma properties (temperature and electron density), and the concentration of the vaporized particle material that is to be measured. In fact, measurements of temperature and electron density have demonstrated that gradients exist in LIBS plasmas [36] and evidence for localized distribution of the vaporized particle material will be presented in later Chapters. This implies that, though necessary, LTE is not sufficient to ensure a repeatable LIBS signal.

Aside from difficulty in achieving repeatable plasma properties and analyte concentrations, there are several factors that interfere with the measurement of a specified atomic emission line. There are several broadening mechanisms, including Stark broadening, Doppler broadening, and instrument broadening associated with the

spectrometer, that cause uncertainty in the wavelength of the emitted light. In some cases, this broadening is not problematic. However, if there are several emission lines closely spaced, they can overlap due to broadening, and distinguishing each may be difficult. In addition to the atomic lines, the plasma emits a bright, broadband background due to Bremsstrahlung radiation and electron-ion recombination. These broadband emissions are particularly strong at early times when the electron density and temperature are high. The bright background, and the noise it causes in a measured spectrum, can make it difficult to measure weak atomic emissions. Finally, some atoms may recombine to form molecules such as CN in the plasma. These molecules may emit electronic-vibrational emission bands that can interfere with the atomic emissions of interest. The lifetime of the LIBS plasma and associated emission is typically on the order of tens of microseconds, and an additional challenge in optimizing the LIBS signal is to select an appropriate time interval for collecting signal when the atomic emissions of interest are maximized and the background interference is minimized.

## 2.2 The LIBS Apparatus

### *2.2.1 Laser*

The role of the laser in a LIBS system is to provide energy to ionize, vaporize, dissociate, and excite analyte material. The one essential characteristic of the laser is that, when focused, it must achieve a peak intensity above the breakdown threshold of the material sampled. The breakdown threshold is the laser intensity at which the material will be substantially ionized, and a plasma formed. The fundamental process of plasma formation is depends on the wavelength of the laser, the total pulse energy, and the temporal and spatial profiles of the beam intensity. When designing a practical system,

factors such as size, weight, power and cooling requirements, robustness, and expense are also important considerations. The most common type of laser used in LIBS is the Q-switched Nd:YAG (neodymium doped yttrium aluminum garnet), at either the fundamental, second, third, or fourth harmonic frequency, and pulse widths on the order of 10 ns. Other commonly used lasers include excimer and $CO_2$ lasers. There have been a number of studies on the effects of various laser parameters [38], but it is still an active area of inquiry. A recently developed variation of LIBS, called double-pulse LIBS, uses two separate laser pulses [39,40]. The general idea is that the material ablation is achieved with the first laser pulse and the second pulse serves to heat the plasma to optimum conditions for emission, so that greater control over each process may be achieved. Often an ultraviolet pulse is used for material ablation and a near-infrared pulse is used for plasma heating. Additionally, recent work has suggested that the use of short-pulse lasers, on the order of picoseconds ($10^{-12}$ s) to femtoseconds ($10^{-15}$), may improve the performance of LIBS [41,42]. The effects of various laser characteristics is an important, ongoing area of LIBS research, however it is somewhat restricted by the expense and limited selection of lasers available.

*2.2.2 Spectrometer and Detector*

To measure atomic emissions, a method of resolving light emitted from the plasma by wavelength is combined with a device to detect the amount of light of a given wavelength. The most common devices used to resolve the wavelength are diffractive grating based systems such as the Czerny-Turner or Echelle spectrometers. Other types of monochrometers or line filters may also be used to resolve the light, but are less common in LIBS applications. The important characteristics of the spectrometer are the

resolving power and spectral range. Most elements have atomic emissions in the ultraviolet to near-infrared range (200-1000 nm). With Czerny-Turner spectrometers, there is a trade-off between the resolution and the spectral range that is possible. An appropriate spectral window must be selected which contains emission lines from the element of interest. In some cases it is necessary to change spectral windows in order to measure different elements. The more recently developed Echelle spectrometers can achieve both high resolution and wide spectral range, and are becoming more widely used in the LIBS community. The disadvantage of Echelle systems is that they are generally not as sensitive as, and are slower than, Czerny-Turner systems.

There are a number of optical detectors used in LIBS systems. The essential feature of an optical detector is that the timing can be controlled on the order of microseconds or faster, either integrating signal over a fixed time interval, or measuring a time-trace. This temporal resolution is necessary because of the timescales of the evolution of the plasma discussed above. The most common detectors used in LIBS are the charged coupled device (CCD) and intensified CCD (ICCD). CCD devices consist of an array of pixels so that many channels can be used to measure different wavelengths of light. The resolution of the measured spectrum thus is a function of the dispersion of the spectrometer, and the pixel size of the detector. Photomultiplier tubes are used occasionally as well, and have the advantages of high sensitivity, fast response, and low noise. However, they are relatively large and only several channels may be measured simultaneously, rather than a complete spectrum.

### *2.2.3 Optics*

The optical components in a LIBS system serve to focus the laser pulse onto the surface, or within the bulk, of the material to be analyzed, and also collect light from the plasma into the spectrometer. The greatest diversity encountered in LIBS devices involves the optical components and arrangements used. There are many different configurations reported in the literature, incorporating spherical lenses, aspheric lenses, broadband metallic mirrors, narrowband dichroic mirrors, optical fibers and other components. This is largely due to the fact that optical systems are tailored to a wide range of different applications. Unfortunately, in much of the literature, only the basic configurations of the optical systems are described, and occasionally important details are omitted.

To focus the laser, usually a single lens, or a simple combination of a few lenses is used. If spherical lenses are employed, the spot size will be limited by spherical aberration, whereas diffraction-limited performance can be achieved with the use of aspheric lenses. It is important to use lenses that can withstand the peak intensity of the laser pulse, and when operating in dirty environments, it may be necessary to use purge gas or some other method to keep the optics clean. In some applications, an autofocusing device may be used to account for changing distances to the sample surface, or the laser may be delivered through an optical fiber to difficult to access locations.

Collecting light from the plasma tends to be somewhat more challenging than focusing the laser, and there are many configurations used in LIBS systems. Systems often include lenses, mirrors and fiber optics, and the overall size and geometry is generally constrained by the particular application. In some applications, optical access to the sample is limited, so that the laser introduction and emission collection must be

performed on the same path. In this case, the optical paths may be separated with a pierced mirror, a dichroic mirror, a bifurcated fiber bundle, or another technique. Even without geometric constraints, the throughput of the optical system is limited by the entrance size and F-number of the spectrometer. With such a limit, there may be a need to balance between the solid angle that can be collected from the plasma, and the size of the focal volume. Additional factors such as chromatic aberrations of refractive lenses can be significant when measuring emission lines over a range of wavelengths. As will be discussed further in Chapter 7, if care is not taken when designing the optical system, the performance of the LIBS device may be significantly impaired.

**References**

1. S. Svanberg, Atomic and molecular spectroscopy : basic aspects and practical applications. Berlin; New York : Springer, 2004.

2. I.I. Sobel'man, Atomic spectra and radiative transitions. Berlin; New York : Springer-Verlag, 1992.

3. J.W. Robinson, Atomic spectroscopy. New York : M. Dekker, 1990.

4. V.P. Shevel'ko, Atoms and their spectroscopic properties. Berlin ; New York : Springer, 1997.

5. J.M. Hollas, Basic atomic and molecular spectroscopy. New York : Wiley-Interscience, 2002.

6. E.H. Evans (Editor), An introduction to analytical atomic spectrometry. Chichester ; New York : John Wiley, 1998.

7. P.F. Bernath, Spectra of atoms and molecules. Oxford ; New York : Oxford University Press, 2005.

8. H.V. Boenig, Fundamentals of plasma chemistry and technology. Lancaster : Technomic Pub. Co., 1988.

9. S. Vepřek , M. Venugopalan (Editors), Plasma chemistry. Berlin ; New York : Springer-Verlag, 1980.

10. W. Lochte-Holtgreven, Plasma diagnostics. New York : AIP Press, 1995.

11. I.H. Hutchinson, Principles of plasma diagnostics. Cambridge ; New York : Cambridge University Press, 2002.

12. H.A. Boldis *et al.,* Laser plasma theory and simulation. Chur, Switzerland ; Langhorne, Pa. : Harwood Academic, 1994.

13. F.F. Chen, Lecture notes on principles of plasma processing. New York : Kluwer Academic/Plenum Publishers, 2003.

14. R.O. Dendy, Plasma dynamics. Oxford, England: Clarendon Press ; New York : Oxford University Press, 1990.

15. D.C. Montgomery , D.A. Tidman, Plasma kinetic theory. New York : McGraw-Hill, 1964.

16. M.A. Lieberman , A.J. Lichtenberg, Principles of plasma discharges and materials processing. New York : Wiley, 1994.

17. G.V. Marr, Plasma spectroscopy. Amsterdam; New York : Elsevier Pub. Co., 1968.

18. J.C. Miller, R.F. Haglund, Jr. (Editors), Laser ablation and desorption. San Diego : Academic Press, 1998.

19. J.C. Miller (Editor) Laser ablation : principles and applications. Berlin ; New York : Springer-Verlag, 1994.

20. E.M. Sobol, Phase transformations and ablation in laser-treated solids. New York : Wiley, 1995.

21. W.L. Kruer, The physics of laser plasma interactions. Redwood City, Calif. : Addison-Wesley, 1987.

22. L.J. Radziemski , D.A. Cremers (Editors), Laser-induced plasmas and applications. New York : M. Dekker, 1989.

23. D.A. Cremers, L.J. Radziemski, Handbook of laser-induced breakdown spectroscopy. Chichester, England ; Hoboken, NJ : John Wiley, 2006.

24. A.W. Miziolek, V. Palleschi, , I. Schechter (Editors), Laser-induced breakdown spectroscopy (LIBS) : fundamentals and applications. Cambridge : Cambridge University Press, 2006.

25. Y.B. Zel'dovich , Y.P. Raizer, Elements of gas dynamics and the classical theory of shock waves. (Translated by Scripta Technica, inc.), New York: Academic Press, 1968.

26. S.A. Ramsden , P. Savic, Radiative Detonation Model for Development of Laser-Induced Spark in Air. *Nature*, vol. 203, no. 4951, p. 1217, 1964.

27. Y.P. Raizer, Breakdown and Heating of Gases Under Influence of a Laser Beam. *Soviet Physics USPEKHI-USSR*, vol. 8, no. 5, p. 650, 1966.

28. A.J. Alcock *et al.*, Expansion Mechanism in a Laser-Produced Spark. *Physical Review*, vol. 20, no. 20, p. 1095, 1968.

29. A. Bogaerts *et al.*, A Laser ablation for analytical sampling: what can we learn from modeling? *Spectrochimica Atca Part B*, vol. 58, no. 11, p. 1867, 2003.

30. L.J. Radziemski, D.A. Cremers, T.R. Loree, Detection of beryllium by laser-induced breakdown spectroscopy. *Spectrochimica Acta Part B*, vol. 38, p. 349, 1983.

31. J.E. Carranza , D.W. Hahn, Assessment of the Upper Particle Size Limit for Quantitative Analysis of Aerosols Using Laser-Induced Breakdown Spectroscopy. *Analytical Chemistry*, vol. 74, p. 5450, 2002.

32. V. Hohreiter, D.W. Hahn, Plasma-Particle Interactions in a Laser-Induced Plasma. *Analytical Chemistry*, vol. 75, no. 5, p. 1509, 2006.

33. R.E. Russo *et al.*, The Physics of Laser Ablation in Microchemical Analysis. *Analytical Chemistry,* vol. 74, no. 3, p. 70A, 2002.

34. T.A. Schoolcraft *et al.*, Molecular Dynamics Simulation of the Laser Disintegration of Aerosol Particles. *Analytical Chemistry*, vol. 72, p. 5143, 2000.

35. M. Capitelli, F. Capitelli , A. Eletskii, Non-Equilibrium and Equilibrium Problems in Laser-Induced Plasmas. *Spectrochimica Acta Part B,* vol. 55, p. 559, 2000.

36. J.A. Aguilera, C. Aragon, Characterization of a Laser-Induced Plasma by Spatially Resolved Spectroscopy of Neutral Atom and Ion Emissions: Comparison of Local and Spatially Integrated Measurements. *Spectrochimica Acta Part B*, vol. 59, p. 1861, 2004.

37. O. Barthelemy *et al.*, Investigation of the State of Local Thermodynamic Equilibrium of a Laser-Produced Aluminum Plasma. *Applied Spectroscopy*, vol. 59, no. 4, p. 529, 2005.

38. J.D. Winefordner *et al.*, Comparing Several Atomic Spectrometric Methods to the Super Stars: Special Emphasis on Laser Induced Breakdown Spectrometry, LIBS, a Future Super Star. *Journal of Analytic Atomic Spectrometry*, vol.19, p. 1061, 2004.

39. D.A. Cremers, L.J. Radziemski, T.R. Loree, Spectrochemical analysis of liquids using the laser spark. *Applied Spectroscopy*, vol. 38, p. 721, 2004.

40. J. Scaffidi, S.M. Angel, D.A. Cremers, Emission Enhancement Mechanisms in Dual-Pulse LIBS. *Analytical Chemistry*, vol. 78, no. 1, p. 25, 2006.

41. S. Preuss, E. Matthias, M Stuke, Sub-Picosecond UV Laser Ablation of Ni-Films: Strong Fluence Reduction and Thickness Independent Removal. *Applied Physics A*, vol. 59, no. 1, p. 79, 1994.

42. S.M. Angel *et al.,* LIBS Using Dual- and Ultra-Short Laser Pulses. *Fresenius Journal of Analytical Chemistry*, vol. 369, nos. 3-4, p. 320, 2001.

# 3. DETECTION AND CLASSIFICATION OF BIOLOGICAL AEROSOLS

## 3.1 Introduction

Biological warfare agents pose a serious threat to both military establishments and civilian population centers. A potential method for disseminating biological agents is via aerosols with particles in the respirable size range of 1-10 μm [1]. Therefore, the accurate detection of airborne pathogens amidst the ambient background of dirt, biological debris, and combustion products is of considerable importance. In addition to defense applications, fast and accurate detection and classification of biological aerosols could be important in preventing the spread of disease in hospitals and for monitoring outdoor allergy-causing molds and pollens.

In most concepts for complete biowarfare-agent detection systems, a fast, consumables-free sensor continuously samples air and functions as a "trigger" for subsequent, usually wet-chemistry based, identification of threatening aerosol particles [1]. Considerable progress has been made in applying various combinations of particle sizing, particle counting, and fluorescence measurements to the trigger component of bioaerosol detection [2-7]. Fluorescence based aerosol triggers provide reasonable rejection of inorganic background clutter, but fluorescent combustion products and natural biological aerosols may cause interference [1]. High false-trigger rates due to background aerosols can drive up system operating costs by increasing the use of

consumables such as chemical reagents in the identifier. Technologies that offer discrimination against fluorescent, non-threat aerosols would substantially reduce the deployment costs of bioagent aerosol detection systems and subsequently increase their utility. Additionally, consumables-free technologies with the ability to classify biological aerosols into broad categories such as fungal spores, pollens, bacteria, viruses, and toxins would further reduce operating costs, add another level of confirmation to the identifier, and allow the optical trigger/classifier to operate independent of a full detection system in certain, limited-role applications.

Most likely, optimal false-trigger rates and classification capabilities will require the fusion of two or more orthogonal measurement technologies. The addition of elemental analysis to fluorescence/sizing measurement is one example of such a concept. Biological organisms contain a wide variety of readily detectable inorganic elements such as Ca, Mg, Mn, Fe, P, Na, K, and Si [8]. In some cases, the relative amounts of these elements vary between different classes of organisms. For example, it is well known that during sporulation bacterial spores concentrate calcium dipicolinate [9]. Accordingly, Table 3.1 shows a laboratory analysis of seven elements in three types of sporulated *Bacillus subtilis var. niger* (Bg), a common simulant for *Bacillus anthracis*, and three types of fungal spores. Although the total weight percent of the inorganic species varies within the Bg samples, the relative ratios remain fairly similar. More interesting are the significant differences in the ratios of Ca, K, P, and Na between Bg and the fungal spores. This suggests that elemental analysis offers substantial potential for broad classification of biological aerosols.

Several techniques exist in atomic spectroscopy for the analysis of laboratory samples. However, many of these techniques are not easily translatable into field instruments. Laser-induced breakdown spectroscopy (LIBS) is one of the most practical means for bringing elemental analysis to the field [10]. The technique involves tightly focusing a laser pulse to create a microplasma via laser breakdown of a sample or ambient air. Material inside the plasma volume is ionized and decomposed into atomic constituents. The hot plasma (10,000-15,000 K) provides a thermal excitation source for the atomized species within the plasma volume. Emission from these electronically excited atoms and ions is spectrally resolved and used to determine the elemental composition of the sample. The lack of sample preparation, experimental simplicity, and portability of modern lasers makes LIBS an attractive and practical technique for deployment in field sensors.

A rough gauge of the ability of LIBS to detect single bioaerosol particles can be made by considering the absolute mass of each element (Table 3.1) present in a representative bioaerosol particle, relative to the LIBS detection limits reported in the literature. A single bacterial spore represents a generally lower size limit for a typical bioaerosol particle. It can be approximated as a cylindrical particle with 2.5-μm length, 1-μm diameter, and a density of ~1 g/cm$^3$. This representative particle would have a mass of approximately 2 pg. Recently, Hahn and co-workers used a portable LIBS instrument to measure Na, Ca, Mg, and Al from ambient aerosols. They reported absolute mass detection limits of 0.5, 1.2, and 3.3 fg for Ca, Mg, and Na [11]. These detection limits for Ca and Mg are similar to previously reported limits determined using a differential mobility analyzer to measure a monodisperse aerosol stream [12]. Based on these limits,

one would expect to be able to detect these elements in a bioaerosol particle at concentrations of 0.1% by weight. Given the concentrations of these elements in Bg (Table 3.1), it is expected that LIBS should be able to detect them in single spores. In reality, a bioaerosol will have a distribution of particle sizes so that a significant fraction of the bioaerosol particles would actually be larger.

A large body of work on the LIBS technique exists; a general introduction to the technique and a survey of the literature can be found in a number of reviews [13-16]. Particularly relevant to this study is the literature associated with detection of aerosol particles, which reveals limitations to the LIBS technique. Because the plasma is responsible for both particle ablation/vaporization and excitation of elements in the sample, plasma stability is critical for reproducibility and a favorable signal-to-noise ratio (S/N) in LIBS. Air plasmas exhibit a saturation effect with increasing laser power; it is observed that an increasing percentage of the incident laser energy is absorbed by the plasma until a saturation of approximately 60% of the incident laser power is reached. Operation in this saturated regime has been shown to increase the reproducibility of the LIBS signal [17].

The potential of incomplete vaporization of particles also produces uncertainty in LIBS analysis. It is commonly accepted that the energy in a typical breakdown is sufficient to vaporize micron-sized particles and atomize molecules in the plasma volume. Estimates of the largest particles that can be vaporized, with ensuing LIBS detection of the particles, have ranged from ~2.5 μm to ~10 μm, and are expected to depend on the particle composition and on experimental conditions such as laser power. Such analysis has not been completed for the chemical matrices relevant to bioaerosol detection. In

addition, an optimal detection window for peak S/N exists for each element based on the transition energy and the transition probability [18,19].

Once optimal S/N is achieved, a robust method is required to distinguish particles from noise generated by the plasma and detection system. Schechter et al. suggest that spectral sorting based on various characteristics could be used to discriminate aerosol particles suspended in gas and reject ill-conditioned spectra, which may have variations due to matrix effects, poor atomization of the particle in the plasma, or laser power fluctuations [20,21]. Following this concept, Hahn presented an analysis of LIBS-based aerosol detection, elemental analysis, and particle sizing [12], which was subsequently confirmed for laboratory-generated aerosol particles and polydisperse particles of known composition using a differential mobility analyzer to size-segregate the particles prior to LIBS [22]. These strategies have enabled LIBS to be used successfully for measurements of particulate-bound metals in effluents from thermal treatment processes [23,24]. Additional aspects of LIBS for aerosol detection are covered in a recent review by Martin et al. [10]

Here, we report on the investigation of LIBS as a biotrigger technology. Two different LIBS instruments were used to explore aspects of the technique fundamental to its utility for bioaerosol detection: (1) its discrimination potential for bioaerosol sensing, and (2) the detection of the discriminatory elements in single-bioagent-simulant particles. To address discrimination potential, a broadband LIBS instrument was used to acquire spectra of dense aerosols over the range 200-825 nm. These spectra were subjected to principal components analysis (PCA) to gauge the overall discrimination ability of the technique. Since the broadband system was not capable of detecting single particles,

single-particle detection of Bg was demonstrated over narrow spectral windows with a more sensitive spectrometer/intensified-CCD system.

## 3.2 Experimental

### *3.2.1 Broadband, Multi-particle LIBS of Aerosols*

Broadband, multi-particle LIBS spectra were recorded using the apparatus in Figure 3.1. A Big Sky Ultra CFR-GRM Nd:YAG laser was used to generate the plasma. Typical of lasers used for LIBS experiments, it produces 7-ns, 50-mJ pulses at 1064 nm with a maximum repetition rate of 20 Hz. The laser pulses were focused with a 2-in.-diameter, 75-mm-focal-length UV-grade fused-silica lens (L1). CCD images of the resulting plasma (in air) indicate a plasma volume on the order of $10^{-4}$ $cm^3$ (1-mm-long, 0.5-mm-radial-diameter ellipsoid). Optical emission from the plasma was collected with L1 and focused into a bifurcated fiber bundle (BF, NA = 0.22, diameter = 600 μm for each fiber) using a 2-in.-diameter, 100-mm-focal-length UV fused-silica lens (L2). Each fiber was connected to the input port of an Ocean Optics HR2000 spectrometer, each with a 5-μm slit width. The spectrometers were equipped with electronic triggering, so that signal integration could be delayed in increments of 500 ns from the time the laser fired (total integration time is fixed at 2 ms). For the experiments presented here, this delay was set to 3.5 μs to prevent unwanted ion lines and broadband plasma emission from decreasing S/N. The UV/VIS spectrometer (S2) covered 200-650 nm with 0.35-nm nominal resolution, and the NIR spectrometer (S1) covered 613-825 nm with 0.15-nm nominal resolution. Since an aerosol LIBS sensor will likely encounter a variety of particle sizes, it was assumed that any discrimination algorithm would rely on the ratios of line intensities as opposed to absolute intensities. Therefore, the acquired LIBS spectra

were not corrected for chromatic focusing aberrations, wavelength-dependent CCD response, or wavelength-dependent grating efficiency since these effects should not vary from sample to sample.

An issue in obtaining background-free LIBS spectra of powders is finding a suitable means to bring the sample into the plasma volume for measurement. One approach is to adhere the sample to a surface such as double-sided adhesive tape or a silicon wafer. However, any substrate can contribute atomic lines to the LIBS spectrum that may hide features due to the sample alone. Additionally, because complex materials such as tape include many of the same elements present in the bioagent simulants, they might produce erroneous discriminating features that could vary from sample to sample, or shot to shot, depending on the relative amounts of substrate and sample consumed in each measurement. Therefore, as shown in Figure 3.1, a small pile of sample was placed in a microcentrifuge tube for measurement. The tube was positioned so that the air plasma formed at its mouth. The shock wave resulting from each laser shot aerosolized sufficient material that the subsequent laser pulse encountered a dense sample cloud. By continually running the laser at 5 Hz, single-shot spectra were obtained from a continually refreshed, dense aerosol cloud. No signal was observed from empty tubes, indicating that the plasma was not ablating the tube walls. In this way, clean, substrate-free spectra were obtained for each sample. Table 3.2 contains a list of the samples investigated. Bioagent simulants included three types of Bg and three “protein/media” that simulate viruses, toxins, or growth media. The various types of Bg differ from each other in growth history and washing methods. Background materials included three types of fungal spores, three types of pollen, and dirt.

*3.2.2 Narrowband LIBS of Single Aerosol Particles*

Single Bg particles were measured using the more sensitive intensified-CCD system, in which a frequency-doubled Big Sky CFR-400 Nd:YAG laser with a nominal pulse energy of 200 mJ/pulse fires at an adjustable rate between 1 and 10 Hz to generate an air plasma inside a sample cell. We note that previous work has shown the similarity of the 1064 nm and 532 nm Nd:YAG wavelength-generated plasmas for elemental analysis [25]. A 3:1 Galilean telescope expands the 0.6-cm beam from the laser to 1.8-cm diameter, and the expanded beam is focused using a 10-cm-focal-length plano-convex lens. Emission from the plasma is detected at right angles using a 7.5-cm, 2-inch diameter, plano-convex lens to collimate the light. A 5.2-cm-focal-length, 3-cm-diameter reflective collection system (Multichannel Instruments CC-52) efficiently couples the plasma light into a UV-compatible, 0.22 NA optical fiber bundle. The optical collection system is characterized by an overall N.A. of ~ 0.11, which corresponds to a 0.44 sr solid angle of collection. The fiber transmits the light to a Roper Scientific PI-Max gated, intensified CCD camera (UV enhanced) mated to a 0.3-m Acton SpectraPro 300i spectrometer. This setup, collectively referred to here as the Roper system, allows extremely accurate time gating of the collected emission signal, on the order of 5 ns. The effective dispersion of the system using a grating with 1200 grooves per millimeter is approximately 0.05 nm per pixel, allowing spectral window segments of ~50 nm to be recorded with each shot.

An aerosol stream was generated from a dry powder. Aerosol particles were suspended in an air stream (5-20 lpm of HEPA-filtered air) using a 60-Hz excitation current driving a loudspeaker. Software processing of each acquired spectrum detects individual aerosol hits by monitoring wavelengths corresponding to atomic emission lines.

The operation of the aerosol generator was varied to result in a measured aerosol hit rate in the sample cell between a maximum of one hit per 10 shots and a minimum of approximately one hit per 50 shots. As a result, to first order the frequency of double particle hits is between 0.01 and 0.0025.

## 3.3 Results and Discussion

### *3.3.1 Broadband, Multi-particle Measurements*

Figure 3.2 displays averaged LIBS spectra for the various classes of biological simulants and representative background materials. The illustrated spectra are normalized by their total spectral power (integration of the entire spectrum), and in the following discussion ratios of individual elements are determined by integration of the relevant atomic peaks. Figure 3.2 also shows the LIBS spectrum of a dirt sample in order to give some idea of inorganic aerosols likely to be encountered in the real environment. A few conclusions can be drawn from visual inspection of the individual LIBS spectra. Most important, each class of biological sample has a distinctive feature: Ca:K ratio >> 1 in Bg, Ca:K ratio << 1 for fungal spores (e.g., Penicillium), an overwhelming Na signal in the ovalbumin spectrum, and a minimal sodium signal (combined with Ca:K > 1) in pollen. In most of the biological samples a relatively broad peak is seen around 387 nm, attributed to recombination of CN in the cooling plasma. The peak is also evident in diesel and spark-ignited engine exhaust, where it has recently been used in conjunction with atomic O and N measurements to quantify engine equivalence ratio [26]. Potentially, this molecular peak could be used to separate predominantly carbon-based particles (mostly biological) from inorganic particles. Phosphorus, with a peak near 255 nm, is not readily visible in the bulk LIBS spectra. This is likely due to the combined effect of

delaying detection by 3.5 μs (phosphorus emission should peak early because of its large excitation energy) and the low (<30%) efficiency of the Ocean Optics grating and CCD detector at this wavelength.

Even when operating significantly above the detection limits, as is the case with bulk samples, shot-to-shot reproducibility of LIBS spectra can be poor because of variations in the plasma volume, temperature, and electron density. Variations of these plasma characteristics affect both absolute and relative intensities of spectral lines. Therefore, it is important to understand the magnitude of these fluctuations relative to differences between samples. Additionally, in order to be of utility for discriminating classes of organisms from one another, the variation in LIBS signatures between *samples in the same class* must be significantly less than the differences between *samples from different classes* (i.e., LIBS signatures of two samples of Bg must be more similar to one another than to corn smut). This issue is addressed in Figure 3.3, which summarizes the statistics of the major atomic lines in the LIBS spectra of all 12 biological samples. The height of each bar represents the average value of all the single-shot, sum-normalized spectra of a given sample type, and the error bars are drawn at +/-1 σ. When the LIBS results in Figure 3.3 are compared with the analysis of Bg (different samples of Bg) and fungal spores in Table 3.1, there is very good semiquantitative agreement across all four elements. Among these four elements, the discriminating features of each sample class are above the noise level set by the shot-to-shot variations. In single-particle measurements, other noise sources such as shot noise and variable particle ablation become important since many of the elemental concentrations are near LIBS detection limits. Nonetheless, these initial results are encouraging in that the reproducibility of the

LIBS technique is sufficient for discriminating among this limited set of bioagent simulants and interferants. It is interesting to note that, even using only Mg, K, Ca, and Na lines, differences between types of Bg, growth media, and fungal spores are significant, indicating that LIBS measurement of a few elements may be able to go beyond broad classification and differentiate more specifically, e.g., between different types of fungal spores or bacterial spores grown under different conditions.

To visualize and assess the discrimination potential of LIBS (multi-particle, broadband), PCA was applied to the 30 most prominent lines in the data set. This analysis provides a lower-dimensional representation of a data set in a coordinate system that preserves the maximum amount of the data set's variance (roughly its information content) [27]. For discrimination between biological sample classes, a reduced "training set" was constructed by determining average spectra for each sample class (one for Bg, one for fungal spores, etc.). These four spectra were then used with a basic PCA procedure to generate a three-dimensional coordinate system that best represented the differences between each sample class. Each coordinate is composed of a linear combination of atomic line intensities weighted by their contribution to the training set's variance (they are the eigenvectors of the data's covariance matrix). The atomic line intensities from each individual, normalized spectrum were then used to put each single-shot LIBS spectrum into the PCA space as a single point. Figure 3.4 illustrates this three-dimensional representation of the data, in which all four biological sample classes are fairly well separated. The pollen data set shows significant spread, much of which is due to the lower S/N of the pollen spectra. The lower S/N of the pollen is probably due to the larger particle size of pollen (20-60 μm), which makes it difficult to aerosolize and to

fully ablate. The spread in each sample cluster is the combined effect of shot-to-shot reproducibility and the true variation between the different samples in each class (e.g., oat smut vs. penicillium), which can both be seen in the error bars of Figure 3.2.

As suggested by Figure 3.3, there are indications that LIBS spectra can be used to differentiate samples within the same class. This type of capability could be useful in determining the source or identity of a particular bioaerosol. A PCA analysis on each sample class, using training spectra constructed from averages of each sample type, such as the various Bg samples, was used to explore this type of high level discrimination. The results are shown in Figure 3.5. It appears that the LIBS spectra do provide significant discrimination between the different types of fungal spores, growth media, and Bg samples. Since these spectra are not single particles, it is not clear whether the different Bg spores are actually different or if their spectral signatures come from impurities such as residual growth media. Spectrally broadband, single-particle measurements will be required to determine the origin of these differences in LIBS signatures.

Some cautionary statements should be made about the discriminatory power of LIBS. First, nearly all the "signature" elements of the biological samples can be found in dirt. An example of this is the dirt in Figure 3.2, which contains Mg, Ca, K, and Na, albeit in different ratios than either Bg or fungal spores. It is not hard to imagine, given the diversity of the natural environment, that other types of inorganic materials would have mineral signatures very similar to the biological materials. The CN peak does offer some discrimination, but varies significantly among the samples of biological origin. Therefore, although LIBS potentially offers better discrimination between biological materials, it might not perform as well as current methods, such as fluorescence, in

separating dirt particles from biological aerosol particles. Further, we should emphasize that the use of PCA in this work is merely illustrative of the potential for LIBS-based discrimination, but that more robust algorithms would likely be required in real-world applications.

The presence of these signature elements in the inorganic material also has significant consequences for LIBS of mixtures. Since the signatures of the simulants rely on the relative intensities of multiple lines, rather than the presence of a single unique line, it is not hard to imagine that LIBS analysis of mixtures could easily cause inaccurate classification. An example, taken from this data set, would be a mixture of ovalbumin (mostly Na and CN) and dirt (mainly Ca and K). In the correct proportions, this would have a nearly identical signature to the LIBS spectrum of Bg. Although this study does not push the limits of chemometrics, the exploitation of matrix effects, or pattern recognition, LIBS of single particles will most likely be very useful for detecting bioagents and discriminating them from the natural background.

### *3.3.2 Single-Particle, Narrowband Measurements*

In order to address the question of whether or not LIBS is capable of detecting the amounts of Ca, Na, Mg, etc. present in single biological particles, narrowband single-shot spectra of individual Bg particles in dilute flows were measured using the Roper system. Although the detection limits mentioned earlier [12] indicate that the relevant concentrations should be readily detectable, the bioaerosol particles are complex matrices and it is important to verify that matrix effects do not elevate the detection limits above the expected absolute masses. To obtain these measurements, the aerosol generator was operated in a regime in which the maximum particle hit rate is roughly 1:10. Thus, as

noted above, the expectation is that the incidence of simultaneous two-particle hits should be roughly 1:100, but there was no way to measure coincidence of particles directly in these experiments. Typical mean particle sizes for the Bg aerosols, determined by aerodynamic particle sizing, are roughly 2.5 μm.

Quantification of LIBS peaks can be accomplished using several methods, such as by integrating the peak area following baseline subtraction or by ratioing the peak area to the baseline area. The latter quantity is referred to as the peak/base ratio, and has the benefit of attenuating fluctuations attributed to variations in the laser power, as both the peak strength and the baseline strength are functions of the laser power. For measurements described in this paper, the peak area and the peak/base ratio are closely correlated. The peak/base ratio was used as the measurement variable (e.g., Figure 3.7), as it has been shown (e.g., Ref. 18) that relatively robust calibrations, applicable in the field where conditions may cause fluctuations in laser power and/or transmitted light, are possible using peak/base ratio. Dedicated software analyzed individual spectra to determine the peak/base ratio for each element, which then was converted to the measured mass of each element using laboratory calibrations.

A timing of a 5-μs delay after the laser pulse and a 60-μs gate width after the shutter opening allows relatively good detection of all of the measured species. Detection limits for Ca, Mg, and Na (obtained with standard aerosols of each element) are shown in Table 3.3. These are not optimized for each element, as were the detection limits mentioned earlier [12]. The detection limits shown in Table 3.3 are related to the minimum percent concentration of the element in the hypothetical single-spore particle described in the introduction. Based on the elemental analysis of Bg shown in Table 3.1,

these detection limits suggest that individual spores are close to the detection limit of our LIBS system as presently configured, but that agglomerated particles should be readily detectable. As agglomerates are expected in realistic situations, these results are equally relevant to the detection of real bioaerosol clouds. In addition, with the present system, detection limits for individual elements could be improved with optimized delay and gate for each element.

With the limited spectral range of the Roper system, it is not possible to measure all of the spectral lines at once, as one may do with an echelle spectrometer or a suitably configured linear array spectrometer. Hence, to visualize the entire spectrum that may result from a single-particle hit, a composite spectrum must be generated from a combination of spectra from each of the spectral windows. Figure 3.6 shows a composite single-shot, single-particle-based spectrum of Bg. Ca, Na, and Mg are visible in the spectra of single Bg particles. Although the ratios of atomic lines in separate spectral windows are meaningless because they are not obtained from the same particle, the composite spectrum can be used to gauge the relative S/N of each element present in the bioaerosol. The background noise, which is primarily from the intensifier and the plasma itself, is somewhat more evident in single-shot spectra than the average spectra, but the signals are still much stronger than the background.

For these experiments, sets of 1000 spectra were taken in each spectral window. Following the data acquisition, software triggers were set to discriminate elemental peaks (as relevant to the spectral window) using an adjustable criterion for peak detection based on the measured RMS noise ($\sigma$) in the spectral region immediately adjacent to the relevant peak. Peaks and noise are both integrated over the spectral line width. For many

elements, including all measured here, two lines are available in a single spectral region, allowing software detection on one line and verification/quantification on the other. For purposes of these experiments, a 3σ criterion is used; a spectrum is classified a "hit" if the measured variable at the peak is three or more times the RMS value of the measured variable in a region immediately adjacent to the peak. Following software detection of the atomic lines, all spectra classified as hits were hand checked to verify the hit, and no false hits were detected.

Figures 3.7 and 3.8 illustrate the detection of Ca in aerosolized Bg. Figure 3.7 shows the measured peak/base ratio for 1000 laser shots. The Bg concentration fluctuates somewhat during the experiment; the upper trace in Figure 3.7 illustrates the particle hit rate, averaged over 10 s, as a function of time. The average hit rate is approximately 1:10, but went as high as 1:5 for a short time near the end of the experiment. The 3σ hit criterion for Ca in the Bg spectrum, based on a spectral region immediately adjacent to the 422.7-nm peak of Ca, corresponds to a peak/base ratio of 12.5, which is shown in Figure 3.7 as a horizontal line near the bottom of the figure. Points above this line correspond to hits of Ca-containing Bg. Figure 3.8 illustrates the 91 measured Ca hits from Figure 3.7 in a histogram, and the cumulative percentage (by number) of hits as a function of peak/base ratio. In summary, based on the frequency of hits, the majority can be assigned to single-particle events with a high degree of confidence.

Measured elemental signal strengths for Bg are shown in Table 3.4, along with the standard deviation of each of the measured peaks (some of this variation is due to the distribution of particle sizes within the aerosol) and the RMS noise in that spectral region. The average S/N for typical Bg particles is also shown in Table 3.4. This experimental

data shows that detection of elemental concentrations relevant to single-particle detection of biological particles is possible. Based on the data from Table 3.4, each of the elements Ca, Mg, and Na has a S/N well in excess of 3, sufficient to discriminate individual particles, provided the spectral signatures of single particles match those obtained in the multi-particle measurements.

In addition to the technique's sensitivity in terms of optical signal strength, a central issue for any technology being considered for bioaerosol detection is its sensitivity in terms of minimum detectable particle concentration. In the case of a bioagent release, detection of agent concentrations as low as 10 particles/L within a time span of less than 10 min may be required to prevent infection [1]. In urban environments, the background aerosol concentration in the size range 1-10 μm can be up to 10,000 particles/L [28]. Therefore, any aerosol sensor must sort through a significant amount of air and benign particles to interrogate the offensive agent. This is particularly problematic for LIBS, which usually samples ~1 $mm^3$/laser shot at repetition rates <50 Hz. Without significant modification or new laser technology, a stand-alone LIBS sensor would not be capable of achieving the roughly 20-L/min sampling rate required for detecting realistic concentrations of bioagents. The addition of air concentrators and/or separate "cueing" detection technologies will most likely be required to increase the sensitivity of LIBS so that it can deal with scenarios of this type.

### 3.4 Conclusion

We have demonstrated that LIBS has significant potential as a bioaerosol classifier. The technique is able to resolve differing elemental ratios in biowarfare-agent simulants and in common biological and environmental interferants. Measurements

combined with PCA suggest that it may be possible to readily discriminate bioaerosols from interferences. Single-particle analysis of Bg spores reveals sufficient sensitivity to detect Ca, Na, and Mg, each with S/N > 3, illustrating that LIBS can be used to detect single bioaerosol particles.

When considering the detection of a minority aerosol species in the outdoor environment, laboratory measurements can only go so far. The capabilities of LIBS must be evaluated in the real outdoor environment. Future studies may consider using sensitive echelle spectrometers coupled with intensified CCD cameras or a polychromator/photomultiplier tube detector configuration to obtain both wide spectral range and the high sensitivity required to detect single particles.

**3.5 Acknowledgement**

Chapter 3, in full, is a reprint of material as it appears in Applied Spectroscopy, vol. 57, no. 10, p. 1207, 2003, Hybl, J., Lithgow, G.A., and Buckley, S.G.

**Table 3.1.** Elemental analysis of Bg and smut.

| Element[a] | Bg | | | Fungal spores (smuts) | | |
|---|---|---|---|---|---|---|
| | 1 | 2 | 3 | Oat | Wheat | Corn |
| Ca | 1.16 | 1.08 | 10.21 | 0.16 | 0.0147 | 0.12 |
| Mg | 0.30 | 0.37 | 2.80 | 0.20 | 0.0937 | 0.19 |
| Na | 0.45 | 0.38 | 5.82 | 0.0132 | 0.0110 | 0.0171 |
| K | 0.49 | 0.49 | 0.68 | 1.60 | 2.24 | 1.63 |
| Fe | 0.67 | 0.57 | 0.0088 | 0.0253 | 0.0032 | 0.0081 |
| P | 2.30 | 2.32 | 8.52 | 0.44 | 0.41 | 0.58 |
| Mn | 0.0081 | 0.0122 | 0.10 | 0.006 | 0.0024 | 0.0037 |

[a]Elemental concentrations as percent by weight.

**Table 3.2.** Samples tested.

| Sample class | Sample type |
|---|---|
| Bacterial spore | 3 types of Bg (A, B, C) |
| Media/protein | Ovalbumin (Ov)<br>Brain heart infusion (BH)<br>LB Broth (LB) |
| Fungal/mold spores | Penicillium (Pn)<br>Corn Smut (Cn)<br>Oat Smut (Ot) |
| Pollen | Ragweed (Rg)<br>Red Mulberry (Rm)<br>RedOak (Ro) |

**Table 3.3.** Detection limits with Roper system at 5-μs delay, 60-μs timing.

| Element | $\lambda$ (nm) | Mass detection limit (3σ) (fg) | Minimum percent concentration in representative Bg particle (wt%) |
|---|---|---|---|
| Ca | 422.67 | 30 | 1.5 |
| Na | 589.0 | 100 | 5 |
| Mg | 285.2 | 20 | 1 |

**Table 3.4.** Atomic line statistics for single-particle spectra of Bg.

| Line | Number of hits (3 × RMS) criterion | Peak/base ratio (hits) | Peak/base RMS noise | Deviation in peak/base | S/N |
|---|---|---|---|---|---|
| Mg 278 nm | 42 | 36.6 | 3.78 | 17.3 | 9.7 |
| Ca 422.67 nm | 76 | 72.8 | 4.43 | 68.8 | 16.4 |
| Na 589.0 nm | 91 | 137.8 | 15.69 | 98.3 | 8.8 |

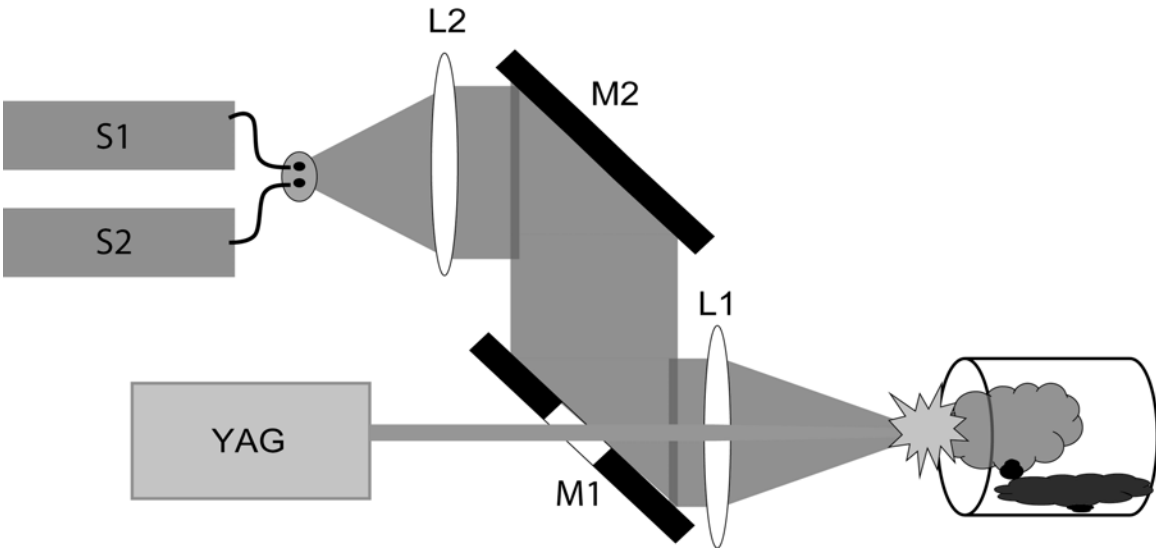


**Figure 3.1**. Experimental LIBS apparatus. A Big Sky Ultra CFR-GRM Nd:YAG laser (YAG) was used to produce the plasma. A 75-mm-focal-length lens (L1) was used to both focus the laser pulse and collect the plasma emission in the backward direction. A pierced aluminum mirror (M1) directed the plasma emission towards the collection optics. A 100-mm-focal-length lens (L2) was used to focus the emission into a bifurcated fiber bundle (BF) consisting of two 600-μm-core UV-rated fibers. The fibers then directed the emission into two Ocean Optics HR2000 spectrometers (S1:613-825 nm and S2: 200-650 nm).

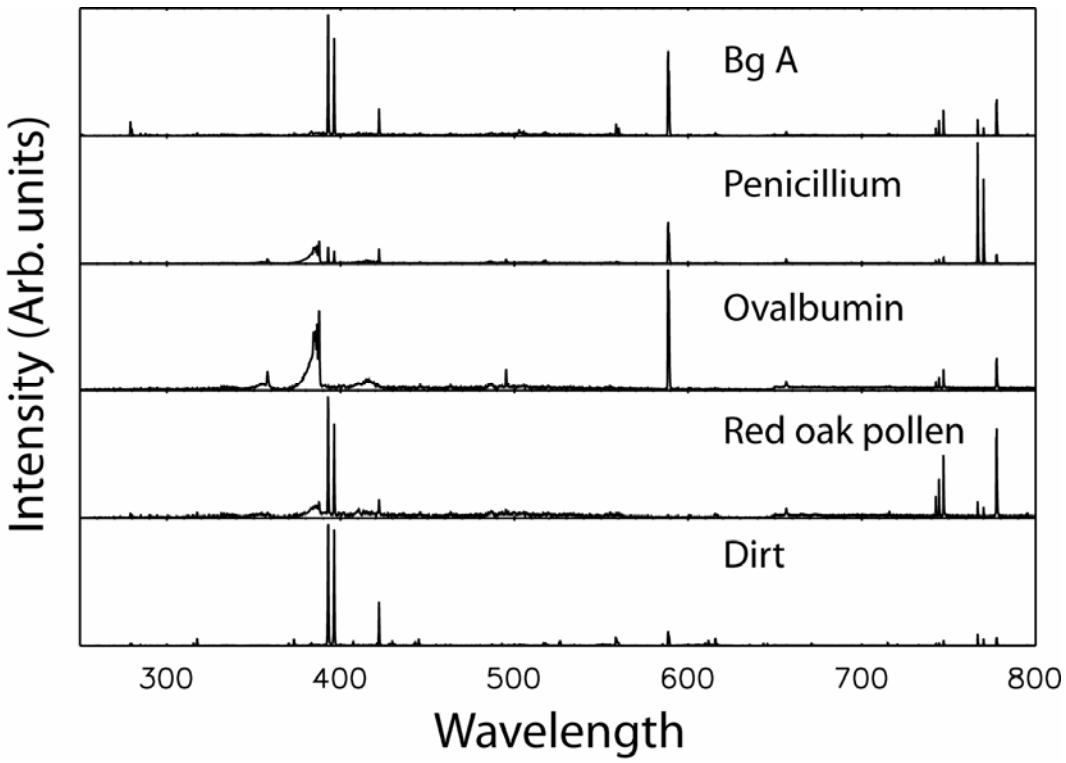


**Figure 3.2**. Representative LIBS spectra of bioagent simulants and background materials. Each spectrum is an average of 50-100 shots. The prominent atomic lines are: Mg (~285 nm), Ca (393, 396, and 422.7 nm), Na (~589 nm), and K (~766 nm); approximate wavelengths are given since some are unresolved or partially resolved multiplets. Molecular CN appears as a broad peak around 387 nm in some of the spectra. Atmospheric N is visible at roughly 741, 743, and 746 nm, and a prominent O line is apparent at 777 nm.

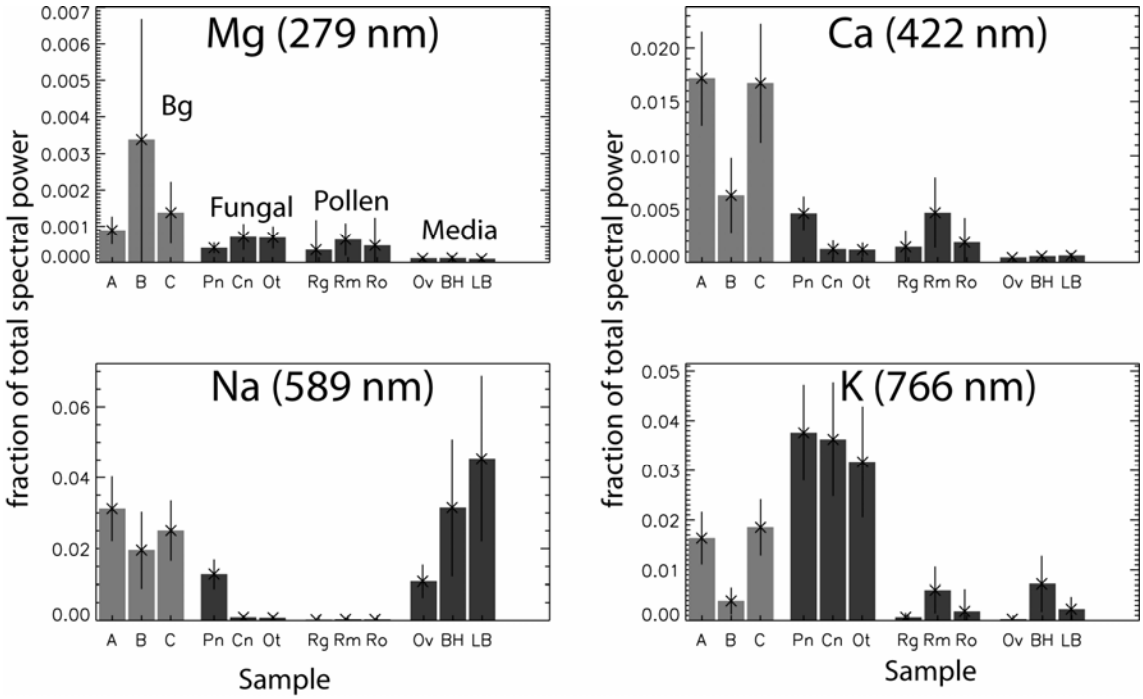


**Figure 3.3**. Bar plots representing major atomic lines in the LIBS spectra of the 12 biological samples. Each bar is drawn to the average value of the atomic line intensity for each type of sample (intensity is normalized by total spectral power). The error bars are drawn at +/-1 standard deviation and can be used as a guide to shot-to-shot reproducibility. Samples are annotated using the abbreviations in Table 3.2.

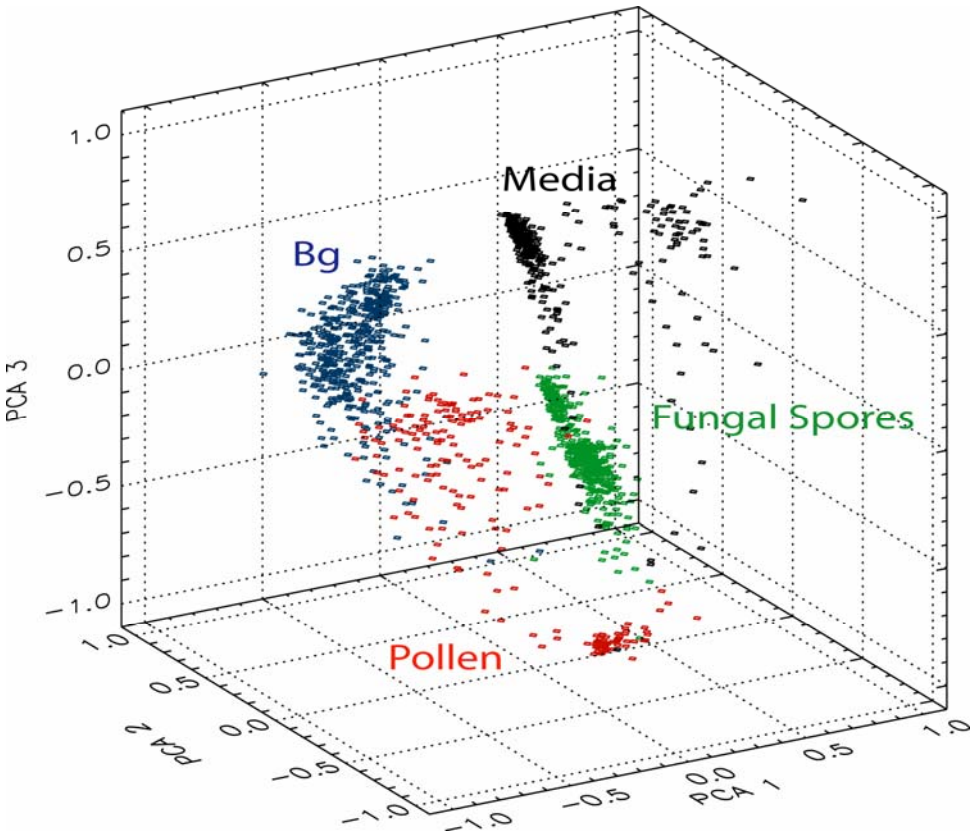


**Figure 3.4**. Three-dimensional scatter plot of the biological data set in the principal component coordinates. Each data point represents a single spectrum acquired from a single laser shot. The principal components were computed using three linear combinations of the intensities of 30 lines from the spectra. Each class of bioaerosol contains three different types, e.g., the fungal spore category is composed of penicillium, corn smut, and oat smut.

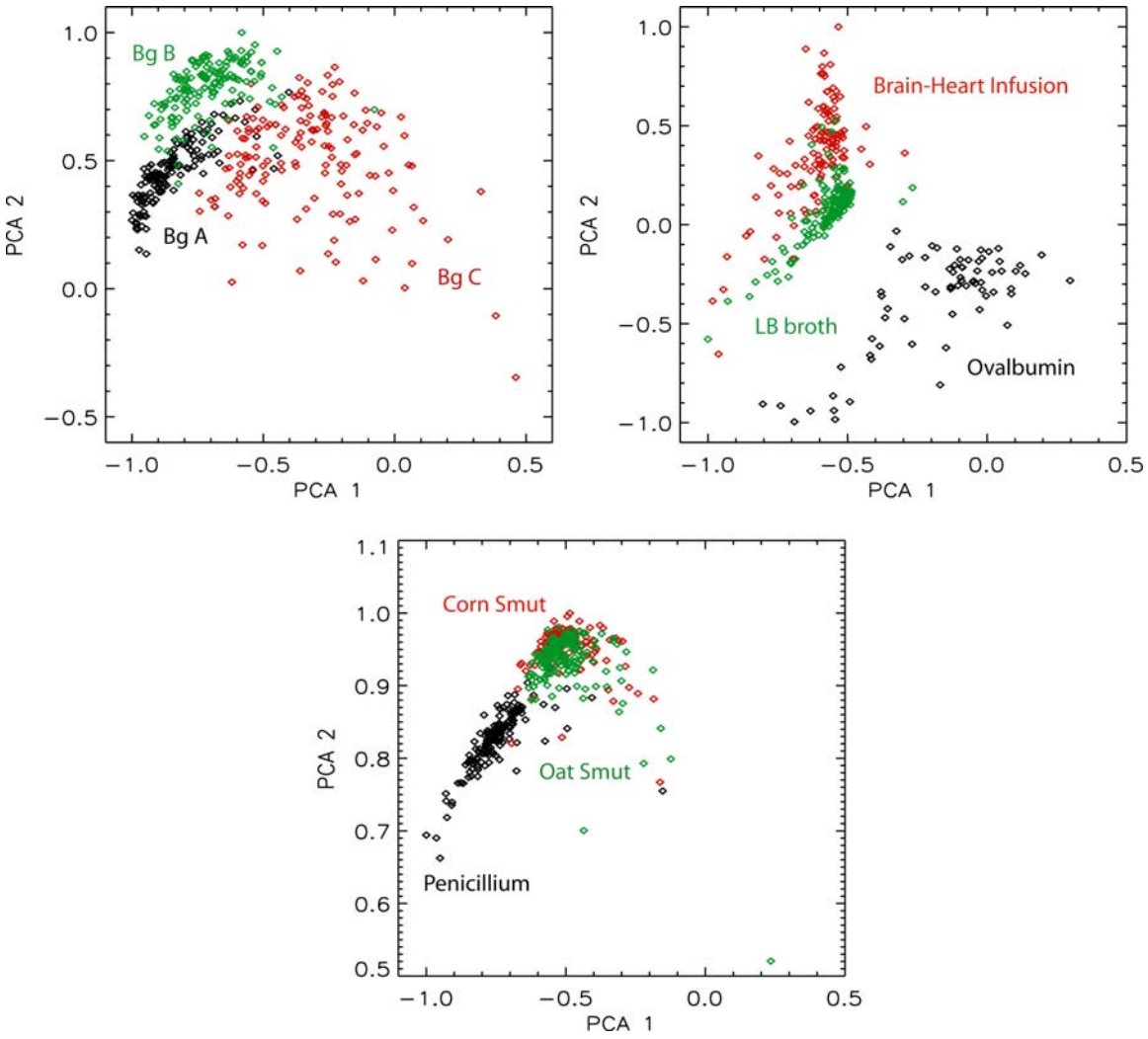


**Figure 3.5**. PCA plots of each bioaerosol class. In this case, the principal components were determined from training sets comprising average spectra of each specific type of bioaerosol. In all three cases, the first two principal components (PCA 1 and PCA 2) account for >95% of the training set's variance.

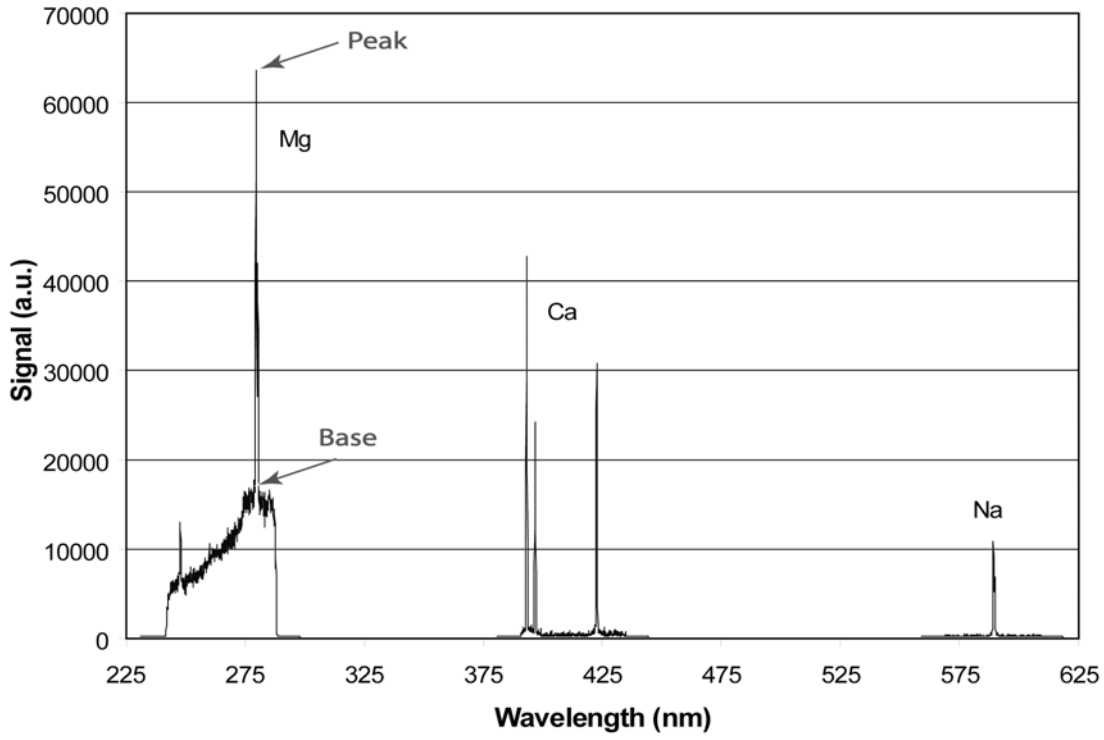


**Figure 3.6.** Representative composite single-shot spectra of Bg, with intensities unadjusted.

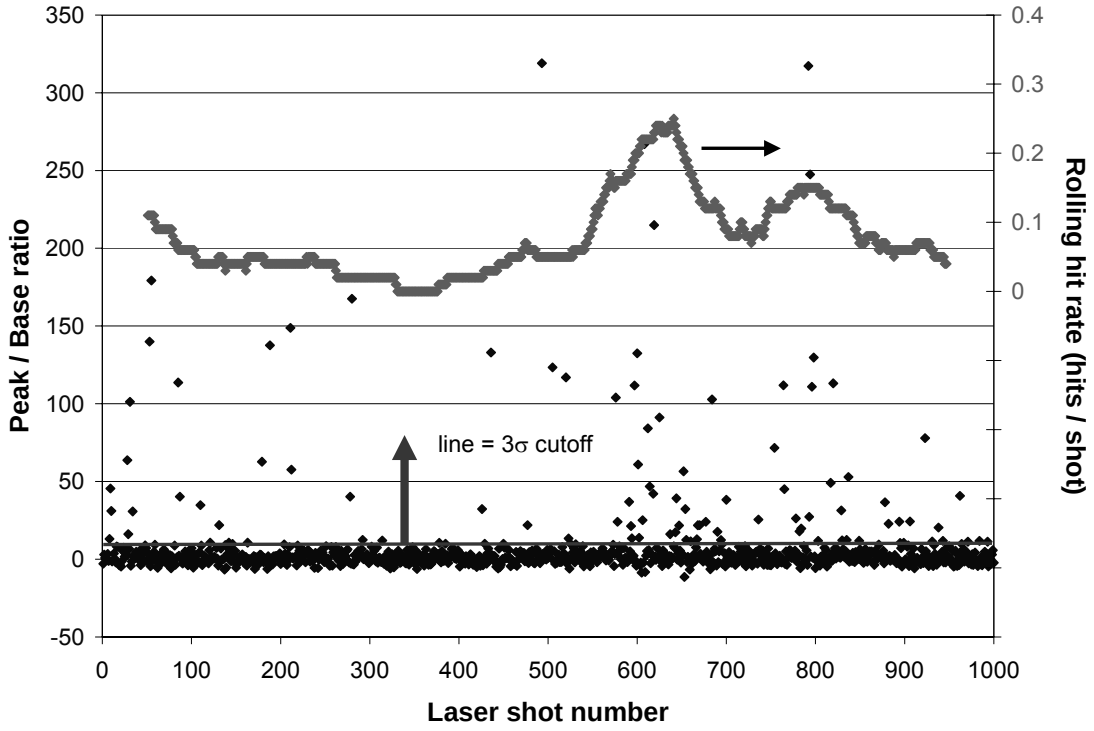


**Figure 3.7.** Peak/base ratio corresponding to Ca for 1000 shots with Bg flowing through the sample cell. The upper trace, associated with the right-hand axis, indicates the particle hit rate averaged over 10 s.

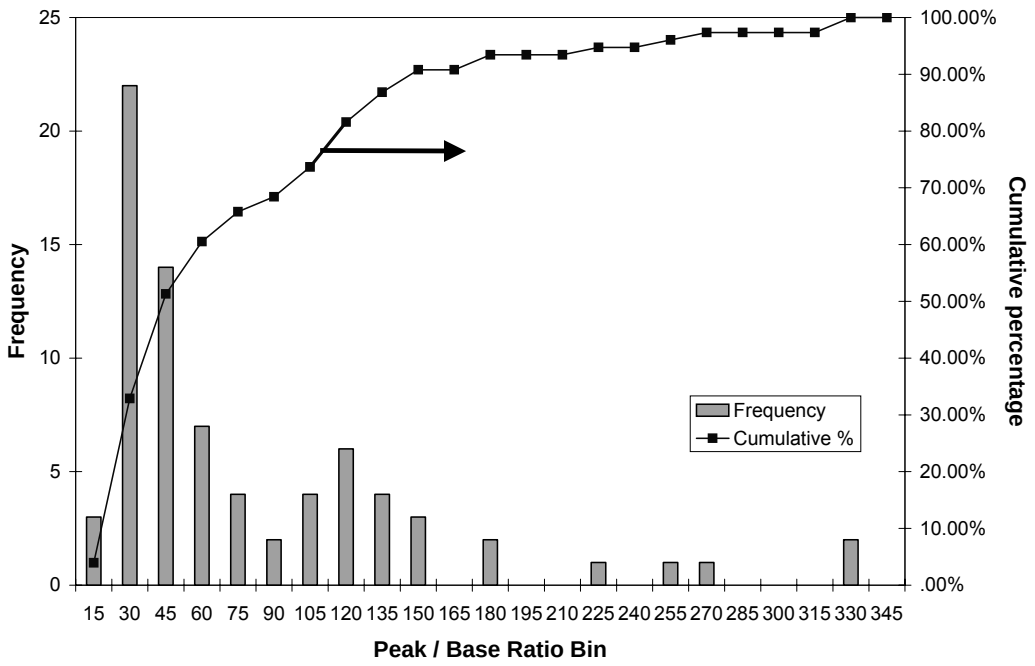


**Figure 3.8**. Histogram of Ca hits in aerosolized Bg, with peak/base ratio > 3σ, for 1000 shots. In these spectra 3σ ≈ 12.5.

**References**

1. C. A. Primmerman, *Linc. Lab. J.* vol. 12, p. 3, 2000.

2. P.P. Hairston, J. Ho, F.R. Quant, *J. Aerosol Sci*., vol. 28, p. 471, 1997.

3. J. Ho, M. Spence, P. Hairston, *Aerobiologia*, vol. 15, p. 281, 1999.

4. G.A. Luoma, P.P. Cherrier, L.A. Retflavi, *Field Anal. Chem. Technol*., vol. 3, p. 260, 1999.

5. P.H. Kaye, J.E. Barton, E. Hirst, J.M. Clark, *Appl. Opt*., vol. 39, p. 3738, 2000.

6. J.D. Eversole, W.K. Cary, C.S. Scotto, R. Pierson, M. Spence, A.K. Campillo, *Field Anal. Chem. Technol*., vol. 5, p. 205, 2001.

7. F.L. Reyes, T.H. Jeys, N.R. Newbury, C.A. Primmerman, G.S. Rowe, A. Sanchez, *Field Anal. Chem. Technol*., vol. 3, p. 240, 1999.

8. M. T. Madigan, J. M. Martinko, J. Parker, Brock Biology of Microorganisms, 8th ed. Upper Saddle River, NJ : Prentice Hall, 1997.

9. G. Gould, A. Hurst, The Bacterial Spore. London : Academic Press, 1969).

10. M.Z. Martin, M.D. Cheng, R.C. Martin, *Aerosol Sci. Technol*., vol. 31, p. 409, 1999.

11. J.E. Carranza, B.T. Fisher, G.D. Yoder, D.W. Hahn, *Spectrochim. Acta Part B*, vol. 56, p. 851, 2001.

12. D.W. Hahn, M.A. Lunden, *Aerosol Sci. Technol*., vol. 33, p. 30, 2000.

13. K. Song, Y.I. Lee, J. Sneddon, *Appl. Spectrosc. Rev*., vol. 32, p. 183, 1997.

14. K. Song, Y.I. Lee, J. Sneddon, *Appl. Spectrosc. Rev*., vol. 37, p. 89, 2002.

15. I. Schechter, *Rev. Anal. Chem*., vol. 16, p. 173, 1997.

16. L.J. Radziemski, *Microchem. J.*, vol. 50, p. 218, 1994.

17. J.E. Carranza, D.W. Hahn, *Spectrochim. Acta Part B*, vol. 57, p. 779, 2002.

18. B.T. Fisher, H.A. Johnsen, S.G. Buckley, D.W. Hahn, *Appl. Spectrosc*., vol. 55, p. 1312, 2001.

19. U. Panne, C. Haisch, M. Clara, R. Niessner, *Spectrochim. Acta Part B,* vol. 53, p. 1957, 1998.

20. I. Schechter, *J. Korean Soc. Anal. Sci.*, vol. 8, p. 779, 1995.

21. L. Xu, V. Bulatov, V. Gridin, I. Schechter, *Anal. Chem.*, vol. 69, p. 2103, 1997.

22. D.W. Hahn, *Appl. Phys. Lett.*, vol. 72, p. 2960, 1998.

23. S.G. Buckley, H.A. Johnsen, K.R. Hencken, D.W. Hahn, *Int. J. Integr. Waste Manage. Sci. Technol*., vol. 20, p. 455, 2000.

24. H. Zhang, F.-Y. Yueh, S. Singh, *Appl. Opt*., vol. 38, p. 1459, 1999.

25. S. Yalcin, D.R. Crosley, G.P. Smith, G.W. Faris, *Hazard. Waste Hazard. Mater*., vol. 13, p. 51, 1996.

26. F. Ferioli, P.V. Pusinauskas, S.G. Buckley, Laser-Induced Breakdown Spectroscopy for On-Line Engine Equivalence Ratio Measurements, *Appl. Spectrosc*., vol. 57, p. 1183, 2003.

27. D. L. Massart, B. G. Vandeginste, S. N. Deming, Y. Michotte, L. Kaufman, Chemometrics: A Textbook. Amsterdam : Elsevier, 1988.

28. R. Jaenicke, Aerosol-Cloud-Climate Interactions, P. V. Hobbs, Ed. San Diego :

Academic Press, 1993.

# 4. AMBIENT MEASUREMENTS OF METAL-CONTAINING PARTICULATE MATTER

## 4.1 Introduction

The composition of aerosol particulate matter (PM) in an urban environment is of interest from the standpoint of environmental impacts and potential human health effects. Aerosol particles in the U.S. are regulated on the basis of $PM_{10}$ and $PM_{2.5}$ mass, which are the fraction of particles smaller than 10 μm and 2.5 μm, respectively. These mass or volume-based regulations are convenient to measure, relative to number or composition, but likely do not capture all of the information that is relevant to health effects. Recent studies have suggested that the number, size, and composition of particulate matter may all have an important role in health effects attributed to PM [1]. In particular, although the mechanisms remain unclear, the presence of toxic metals, polycyclic aromatic hydrocarbons, and other known carcinogens in the respirable fraction of PM are suspected to contribute to measurable health effects [2,3], and the metal fraction may represent a substantial portion of the toxicity of aerosol particles [4].

For this reason, methods for measuring composition of aerosol particles are of interest. Static filter-based methods such as the U.S. Environmental Protection Agency (EPA) Method 29 are useful for bulk measurements of metals in PM, and similar analysis may be performed on impactor size-segregated aerosol particles to yield an understanding of the distribution of metals as a function of size [5] and the elemental and organic carbon

fractions [6]. However, the urban environment is far from a steady-state system. Shifting meteorological patterns coupled with temporally- and spatially-varying emissions result in exposure patterns that may change significantly over time scales of minutes. Understanding human PM exposure patterns thus requires a degree of temporal resolution not afforded by simple filter-based methods.

A number of near-real-time and real-time methods are under investigation for measurement of particle composition, applicable either to the effluent of thermal processes or to ambient measurements. Seltzer and co-workers have used a customized ICP system to monitor metal emissions from an incinerator [7]; this process has met the EPA relative accuracy requirements and is commercially available. However, the instrument is unable to measure individual particles. Similar investigations on another continuous metals emissions monitor based on an atmospheric microwave plasma are underway by Woskov and co-workers [8].

Ondov's group at the University of Maryland has developed a wet chemistry technique called SEAS (Semi-continuous Elements in Aerosol System), in which particles of all sizes entering the instrument are grown by condensation in supersaturated water vapor, and then separated using a virtual impactor [9]. The particle-laden stream is collected in impingers, and the metal content of the wash is analyzed using an ICP or other elemental analysis method. Time-resolved samples can be collected along with corresponding meteorological data to perform source apportionment [10]. However, there is a substantial time lag between data collection and analysis using this technique as currently configured.

Single-particle mass spectrometry, or aerosol time-of-flight mass spectrometry (ATOFMS) has been under development for some time as a real-time method for measurement of a range of atmospheric particles [11]. Aerosol particles are sampled into a low pressure inlet, aerodynamically focused, and their velocity is measured using a pair of lasers. A third laser is thus synchronized and fires to ablate the particle and create an ion signal. Both positive and negative ions can be measured, yielding both inorganic species and molecular fragment ion mass spectra, positive and negative. These instruments can measure both metals and atmospherically important fragments such as sulfates and nitrates on particles as small as a few hundred nm. Recent developments include both wide-range calibrations based on multivariate methods [12], and on extending the technique to particles in the tens of nm, eliminating the timing lasers and using a free-firing ablation laser [13]. The instrument developed by Prather's group is under commercial development by TSI, Inc. This method, however, is still largely qualitative.

Laser-induced breakdown spectroscopy (LIBS) has been used as an analytical technique for gases, liquids, and solids for some time, and has been extensively reviewed [14-17]. Applications of LIBS typically employ a pulsed laser with a high peak power to form a spark (breakdown) in the medium to be examined. The temperature of the resulting plasma at short times (< 10 μs) is in the range of 10,000 – 25,000 K [18], hot enough to dissociate molecules into their constituent atoms, and to excite the electrons in the neutral atoms and ions formed in the plasma out of the ground state and into excited electronic states. As the plasma cools, excited electrons and ions relax back into their ground states, emitting light at characteristic atomic frequencies. Identification of the

atoms present in the sample volume occurs using well-known atomic emission lines, and quantification of the elemental species concentration occurs via measurement of the intensity of the emission lines.

LIBS has been applied to the measurement of aerosol particles emitted from combustion process exhaust streams and ambient particles. Ottesen and co-workers [19] used LIBS to measure the composition of individual coal particles during and after combustion. Absolute elemental analysis of aerosol particles was suggested by Schecter's group in 1997 [20], and shortly afterward Hahn suggested that spectral sorting could be used to increase sensitivity over averaged measurements in dilute aerosol flows [21].

In combustion process exhaust streams, LIBS has primarily been used to measure inorganic species such as toxic metals, which typically occur in particulate form. Groups from Sandia National Laboratories [22,23] and Mississippi State University [24] have applied LIBS to quantification of emissions from incinerators and thermal processes. Recent work has been focused on increasing the sensitivity and accuracy of LIBS via optimization of the detection timing [25] and statistical treatment of the detected signals [26]. Hahn and co-workers have also recently measured ambient particles from 4$^{th}$ of July fireworks in the relatively rural environment around Gainesville, Florida, detecting Al, Ca, Mg, and Na [27]. LIBS systems that have been deployed in the field have been relatively compact and simple compared with other instruments; LIBS systems have been deployed, for example, 90 feet above the ground on 90 cm wide scaffolding for incinerator measurements [22].

**4.2 Experimental methods**

*4.2.1 LIBS Setup*

A schematic of the LIBS system is shown in Figure 4.1. The excitation source for the plasma was a Q-switched Nd:YAG laser operating at the fundamental wavelength (1064 nm). The laser repetition rate was 20 Hz, with pulse energy of nominally 40 mJ and nominal pulse width of 6 ns. The beam was expanded from its initial diameter of 6 mm to a diameter of nearly 25 mm, then focused with a 100 mm focal length, 50 mm diameter lens. The laser pulse energy is only slightly above the breakdown threshold of approximately 25 mJ measured under these conditions in ambient air.

This low laser pulse energy was chosen because previous, unpublished experiments by the authors suggested that single particle detection limits were optimized at low energy for highly dispersed particles. This could possibly be due to the dependence of plasma size on excitation energy, particularly if the plasma were optically thick under some conditions. The background light from the plasma scales with laser pulse energy, while emission from an individual particle in a plasma at local thermodynamic equilibrium is relatively fixed. Signal from a small particle could potentially be overwhelmed by emissions from a large, bright plasma, particularly if the particle is located such that an optically thick plasma screens the particle emission from the collection optics. However, a subsequent study by Hahn's group [26] demonstrated a drawback of lower pulse energies; the amount of energy absorbed by the plasma fluctuates greatly from shot to shot of the laser, resulting in reduced precision of the LIBS signal.

Emissions from the plasma were collected at a right angle to the incident laser beam. Plasma emissions were first collimated with a 75 mm focal length, 50 mm

diameter fused silica lens, then coupled to a fiber optic bundle with a Multichannel Instruments CC52 collector. The light was dispersed with a 0.3 m spectrometer with a 1200 groove/mm grating. Light was detected with a time gated, intensified charge-coupled device (ICCD) detector array. The effective linear dispersion was approximately 0.07 nm per pixel. Spectra were collected in four separate spectral windows, centered at 270, 340, 413, and 590 nm. The signal was integrated over different time gates for each window. The delay with respect to the laser pulse, and the gate width, were optimized for the elements of interest in each spectral region. In the 270 nm window, the delay was 1 μs and gate width was 5 μs (1/5). For the other windows, the times were 15/20, 15/40 and 20/40 respectively.

*4.2.2 LIBS Calibration*

Elemental concentrations are determined from LIBS spectra by measuring the peak-to-base (P/B) ratio and comparing it to a calibration. The P/B ratio is defined as the integral of the atomic emission peak normalized by the continuum emission of the plasma in the spectral region adjacent to the atomic peak. This method is used, rather than absolute elemental emission, to reduce the effect of shot to shot variations in plasma energy [20]. Calibrations are performed by sampling particle-laden streams of known metal concentration, and measuring the P/B ratio. Streams of known concentration are generated by nebulizing reference standard metal solutions using a constant output atomizer (TSI model 3075). To control the concentration of the stream, the output of the atomizer is diluted with filtered, dry air, and for Na, Ca, and Mg the concentration of the solution is also varied to increase the range of the calibration. The total flow passes through a diffusion dryer to ensure that the particles are dry.

The metal concentration in the output stream of the atomizer is determined by sampling with a Scanning Mobility Particle Sizer (SMPS). The SMPS calculates the total volume of particulate matter per unit volume of the carrier gas, based on a measured electrical mobility diameter and the assumption of spherical particles. This procedure should be relatively accurate for dry particles. The composition of the particles is assumed, to deduce density and mass fraction of the metal species. For most of the calibrations, particles are assumed to be composed of the most common oxide of the metal. For sodium, a sodium chloride solution is used, which is assumed to form NaCl particles. The reported total particulate volume is then multiplied by the density of the particle and the mass fraction of the element of interest to yield the mass of the element per volume of gas.

Ensemble averages of 1000 laser shots were used to determine the P/B ratio for a given concentration. Data points were fit with a linear regression, and regression coefficient ($R^2$) values ranged from 0.97 to 0.99 for the seven calibrations. The calibration curve for the Ca (II) line at 422 nm is shown as a representative example (Figure 4.2).

*4.2.3 Data Acquisition and Analysis*

Data was acquired during a one week period from August 26 to September 2, 2002. The system was run continuously for most of the period, with occasional breaks taken to perform minor maintenance and data backup. The system continuously cycled through four spectral windows, acquiring 2000 shots in just under two minutes per window. The spectrometer position and the timing of the camera were controlled by computer, allowing the system to be fully automated.

The concentrations of seven metals (Al, Ca, Cr, Cu, Mg, Mn, Na) were measured during the week long sampling period. A spectral region of approximately 40 nm can be monitored at any given time, so elements can be measured simultaneously only if they have emission lines close to each other. To monitor a larger number of elements, spectral regions must be scanned, resulting in a loss of temporal resolution. The choice of metals was based on their prevalence in the atmosphere, the strength of their LIBS signal, and the location of their emission lines, in an attempt to acquire the greatest amount of useful data in a limited time period.

Time averaged element concentrations were determined using a conditional averaging technique [21]. For each laser shot, the P/B ratio is calculated. If the P/B ratio is greater than the detection threshold, the spectrum is considered a "hit," meaning there was a particle present in the plasma. The concentration of the element within the sample volume of the plasma is calculated for that shot and saved. If the P/B ratio is below the detection limit, it is considered to contain no particle. In a given time period, the average concentration of the hits times the number of hits is divided by the total number of shots to determine the average concentration.

In this study, the hit rates were very low, so even a small rate of false hits would significantly influence the calculated concentration. For this reason a relatively high threshold was used to determine hits. The threshold for each element was set by taking several thousand spectra in filtered air, and increasing the threshold for a particular line until no hits were recorded. This yielded a higher selectivity than the standard $3\sigma$ criterion for signal-to-noise. The resulting thresholds correspond to signal-to-noise ratios of about 4 to 5, and thus the probability of false hits is minimal.

Along with elemental concentrations, the LIBS technique can provide information about particle mass distributions. The LIBS signal is proportional to the concentration of analyte within the plasma volume. If the concentration is multiplied by the plasma volume, the mass of analyte can be calculated. When a single particle is hit, the mass of analyte within the plasma is equal to the mass of analyte in the sampled particle. In this manner, the particle mass distribution of a given element can be determined. Given a dilute particle phase, the probability of a multiple particle hit is roughly the square of the single particle hit rate. As discussed below, the hit rate in these experiments is sufficiently low that the single-particle assumption is justified.

*4.2.4 Aerosol Sampling*

Ambient particulate matter was sampled at the Pittsburgh Air Quality Study Supersite in Pittsburgh, PA. The equipment was housed in a trailer located at the top of a hill in Schenley Park, adjacent to the campus of Carnegie Mellon University. Air was sampled several meters above the roof of the trailer, using a particle concentrator from Eatough's group at Brigham Young. The particle concentrator consists of a $PM_{2.5}$ cyclone inlet and a virtual impactor. The virtual impactor removes excess air, producing a flow stream with an increased concentration of fine particles. The design and characterization of the system have been previously described by Ding et al. [28] (note: the diffusion denuder and filter packs were removed for this study). In these experiments, the concentrator runs at a minor to total flow ratio of 20% and a total flow of $2.5 \times 10^{-3}$ $m^3$ $s^{-1}$ (150 l $min^{-1}$). This results in approximately a five-fold concentration of particles and a low cutoff of approximately 0.1 μm. The detection limit of the LIBS system is above

100 μm, therefore the concentrator losses should not significantly affect the LIBS performance.

After passing through the particle concentrator, the sample air is carried approximately three meters to the sampling cell of the LIBS system in 1.2 cm diameter Teflon™ lines. The sampling cell is a sealed 6 cm diameter cylindrical Teflon chamber with planar windows allowing optical access. The choice of Teflon™ may have adversely influenced our small particle hit rate due to electrostatic deposition of particles in the line; this should be avoided in future efforts of this kind. Because the repetition rate of the laser is fixed at 20 Hz and the flow rate from the concentrator was set at $5x10^{-4}$ $m^{-3}$ $s^{-1}$ (30 l $min^{-1}$) in these experiments, a section of 5/8 cm stainless steel tube was used to accelerate the flow and introduce it to the plasma. The tube was positioned so that the plasma was approximately 1 cm from the opening of the tube. This ensured that the velocity was sufficiently high that fresh gas was sampled with each laser shot.

## 4.3 Results and Discussion

### *4.3.1 Particle Hit rates*

During the week, the system ran 4552 acquisition cycles, recording 2276000 spectra in each window. Of the seven elements, Ca, Na, and Mg were the most common, with hit rates on the order of several hits per 10,000 shots. For the other elements, the frequencies were on the order of several hits per 100,000 shots. The number of hits and the hit rates for all elements are shown in Table 4.1. Presumably, the use of the particle concentrator helped to increase the sampling efficiency of the LIBS system. Unfortunately, due to time limitations, data was not acquired without the concentrator to determine its effect.

*4.3.2 Ambient Metal Concentrations*

The combination of the measured hits for each element allows the construction of an ensemble-averaged spectrum, shown for the 932 Ca hits in Figure 4.3. Ca (II) peaks are visible at 393.4, 396.8 nm, and at 422.0 nm. The average concentration of each element is calculated for the entire week, as discussed above (Table 4.2). The concentrations ranged from tens of nanograms per cubic meter for four minor elements to hundreds of nanograms per cubic meter for Na, Mg and Ca. Hourly concentrations of the three major elements are plotted in Figures 4.4a-4.4c.

Relationships between element concentrations were measured by determining the Pearson correlation coefficients between of sets of time averaged elemental concentrations. The Pearson correlation coefficient is defined as

$$R=\frac{n(\Sigma XY)-(\Sigma X)(\Sigma Y)}{\sqrt{[n\Sigma X^2-(\Sigma X)^2][n\Sigma Y^2-(\Sigma Y)^2]}} \qquad (4.1)$$

The correlation coefficients between Na, Mg and Ca are given for 1-, 4- and 12-hour averages in Table 4.3. Interestingly, magnesium shows a moderate correlation with both sodium and calcium, but sodium and calcium show essentially zero correlation. This behavior may be explained by considering the volatilities of the metals: in general, the volatility of Na > Mg > Ca. Thus for combustion-generated particles, which are the bulk of the particles containing alkali and alkaline earth elements smaller than 1 micron, one might expect Mg to share some commonality with both Na and Ca. It is also interesting that both the Mg-Na and Mg-Ca correlations get stronger for longer averaging intervals. Further study is needed to determine whether this is due to actual short time-scale

fluctuations of element concentrations, or if the hit frequencies are too low to obtain representative samples at the short time scale.

Twelve-hour Micro-Orifice Uniform Deposit Impactor (MOUDI) samples were acquired concurrently to the LIBS measurements. Those samples could be used to provide a reference for verification of the LIBS data. At the time of publication however, the MOUDI samples had yet to be analyzed, illustrating the advantage of the real time capability of LIBS.

*4.3.3 Particle Mass Distributions*

Mass distributions were determined for the elements based on particle hits. Single shot element concentrations were multiplied by a plasma volume of 0.25 $mm^3$. The Mg distribution is shown in Figure 4.5, other distributions were similar. The distributions of Na, Mg and Ca all show that the distributions are dominated by particles near the detection limit. The distributions are truncated at the mass corresponding to the conservatively-determined detection threshold of the LIBS system. The mass detection limit for each element is shown in Table 4.2. The location of the mode of the full distribution, and how far below the detection limit it would be, cannot be determined. It is likely that the LIBS system is missing a significant number of the smallest particles and thus under predicts the mass concentrations of elements. This fact is ameliorated somewhat by the fact that the elemental mass concentrations are a weighted average of the mass number distribution, and hence the larger particles contribute the most to the mass determination.

While ambient particles are typically comprised of multiple compounds, as discussed below, it may be useful to determine an equivalent size based on a pure particle

of assumed composition. For example, the mass detection limits in Table 4.2 for Ca and Mg would correspond to 342 nm CaO and 360 nm MgO particles. The ultimate mass concentration detection limit, which would be expressed in μg $m^{-3}$, is difficult to define for a LIBS monitor, due to the fact that discrete particle hits may be followed by an arbitrary number of non-hits. Each "miss" acts to lower the effective mass concentration detection limit by increasing the volume sampled. Hence the mass concentration detection limit depends both upon the particle size distribution and the mass detection limit.

*4.3.4 Multiple-Element Spectra*

Several individual spectra contained signal from more than one element. These multi-element spectra illustrate the potential for LIBS to determine complete particle composition and associations between elements. Figure 4.6 shows a single particle containing Ca, Mn and Cr. Several other particle types were observed, including predominantly Mg particles with several additional species such as Si, Ca / Al particles, and Fe / Cu / Cr particles. Echelle spectrometers providing spectral coverage from UV to NIR have recently become available. Successful implementation of such a device in a LIBS system could greatly improve the usefulness of LIBS for measurement of atmospheric particulate matter. In fact, an initial attempt was made by the authors to measure ambient particulate matter with an echelle spectrometer at the Supersite. Unfortunately the optical efficiency of this particular spectrometer was very poor, and single particles could not be detected. As the sensitivity of the LIBS technique improves, and with the use of large bandwidth echelle spectrometers, useful estimates of total composition and size (requiring assumptions about density and molecular composition)

of single particles could potentially emerge, and source apportionment using the methods of Hopke and co-workers, e.g. [12] could be implemented.

*4.3.5 Discussion*

To our knowledge, the only previous measurement of ambient particles using LIBS was performed by Hahn and co-workers [27]. Their experiments demonstrated that LIBS could detect increased levels of Mg and Al introduced by fireworks displays during the July 4$^{th}$ holiday. They measured the daily concentrations of Mg, Na, Al, and Ca for several weeks around the fourth of July, sampling roughly 4 hours per day. This current study seeks to demonstrate the capability of LIBS to characterize ambient particulate matter in greater detail, by measuring an extended list of elements at greater continuous temporal resolution. The data from the current study will also provide benchmark accuracy data for verification once the corresponding MOUDI data becomes available.

It is important to note that Hahn et al. reported particle hit rates one to two orders of magnitude greater than those reported here. This could be due to several factors, including either sampling issues or issues surrounding the detection limits of the system. One obvious sampling issue is that smaller particles may be trapped in the Teflon™ lines used in our experiments. In addition, environmental differences between Hahn's Florida location and our Pittsburgh location may result in substantial differences in elemental concentrations. Finally, the spark volume is expected to be roughly proportional to the laser pulse energy, and as a consequence Hahn's analytical volume should be significantly larger, as their energy is ~ 9 times greater than ours.

Considering factors influencing detection limits, the higher pulse energy used in Hahn's work results in a more repeatable plasma. Increased variability in the background

signal necessitates more conservative detection thresholds. Hahn et al. also could have used a slightly more efficient optical setup for collecting light from the plasma or more optimal detection timing. In addition, they did use a different data processing technique, triggering on one emission line and quantifying using a second line. This method minimizes the influence of false hits, allowing lower thresholds, but can only be applied when more than one line is visible.

Overall, increases in sensitivity yield a greater ability to determine a complete picture of the particle mass distribution, and comparisons indicate that there is room for improvement in our current system. With better detection limits, and correspondingly higher hit rates, improved measurements of the particle mass distribution are certainly possible. However, given the fact that the mass is predominantly in the larger particles, the mass concentrations determined here, based on particles of roughly 300 – 400 μm in diameter and larger, are likely to be close to the actual values.

**4.4 Conclusions**

This work has illustrated the usefulness of LIBS for long-term measurements of multiple elements in ambient air. These methods are equally applicable to thermal process streams or other situations where dilute particle suspensions mass and composition are of interest. Weekly and hourly mass concentrations illustrate the efficacy of the LIBS technique for temporal measurements, and the potential for LIBS to reveal elemental associations that may be important for understanding chemistry or for source apportionment. Particle mass distributions were limited in this work by the threshold detection limit, illustrating the importance of optimizing laser pulse energy, detection timing, and optical design to lower the detection threshold. However, mass

concentrations determined here are likely to be largely correct, due to the preponderance of the mass in the larger size particles. Multi-element spectra suggest the potential of LIBS as a means for understanding particle formation chemistry through observed elemental affinities, and for source apportionment.

**4.4 Acknowledgement**

Chapter 4, in full, is a reprint of material as it appears in Atmospheric Environment, vol. 38, no. 20, p. 3319, 2004, Lithgow, G.A., Robinson, A.L., and Buckley, S.G.

**Table 4.1.** Number of recorded hits and particle hit rates for experiments conducted from August 26, 2002 – September 2, 2002.

| Element | Ca | Na | Mg | Cr |
|---|---|---|---|---|
| Total Hits | 932 | 836 | 327 | 52 |
| Total Shots | 2276000 | 2276000 | 2276000 | 2276000 |
| Hit Rate | 0.0004407 | 0.0002869 | 0.000157 | 1.8E-05 |

| Element | Al | Cu | Mn |
|---|---|---|---|
| Total Hits | 40 | 56 | 70 |
| Total Shots | 2276000 | 2276000 | 2276000 |
| Hit Rate | 1.757E-05 | 3.207E-05 | 3.08E-05 |

**Table 4.2.** Weekly average concentrations for measured elements (ng $m^{-3}$) and threshold mass detection limits (fg).

| | Ca | Na | Mg | Cu | Al | Mn | Cr |
|---|---|---|---|---|---|---|---|
| Weekly avg. | 304 | 716 | 225 | 32 | 30 | 29 | 37 |
| Mass detection limit | 50 | 143 | 53 | 15 | 184 | 176 | 166 |

**Table 4.3.** Correlation of Ca, Mg, and Na measurements at 1-, 4-, and 12-hour time scales, measured using the Pearson correlation coefficient.

| | Na : Mg | Na : Ca | Mg : Ca |
|---|---|---|---|
| 1 | 0.336111 | 0.010386 | 0.392389 |
| 3 | 0.468767 | -0.04872 | 0.609318 |
| 12 | 0.512869 | -0.10412 | 0.696781 |

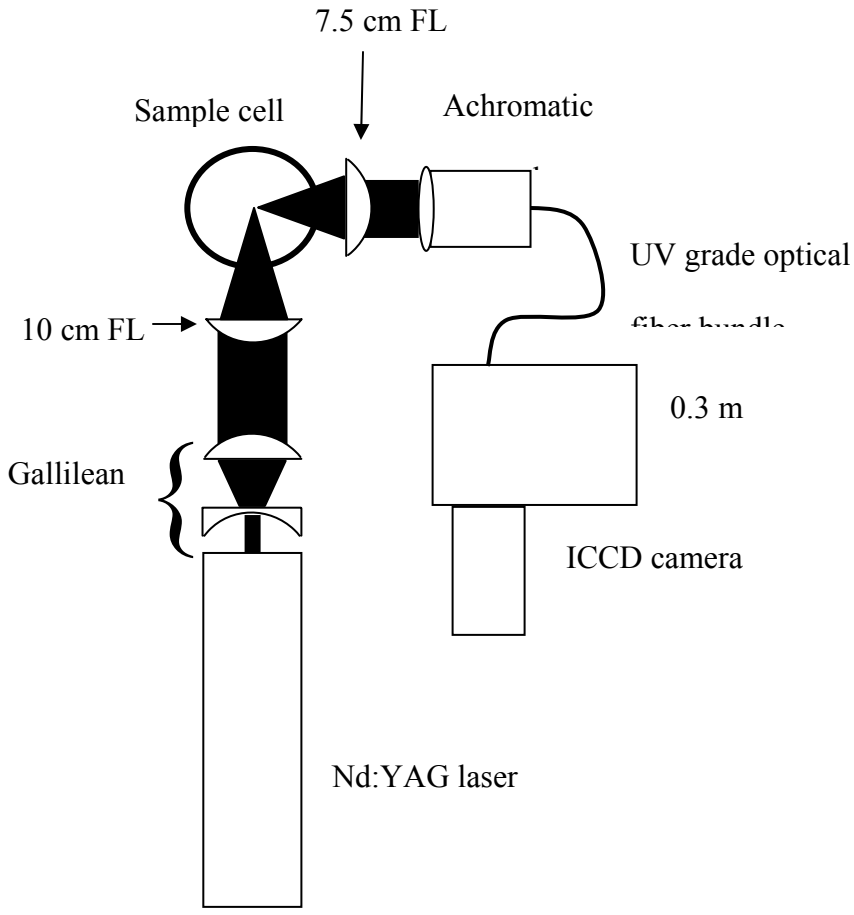


**Figure 4.1**. Experimental apparatus.

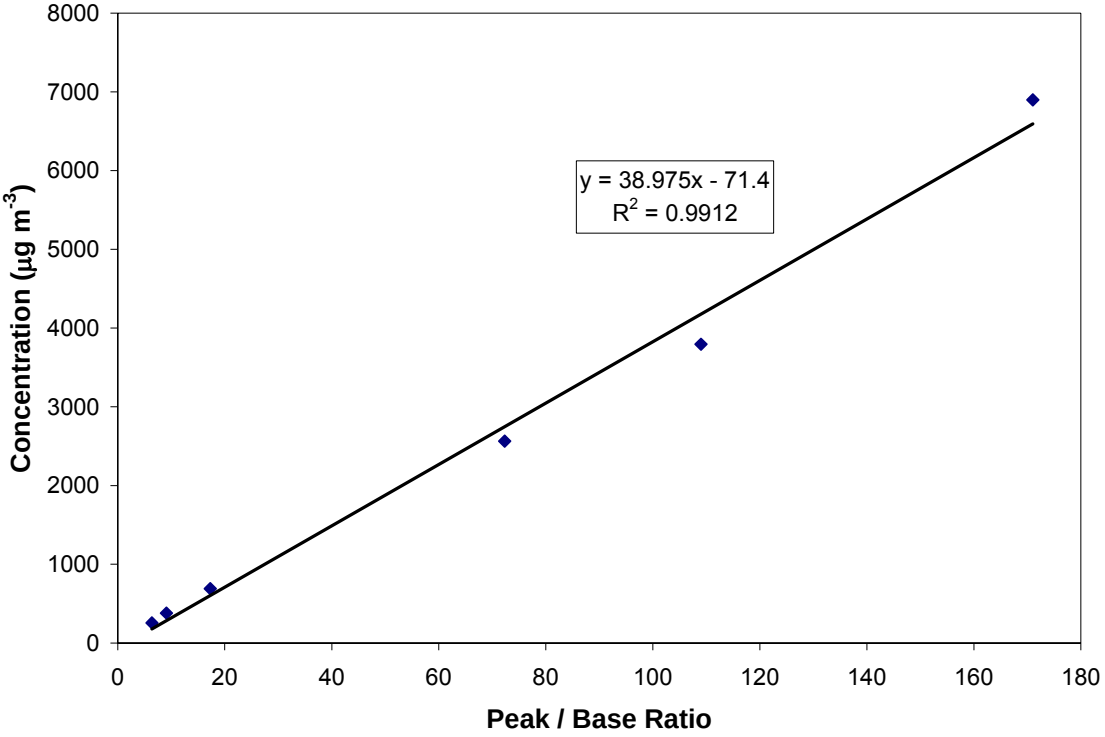


**Figure 4.2.** Calibration for Ca(II) line at 422.0 nm.

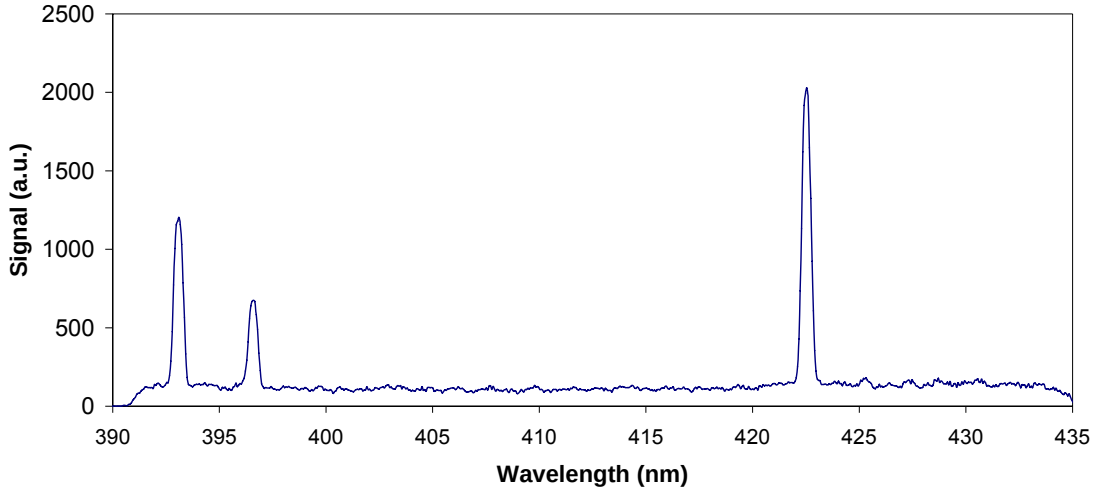


**Figure 4.3.** Averaged spectrum of 932 Ca particle hits.

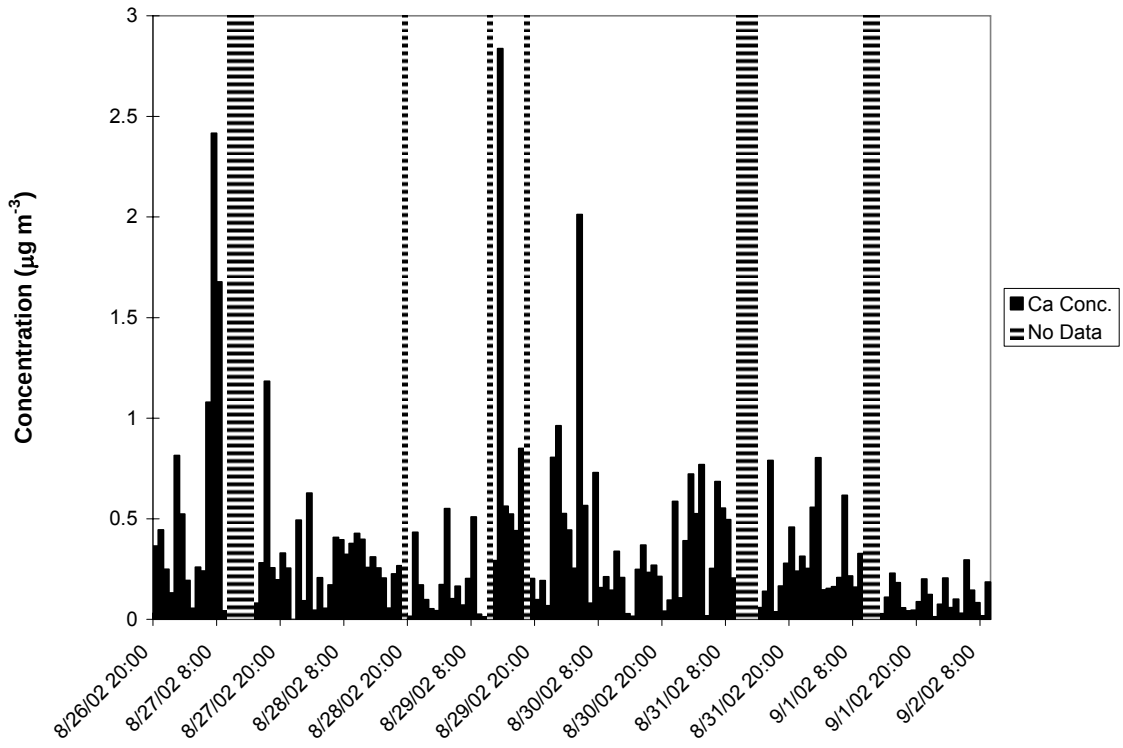


**Figure 4.4a.** Measured hourly concentrations for Ca.

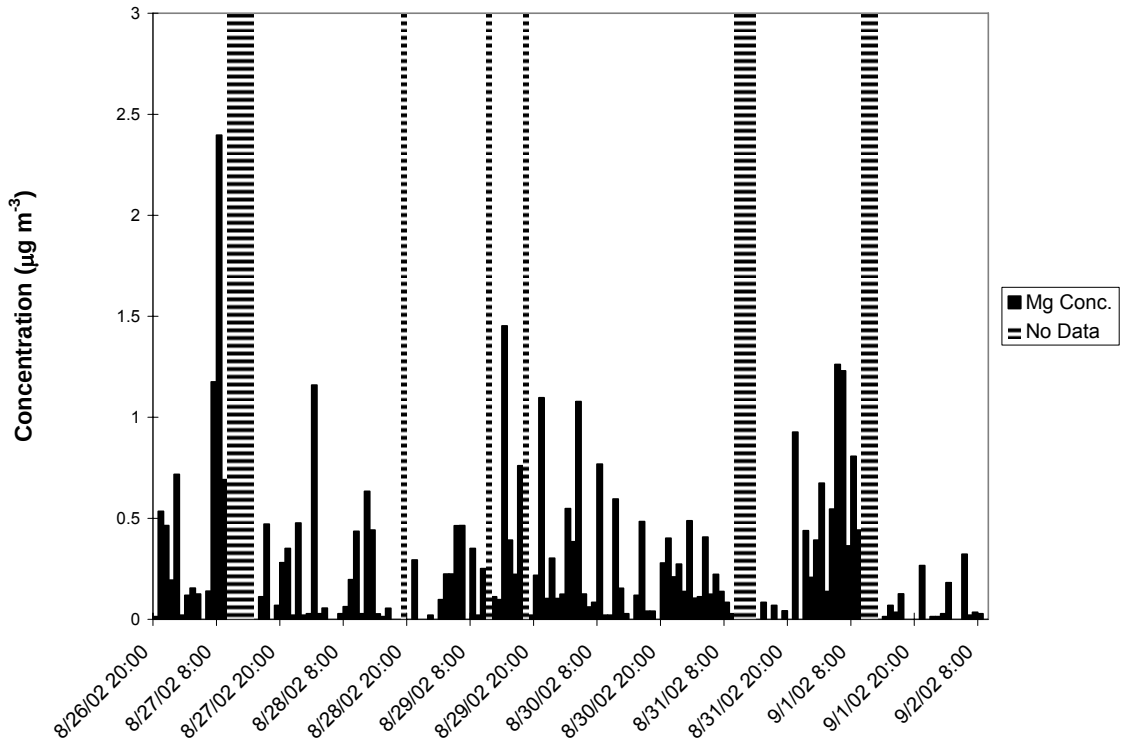


**Figure 4.4b.** Measured hourly concentrations for Mg.

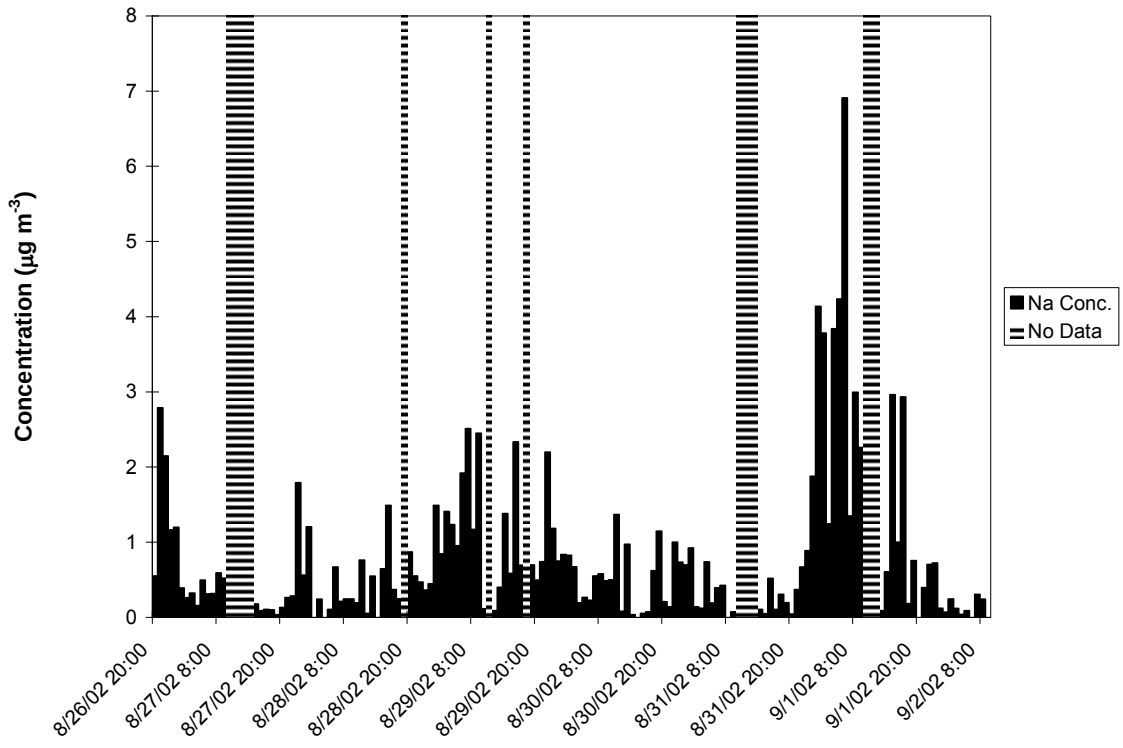


**Figure 4.4c.** Measured hourly concentrations for Na.

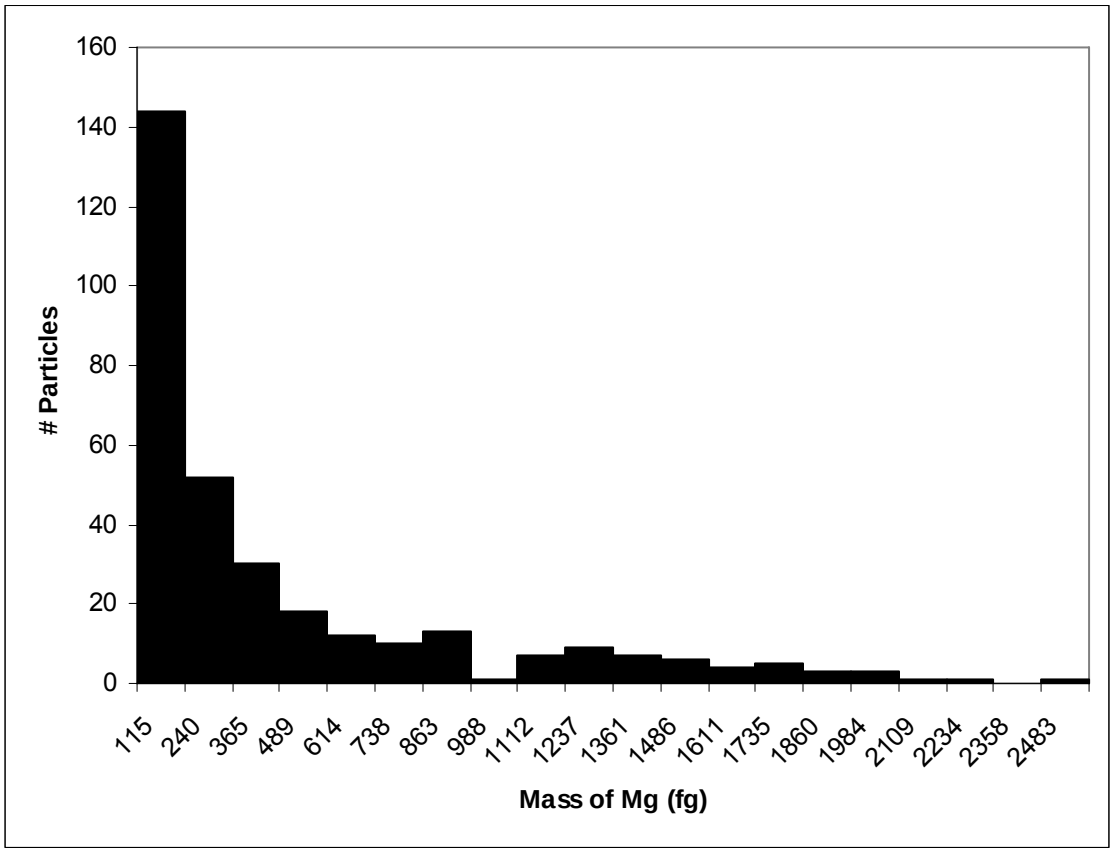


**Figure 4.5.** Distribution of Mg mass in measured particles.

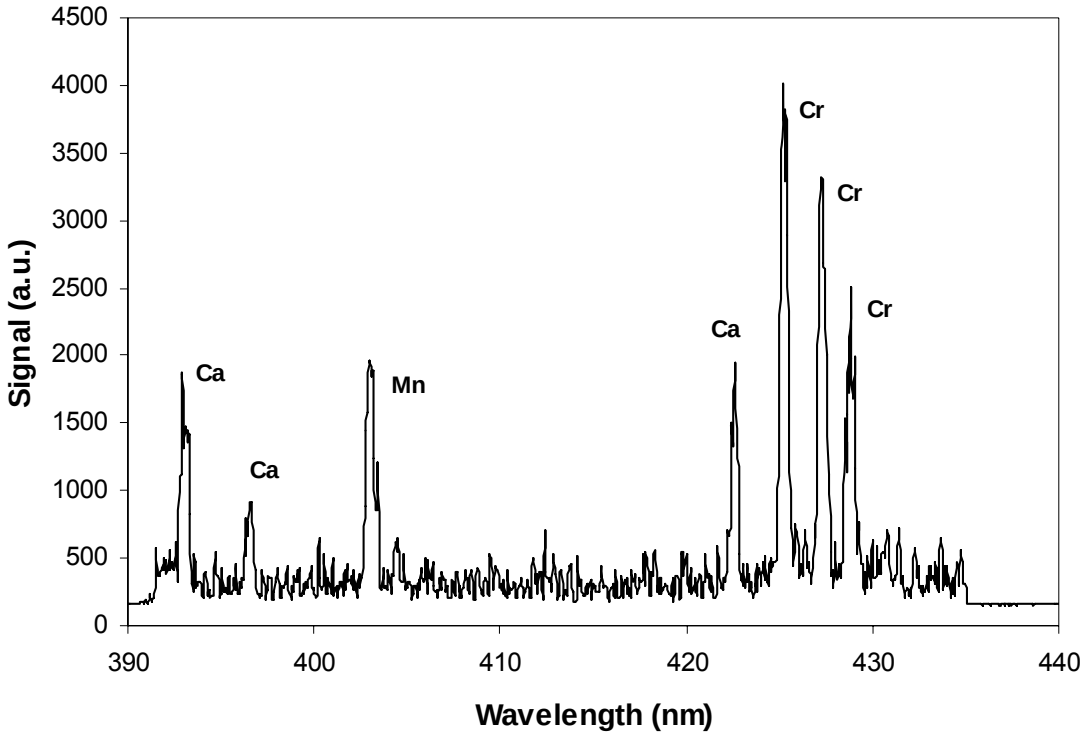


**Figure 4.6.** A multi-element particle containing Ca, Mn, and Cr.

**References**

1. D.W. Dockery, C.A.I. Pope, Acute Respiratory Effects of Particulate Air Pollution, *Annual Review of Public Health,* vol. 15, p. 107, 1994.

2. R. Brook, *et al.*, Air Pollution: The "Heart" of the problem, *Current Hypertension Reports*, vol. 5, no. 1, p. 32, 2003.

3. S. Salvi, S. Holgate, Mechanisms of particulate matter toxicity, *Clinical and Experimental Allergy*, vol. 29, no. 9, p. 1187, 1999

4. W.P. Linak, J.O.L. Wendt, Toxic metal emissions from incineration: Mechanisms and control, *Progress in Energy and Combustion Science,* vol. 19, no. 2, p. 145, 1993.

5. R.L. Davison, *et al.*, Trace elements in fly ash, *Environmental Science and Technology*, vol. 8, no. 13, p. 1107, 1974.

6. J. Chow, *et al.*, The DRI thermal optical reflectance carbon analysis system - description, evaluation, and applications in United States Air Quality Studies, *Atmospheric Environment Part A*, vol. 27, no. 8, p. 1185, 1993

7. M. Seltzer, Performance testing of a multimetals continuous emissions monitor, *Journal of the Air and Waste Management Association*, vol. 50, no. 6, p. 1010, 2000.

8. P.P. Woskov, *et al.*, Accurate and sensitive metals emissions monitoring with an atmospheric microwave-plasma having a real-time span calibration, *Waste Management*, vol. 20, nos. 5-6, p. 395, 2000.

9. C. Kidwell, J. Ondov, Development and evaluation of a prototype system for collecting sub-hourly ambient aerosol for chemical analysis, *Aerosol Science and Technology*, vol. 35, no. 1, p. 596, 2001.

10. A. Suarez, J. Ondov, Ambient aerosol concentrations of elements resolved by size and source: Contributions of some cyokine-active metals from coal- and oil-fired power plants, *Energy and Fuels*, vol. 16, no. 3, p. 562, 2002.

11. K. Prather, *et al.*, Real-time characterization of individual aerosol particles using time-of-flight mass spectrometry, *Analytical Chemistry*, vol. 66, p. 1403, 1994.

12. D. Fergenson, *et al.*, Quantification of ATOFMS data by multivariate methods, *Analytical Chemistry*, vol. 73, p. 3535, 2001.

13. D. Phares, *et al.*, Performance of a single ultrafine particle mass spectrometer, *Aerosol Science and Technology*, vol. 36, p. 583.

14. L.J. Radziemski, Review of selected analytical applications of laser plasmas and laser ablation, *Microchemical Journal*, vol. 50, p. 218, 1994.

15. I. Schechter, Laser induced plasma spectroscopy: A review of recent advances, *Reviews in Analytical Chemistry*, vol. 16, no. 3, p. 173, 1997.

16. J. Sneddon, Y.I. Lee, Novel and recent applications of elemental determination by laser-induced breakdown spectrometry, *Analytical Letters*, vol. 32, no. 11, p. 2143, 1999.

17. K. Song, *et al.*, Applications of laser-induced breakdown spectroscopy, *Applied Spectroscopy Reviews*, vol. 32, no. 3, p. 183, 1997.

18. S. Yalcin, *et al.*, Influence of ambient conditions on the laser air spark, *Applied Physics B*, vol. 68, no. 1, p. 121, 1999.

19. D.K. Ottesen, *et al*., Laser spark emission spectroscopy for *in situ*, real-time monitoring of pulverized coal combustion, *Energy and Fuels*, vol. 5, p. 304, 1991.

20. L. Xu, *et al.*, Absolute analysis of particulate materials by laser-induced breakdown spectroscopy, *Analytical Chemistry*, vol. 69, p. 2103, 1997.

21. D.W. Hahn, Laser-induced breakdown spectroscopy for sizing and elemental analysis of discrete aerosol particles, *Applied Physics Letters*, vol. 72, no. 23, p. 2960, 1998.

22. S.G. Buckley, *et al.*, Laser-induced breakdown spectroscopy as a continuous emission monitor for toxic metals in thermal treatment facilities, *Waste Management*, vol. 20, p. 455, 2000.

23. D.W. Hahn, *et al.*, Discrete particle detection and metal emissions monitoring using laser-induced breakdown spectroscopy, *Applied Spectroscopy*, vol. 51, no. 12, p. 1836, 1997.

24. H. Zhang, *et al.*, Laser-induced breakdown spectrometry as a multimetal continuous emissions monitor, *Applied Optics*, vol. 28, no. 9, p. 1459, 1999.

25. B. Fisher, *et al.*, Temporal gating for the optimization of laser-induced breakdown spectroscopy detection and analysis of toxic metals, *Applied Spectroscopy*, vol. 55, no. 10, p. 1312, 2001.

26. J.E. Carranza, D.W. Hahn, Sampling statistics and considerations for single-shot analysis using laser-induced breakdown spectroscopy, *Spectrochimica Acta Part B*, vol. 57, p. 779, 2002.

27. J.E. Carranza, *et al.*, On-line analysis of ambient air aerosols using laser-induced breakdown spectroscopy, *Spectrochimica Acta Part B*, vol. 56, p. 851, 2001.

28. Y. Ding, *et al.*, High-volume diffusion denuder sampler for the routine monitoring of fine-particulate matter: I. Design and optimization of the PC-Boss, *Aerosol Science and Technology*, vol. 36, p. 369, 2002.

# 5. EFFECTS OF FOCAL VOLUME AND SPATIAL INHOMOGENEITY ON UNCERTAINTY IN AEROSOL MEASUREMENTS

Laser-induced breakdown spectroscopy (LIBS) is emerging as a useful analytical technique for measuring the size and composition of individual aerosol particles. Recent studies have indicated that LIBS is suitable for a variety of applications including atmospheric pollution measurements [1,2], thermal process exhaust monitoring [3], and biological aerosol detection [4-8]. With the potential ability to measure the size and composition of submicron particles, LIBS is a promising new tool for aerosol science.

In some applications, LIBS can provide highly quantitative results. Calibration curves for laboratory measurements of aerosols have been found linear over a large range of analyte concentration, with small uncertainties. Such curves are typically obtained by sampling a particle-laden gas flow of known mass concentration, and averaging spectra collected from many laser shots. However, many applications require information about single particles, measured with a single laser shot, which significantly reduces the measurement precision. Hahn [9] quantified the uncertainty of single particle measurements by sampling monodisperse aerosols, illustrating both the potential of single particle LIBS measurements and the limitations due to precision in standard implementations of LIBS.

Consequently, a number of recent studies have focused on investigating sources of uncertainty in single-particle LIBS measurements. Nearly all of these studies have focused on shot-to-shot fluctuations of bulk plasma parameters such as temperature and electron density. Fluctuations in laser pulse characteristics and variations in laser-plasma interactions influence the plasma formation, and have been identified as sources of uncertainty in the LIBS signal [10-13]. It has also been observed that if a particle is too large, or if it is located at the boundary of the plasma, there will be insufficient energy transfer to completely vaporize the particle, resulting in an artificially low signal [14]. However, it has generally been assumed that species diffusion within the plasma is sufficiently fast that, once vaporized, the initial location of the particle relative to the plasma volume and the focal volume of the spectrometer collection optics is irrelevant. In this Letter, the influence of the particle location is identified as an important source of uncertainty in single-particle LIBS measurements.

In these experiments, two separate sets of optics were used to collect two simultaneous spectra from single laser-plasmas, as indicated in Figure 5.1. One set collected emissions at a right angle to the incident laser beam ("side-collection"), while the other set collected emissions backwards along the axis of the beam ("back-collection"). The side collection optics consisted of two 50 mm diameter, 75 mm focal length plano-convex UV fused silica lenses. For back-collection, plasma emission was first collimated with a lens, diverted from the laser beam path with a pierced mirror, and focused with a second lens, each identical to the side-collection optics. The two legs of a bifurcated optical fiber bundle, each leg containing 7 fused silica fibers (200 μm core diameter, 700 μm bundle diameter), were positioned at the focal points of the collection

optics to guide the light from both side- and back-collection to an imaging spectrometer for simultaneous measurement. The spectrometer (Acton Research, SpectraPro) utilized a 1200 G/mm grating, and was mated to a time-gated ICCD camera (Roper Scientific, PI-MAX). Light from each leg of the fiber bundle was dispersed separately onto two regions of the CCD array, each 85 pixels high. The plasma excitation source is a Q-switched Nd:YAG laser operating at the fundamental wavelength (1064 nm), and at 10 Hz, with a nominal pulse width of 10 ns, average pulse energy of 275 mJ, and beam diameter of 10 mm. The laser was focused with the same lens that collimated the plasma emission in the back-collection optics. The gate delay of the detector was 15 μs with respect to the laser Q-switch, and the gate width was 20 μs.

Measurements were performed in a dilute stream of magnesium chloride aerosols in air. The particles were size selected by electric mobility diameter using a differential mobility analyzer (TSI model 3080) to a mean diameter of 500 nm. The signal used to quantify the analyte present in the plasma is the integrated atomic line normalized by the continuum baseline value, which is termed the peak-to-base (P/B) ratio. A two-line conditional test [15], based on the Mg II doublet at 279.6 and 280.3 nm, was used to determine the presence of a particle signal within each collected spectrum. With no analyte present and signal due only to noise, the detection criteria resulted in false hit rates of 0.01% or less. The particle stream was diluted so that particle hits occurred on approximately 1% of the laser shots. Under these conditions, the vast majority of the collected "hit" spectra can be considered to be from plasmas containing single particles, with a small fraction containing more than one particle, and a negligible fraction of false hits. Approximately 1% of the recorded hits contained large outlying values, which were

assumed to be multiple-particle hits, and were excluded from calculations of sample mean and standard distribution values.

In the experiment, spectra were recorded from 50,000 laser shots. On each shot, both spectra were recorded. Particle hits were detected in at least one of the two spectra on 522 of the laser shots, however three different cases were observed. Signal was present in both spectra on only 220 shots (42% of the total hits, termed Case 1). Signal was present only in the side-collected spectrum on 125 laser shots (24%, Case 2), and in 177 shots, signal was present only in the back-collected spectrum (34%, Case 3). This means that 58% of the time when a particle was detected in one spectrum, it was not visible in the other spectrum. Additionally, the side-collected signal tended to be both stronger and show more variation than the back collected signal. The mean values and standard deviations of the signals for each case are given in Table 5.1.

For each pair of spectra, parameters such as the particle size and bulk plasma properties were identical. The only factor contributing to the difference between the two sets of spectra was the collection optics employed with each method. Specifically, each set of optics imaged a different region of the plasma; these experiments show that emissions are not uniform across the plasma volume. The variation between the side- and back-collection spectra illustrate that the region of strongest emission changes with each particle hit. This suggests that the ablated particle material diffuses a limited distance within the plasma, and will not be detected if it is not initially located within, or near the focal volume of the optics. The enhanced particle detection efficiency of the back-collection method is likely due to the fact that the plasma volume is elongated and the focal volume of the back-collection optics is aligned with the major axis of the

plasma, making it more likely that an ablated particle will lie within the larger focal volume of the back-collection optics than in the side-collection optics. The side-collection method shows a stronger signal, on average, than the back-collection method. This could also be due to the fact that the side-collection method images a smaller region of the plasma. When a particle is present within the side-collection focal volume, the collected emission is only from the most strongly emitting localized region of the plasma. The mean values of the signals in Cases 2 and 3 are roughly a factor of four larger than the detection threshold, and each case contains spectral signals greater than ten times the detection threshold. Hence it is not true that only the very small particles with weak signals populate Case 2 and Case 3, it is common for a large particle to go undetected on one channel but be detected on the other.

Further illustrating the effects of particle location, the 220 shots from Case 1 are plotted in Figure 5.2. In this plot, each point represents a single laser shot, with the side-collected signal plotted on the x-axis, and the back-collected signal plotted on the y-axis. Ideally, the two methods would be well correlated, but the actual measurements show no correlation. The amount of scatter illustrates the measurement uncertainty due to particle location.

The signal values from the set of side-collected measurements, $S_i$, and back-collected measurements, $B_i$, along with the standard deviations, $\sigma_S$ and $\sigma_B$ respectively, can be used to obtain an estimate of the uncertainty of each method. Additionally, we define the difference $D_i = S_i - KB_i$, where K is the ratio of the mean value of $S_i$ to the mean value of $B_i$, and calculate $\sigma_D$, the standard deviation of $D_i$. By assuming that the uncertainty due to particle location is independent of particle size, it is possible to

eliminate the particle size and shot-to-shot uncertainty from the equations relating the observed variance in the signals, yielding the uncertainty due to particle location with respect to the optics. The variances due to the particle location for each collection method $\sigma_L$ are given by

$$\sigma_{L,B}^2 = (\sigma_D^2 + K^2\sigma_B^2 + \sigma_S^2)/ 2K^2, \text{ and} \quad (5.1)$$

$$\sigma_{L,S}^2 = \sigma_D^2 - K^2\sigma_{L,B}^2. \quad (5.2)$$

From these equations, the uncertainty of the side-collected method is found to be $\sigma_{L,S}$ = 4.7, and for the back-collected method, $\sigma_{L,B}$ = 2.8. These correspond to relative standard deviations of 59% and 46% for the side- and back-collection methods respectively.

These results demonstrate that variation in particle location relative to the focal volume of the optics has strong influence on the resulting LIBS signal. The enhanced precision of the back-collection method over the side-collection method indicates that imaging a larger region of the plasma integrates spatial variations and reduces the uncertainty. Therefore, one approach to improving the measurements is to simply image a larger region of the plasma. It is important to note that the fiber bundles used in this study are smaller than the 19-fiber bundles commonly used in LIBS, resulting in a smaller imaged region than is typical. This is consistent with the fact that the results of Hahn [9] apparently show superior precision to those presented here.

However, these results suggest a second approach to improving the precision of aerosol measurements with LIBS. The observation of spatial variations in the plasma emission suggests that more information would be available with spatially resolved

measurements. Specifically, spatially resolved measurements would give insight into the transport processes occurring within the plasma. With knowledge of the distribution of the analyte material, the relative efficiency of the collection optics could be accounted for. Furthermore, it has been demonstrated that the plasma properties vary across the plasma volume, and that analyte emission varies with plasma properties. With spatially resolved measurements, proper integration of the signal would incorporate these spatial variations. Finally, a more sophisticated hit detection threshold could be developed to exclude particles located at the edge of the plasma, which may not be fully vaporized, or to determine whether multiple particles are present. The results presented here suggest that there is significant room for improving the precision of single-particle LIBS measurements. Properly accounting for spatial gradients by employing spatially resolved measurements could be an important step towards fulfilling the potential of LIBS for single-particle composition measurements in real applications.

**5.1 Acknowledgement**

Chapter 5, in full, is a reprint of material as it appears in Applied Physics Letters, vol. 87, no. 1, art. no. 011501, 2005, Lithgow, G.A., and Buckley, S.G.

**Table 5.1.** Mean values and standard deviations of the side-collected and back-collected Peak-to-Base ratios for the data sets in which a particle was detected by both methods (Case 1), or by only one method (Cases 2 and 3).

| | Case 1 | | Case 2 | Case 3 |
|---|---|---|---|---|
| | Side | Back | Side | Back |
| Mean | 7.96 | 6.15 | 4.94 | 3.64 |
| Std. Dev. | 5.23 | 3.34 | 2.89 | 2.12 |

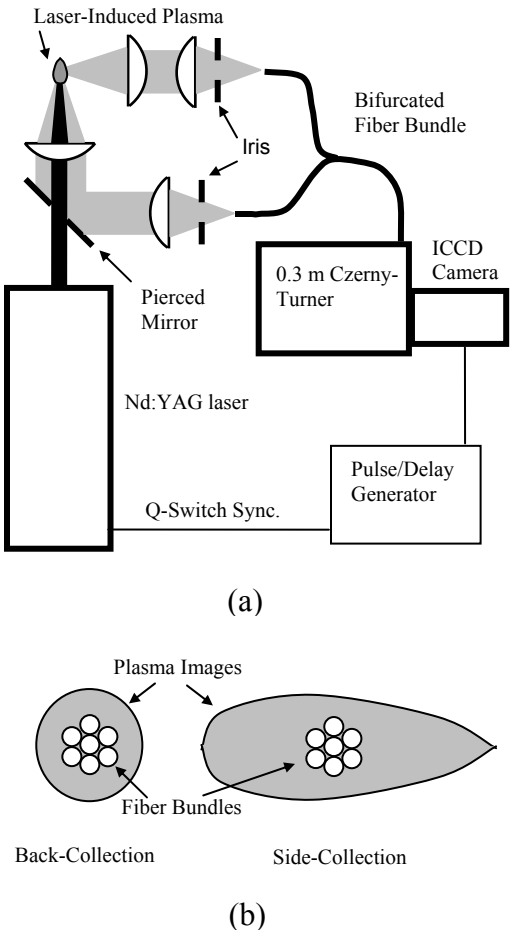


**Figure 5.1.** (a) Schematic of experimental apparatus. (b) Location of plasma images with respect to the tips of the fiber bundles.

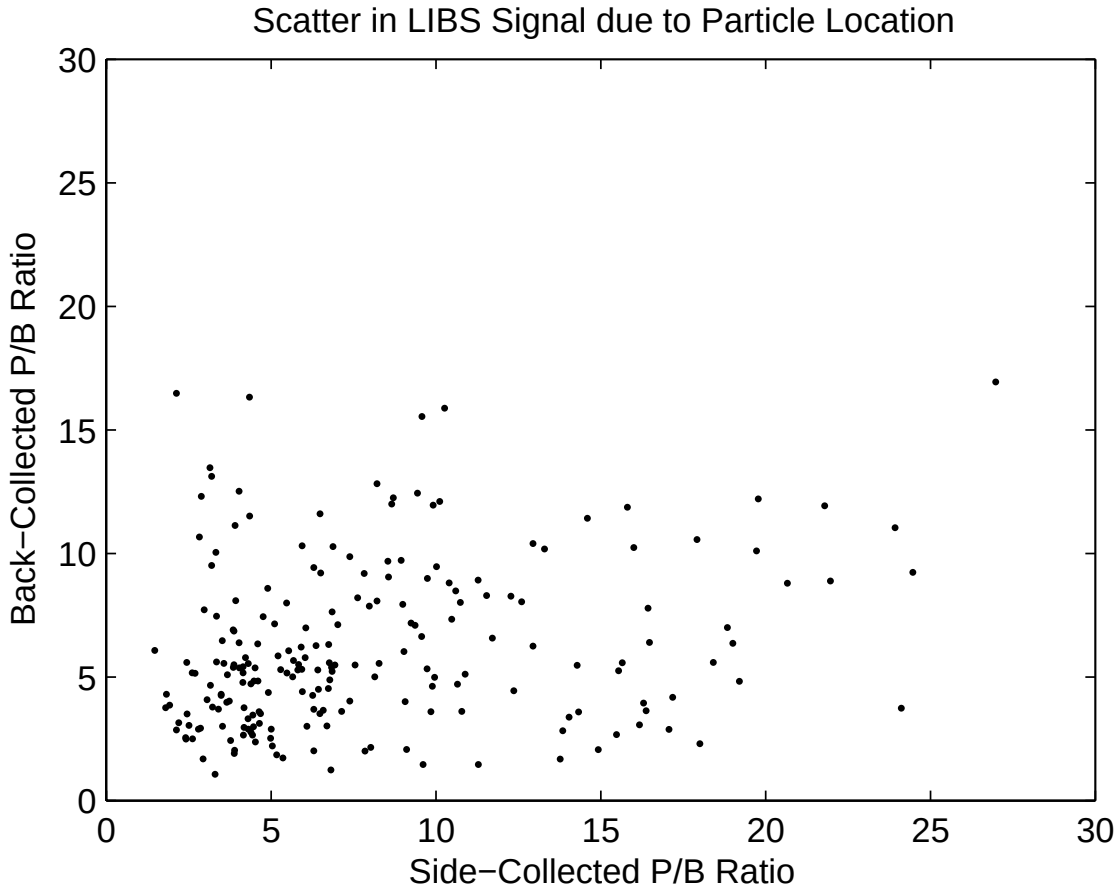


**Figure 5.2.** Side- and back-collected particles signals show no correlation. Each point represents a single particle with the side-collected signal on the x-axis and the back-collected signal on the y-axis.

**References**

1. J.E. Carranza, B.T. Fisher, G.D. Yoder, and D.W. Hahn, *Spectrochim. Acta Part B*, vol. 56, p. 851, 2001.

2. G.A. Lithgow, A.L. Robinson, and S.G. Buckley, *Atmos. Environ*., vol. 38, p. 3319, 2004.

3. S.G. Buckley, H.A. Johnsen, K.R. Hencken, and D.W. Hahn, *Waste Man*., vol. 20, p. 455, 2000.

4. J. Hybl, G.A. Lithgow, and S.G. Buckley, *Appl. Spectrosc*., vol. 57, no. 10, p. 1207, 2003.

5. S. Morel, N. Leone, P. Adam, and J. Amouroux, *Appl. Optics*, vol. 42, no. 30, p. 6184, 2003.

6. A. Boyain-Goitia, D.C.S. Beddows, B.C. Griffiths, and H.H. Telle, *Appl. Optics,* vol. 42, no. 30, p. 6119, 2003.

7. A.C. Samuels, F.C. DeLucia Jr., K.L. McNesby, and A.W. Miziolek, *Appl. Optics,* vol. 42, no. 30, p. 6205, 2003.

8. P.B. Dixon and D.W. Hahn, *Anal. Chem*., vol. 77, no. 2, p. 631, 2005.

9. D.W. Hahn, *App. Phys. Lett*., vol. 72, no. 23, p. 2960, 1998.

10. V. Hohreiter, J.E. Carranza, and D.W. Hahn, *Spectrochim. Acta Part B*, vol. 59, no. 3, p. 327, 2004.

11. C.V. Bindhu, S.S. Harilal, M.S. Tillack, F. Najmabadi, and A.C. Gaeris, *J. Appl. Phys.*, vol. 94, no. 12, p. 7402, 2003.

12. C.V. Bindhu, S.S. Harilal, M.S. Tillack, F. Najmabadi, and A.C. Gaeris, *Appl. Spectrosc*., vol. 58, no. 6, p. 719, 2004.

13. V. Hohreiter, A.J. Ball, and D.W. Hahn, *J. Anal. Atom. Spectrom*., vol. 19, no. 10, p. 1289, 2004.

14. J.E. Carranza and D.W. Hahn, *Anal. Chem*., vol. 74, no. 21, p. 5450, 2002.

15. D.W. Hahn, W.L. Flower, and K.R. Hencken, *Appl. Spectrosc*., vol. 51, no. 12, p. 1836, 1997.

# 6. INFLUENCE OF PARTICLE LOCATION WITHIN PLASMA AND FOCAL VOLUME ON PRECISION OF SINGLE-PARTICLE MEASUREMENTS

## 6.1 Introduction

Recently, a number of studies have investigated the use of LIBS for quantitative measurement of single aerosol particles. Particles of interest include exhaust from thermal processes [1], ambient particulate matter [2, 3] and biological aerosols [4-7]. The fact that LIBS is a relatively fast, simple, and inexpensive technique makes it very attractive. When information about individual aerosol particles is desired, ensemble averaging is not useful, so the success of the technique relies on the precision of single-shot measurements.

Recent studies have begun to address the precision of single-shot measurements. Most of this work has focused on shot-to-shot variations in the bulk properties of the laser plasma, such as temperature and electron density. The laser pulse characteristics [8], interactions of the laser pulse with the plasma [9, 10], and interaction of the plasma with particles [11, 12] have all been identified as factors that contribute to shot-to-shot fluctuations of plasma properties.

Previous imaging studies of plasmas supported on surfaces have revealed spatial and temporal variations to be important factors in determining the analytical performance of LIBS [13, 14]; such variations are supported by simplified plasma models e.g. [15].

Applied to aerosols, a recent [16] experimental study has shown that the location of individual particles within the plasma volume and the focal volume of the optics can also significantly contribute to uncertainty in the LIBS signal. Multiple spectra were acquired simultaneously from individual laser shots using separate collection optics. The optics collected light from different regions of the plasma and significantly different LIBS signals were observed. Since each spectrum was taken from the same plasma, the bulk plasma properties were identical, therefore shot-to-shot fluctuations did not contribute to the discrepancy in signals. This implies that the material from ablated particles does not diffuse throughout the volume of the plasma. The atomic emission of the elements of interest is not spatially uniform, and the spatial distribution is not consistent from shot to shot (i.e. there is not simply an optimum location within the plasma).

This study further investigates the role of particle location, and compares three methods of collecting light from the plasma. The previous study demonstrated that when spectra are collected from two regions of a plasma containing a particle, it is possible that one spectrum can record a strong signal, while the other spectrum records no signal. In this study, the effects of imaging larger areas of the plasma on the particle hit rates are investigated. Also, spatially resolved measurements are made to investigate mass transport within the volume, and to develop improved particle detection methods.

## 6.2 Experimental

### *6.2.1 LIBS system*

A schematic of the experimental apparatus is shown in Figure 6.1. The plasma excitation source is a Q-switched Nd:YAG laser operating at the fundamental wavelength

(1064 nm), and at 10 Hz, with a pulse width of 10 ns and average pulse energy of 275 mJ. The 10 mm diameter beam is focused with a 75 mm plano-convex fused silica lens. Two sets of optics simultaneously collect plasma emissions into two separate detectors. One set collects emissions at a right angle to the incident laser beam, while the other collects emissions along the axis of the incident laser beam. Details of the optics are given below in Section 2.2. Each detector system consists of a 0.3 m imaging spectrometer (Acton Research, SpectraPro) with a 1200 G/mm grating, mated to a time-gated ICCD camera (Roper Scientific, PI-MAX). The two cameras are synchronized with a pulse/delay generator (Berkeley Nucleonics) triggered by the laser Q-switch. In this work, the gate delay is 15 μs with respect to the Q-switch and the gate width is 20 μs for each camera.

*6.2.2 Collection optics and plasma imaging techniques*

Under the given excitation conditions, and at the given delay times, the plasma has a long axis of approximately 5 mm along the laser beam axis, and is approximately 2 mm across in the transverse direction. These dimensions were determined by measuring the integrated continuum plasma emission collected with a single fiber. The fiber was translated across the plasma image, and the limits were defined at the points where emission was no longer visible. More detailed measurements of the plasma dimensions were not undertaken in this study, for full treatment of plasma volume considerations see [17]. Three data sets were acquired (Cases 1, 2, and 3), and in all experiments, plasma emission was collected simultaneously with two sets of optics, one at 90° to the incident laser beam (referred to as the side-collection method), and the other at 180° (referred to as the back-collection method). In each case, the side-collection optics were changed to image the plasma in a different manner, while the back-collection optics were unchanged

and used as a reference. In all cases the side-collection optics used two 50 mm diameter, plano-convex, UV-grade fused silica lenses to focus the plasma emission onto a UV fused silica fiber bundle, which guided the light to the entrance slit of the spectrometer. An iris was placed between the second lens and the fiber to ensure a relatively sharp image of the plasma at the tip of the fiber bundle, restricting the F# to approximately 3.

For Case 1, the two side-collection lenses were identical, each with a focal length of 75 mm, giving a magnification ratio of M = 1. The first lens was placed at a distance from the plasma equal the focal length. A large fiber bundle consisting of 19 fibers of 300 μm core diameter was used, with a total bundle diameter of approximately 2.5 mm. These fibers were not tightly packed, the bundle actually consisted 37 fibers, but only 19 randomly selected fibers were directed to the spectrometer slit. The fibers were arranged in a circular configuration on one end of the bundle, and two straight rows on the end attached to the spectrometer. The bundle was located so that light from only one row of fibers entered the slit of the spectrometer. With this configuration, the entire height of the CCD chip was utilized. Collecting light from both rows of the fiber bundle would have required increasing the width of the entrance slit, resulting in an unacceptable loss of spectral resolution. The long axis of the plasma image was significantly larger than the fiber bundle, so the bundle was located at the point of maximum intensity, as measured by the integrated continuum emission.

In Case 2, the first collimating lens was replaced with a 150 mm focal length, 50 mm diameter lens, resulting in M = 0.5. Again, the first lens was placed at a distance from the plasma equal to its focal length. In this case, the length of the plasma image was approximately equal to the bundle diameter, ensuring that light was collected from nearly

the entire plasma volume. For each of the first two cases, light from all of the fibers was integrated by binning all rows of the CCD chip.

In Case 3, the M = 1 optics from Case 1 were used to focus the light onto a linear array of 10 optical fibers, each with a core diameter of 500 μm. Light from each fiber was detected separately by binning 10 different regions of the CCD, each region consisting of 15 rows of pixels. In this manner, 10 spectra were collected simultaneously, each from a different region along the major axis of the plasma volume. The placement of each fiber bundle with respect to the plasma image in each case is illustrated in Figure 6.2.

As a reference, the same optics were used for the back-collection method in all cases. The laser-focusing lens (50 mm diameter, 75 mm focal length, plano-convex, UV grade fused silica) was used to collimate the emission from the plasma. The collimated light was diverted from the laser beam path with a pierced mirror (75 mm diameter mirror, 10 mm hole, enhanced-UV aluminum coating), then focused onto an optical fiber bundle with a second lens (f = 75 mm, d = 50 mm), which launched the light into the spectrometer's entrance slit. The fiber bundle consisted of 7 UV-grade fused silica fibers, each with a core diameter of 200 μm. The total bundle diameter was approximately 700 μm, which was significantly smaller than the plasma image, which was approximately 2 mm in diameter. The bundle was located at the center of the plasma image.

*6.2.3 Single particle generation and detection*

To make single-particle measurements, a dilute stream of magnesium chloride aerosols was introduced into the LIBS plasma. A high purity $MgCl_2$-water solution was atomized using a commercial pneumatic atomizer (TSI model 3076) and diluted with

HEPA filtered air. The particles were size selected by electric mobility diameter using a differential mobility analyzer (TSI model 3080). The mean diameter was 500 μm. The laser plasma sampled the particles in a free jet of the particle-laden flow introduced into open laboratory air.

Conditional data processing, similar to the method developed by Hahn [18, 19], was used to determine whether Mg was detected within the plasma for each shot of the laser. The signal used to quantify the analyte present in the plasma is defined as the integrated atomic line normalized by the continuum baseline value, and termed the peak-to-base (P/B) ratio. The Mg II lines at 279.6 and 280.3 nm were used in concert to determine the presence of Mg, and a spectrum was considered a hit if the P/B ratios of both lines were higher than threshold values. With no analyte present and signal due only to noise, the two-line criteria resulted in false hit rates of 0.01% or less. The particle stream was diluted so that particle hits occurred between 1% and 5% of the laser shots. Under these conditions, the vast majority of the collected "hit" spectra can be considered to be from plasmas containing single particles, with a small fraction containing more than one particle, and a negligible fraction of false hits. For each laser shot in Case 3, the side-collection system recorded ten spectra simultaneously. P/B ratio thresholds for each channel were determined independently to allow for changing noise signatures in different plasma regions. If any of the ten spectra contained a two-line signal above the threshold, it was considered a hit and all ten spectra were saved.

### 6.3 Results and Discussion

In a companion study [16], it was demonstrated that the measured LIBS signal can vary significantly depending on the manner in which plasma emission is collected

into the detector. When two spectra are collected from a single plasma they often show very different LIBS signals. In extreme cases, one spectra can exhibit a strong LIBS signal while the same element is completely undetectable in the other spectra from the same plasma. This is attributed only to the variation of particle location within the plasma volume, and the relative focal volumes of the collection optics. It was observed in the previous study that the back-collection method had a higher particle hit rate than the side collection method. In that case, each detector was coupled to the optics using an identical 7-fiber bundle, but the plasma image created by the side collection optics was significantly larger than that created by the back-collection method, so a smaller fraction of the plasma volume was imaged by the side-collection fiber bundle. It was hypothesized that the discrepancy in the hit rates was due to the fact that the side-collection method was collecting light from a smaller region of the plasma, and therefore it was less likely that a particle would be located within the focal volume of the optics.

The relative particle detection rates for the three imaging methods in the present study, as well as the case from the previous study, are given in Table 6.1. The particle concentrations were not exactly constant for all cases, so only relative hit rates were used as a comparison between cases. It is clear that for the three cases in which a single spectrum was taken from the side, the relative hit rate increases as the imaged area of the plasma increases. Additionally, Case 3 showed the highest hit rate of all methods, detecting almost all of the particles that were detected by either method. The improved detection efficiency of Case 3 over Case 2 is likely due to the fact that the signal is spatially resolved, rather than due to differences in imaged area. Both Case 2 and Case 3 collect light from across nearly the entire plasma image, however, in Case 2 all of the

light is integrated together. As a result a weak signal that is localized in a small region gets integrated with pure noise from the rest of the plasma, resulting in an overall signal below the detection threshold. In Case 3, if the localized signal is above the detection threshold at any of the fiber locations, the shot is recorded as a hit.

Ideally, the signals from the side- and back-collection methods would be well correlated since the signals come from the same particles. An observed systematic difference between the two signals is a reflection of the lack of precision between the imaging. In Figures 6.3a and 6.3b, the correlation of the back- and side-colleted signals are shown for Cases 1 and 2 respectively. Each point is a single shot of the laser with the P/B ratio from the side-collected spectrum on the horizontal axis, and the P/B ratio of the back-collected spectrum on the vertical axis. In both, there was very poor correlation between the side-collection and back-collection method, illustrating the limitations of the precision of one or both of the methods.

The masses of individual particles or the distribution of particle masses is not known, so the P/B ratio distributions of the different collection methods cannot be independently verified. This makes comparison of the precision of two collection methods difficult. However, it is expected that the particle masses will have a distribution centered around a value corresponding to the size selected by the DMA. Histograms of the P/B ratios of each particle hit for both the side- and back-collection signals in Cases 1 and 2 are shown in Figure 6.4 along with the mean and standard deviation of the distribution. In each case, the back collection method shows no clear peak in the distribution, the distributions are truncated at the threshold cutoff value. The side-collection methods both show a distinct peak, and have narrower distributions

compared with the back-collected signals. The back-collected distributions, using identical optics, show similar distributions, suggesting that the particle mass distributions are similar for each case. However, there is a notable difference between the side-collected distributions. Case 2, in which a larger area was imaged, shows an even narrower distribution than Case 1. This would suggest that when larger area of the plasma is imaged, the variation in the signal due variability in particle location is reduced.

At first glance, in Cases 1 and 2, the back-collection method appears to give a stronger signal on average than the side-collection method when a particle is detected by each method. This is illustrated in Figure 6.5, which shows the difference between the P/B ratio for each shot in which a particle was detected by each method for Cases 1 and 2. Positive values on the x-axis reflect spectra pairs with stronger back-collected signals, negative values reflect spectra pairs with stronger side-collected signals. The distribution shows that for any given particle, either method could give a stronger signal, but the distributions are skewed, indicating that the back collection method tends to give a stronger signal. This could indicate that the back collection method tends to collect light from a region of the plasma where conditions tend to favor stronger atomic lines, or weaker continuum emissions, producing a stronger P/B signal. However, this is better explained simply by the difference in imaged area and the fact that ablated material from a particle tends to diffuse a limited distance. With the back-collection method, a smaller area was imaged, so if a particle was located directly in the imaged region, it produced a strong signal. If the particle was located elsewhere, it was simply recorded as a miss, and does not appear in Figure 6.5. Conversely, when a larger area is imaged, a region of

weak signal is integrated along with the strongly emitting region, producing fewer hits with very strong signals, but more hits overall.

In Case 3, spatially resolved measurements were made of single plasmas. Spectra from ten locations along the length of a single plasma image, corresponding to one particle hit, are shown in Figure 6.6. Each spectra is from a different fiber in the linear array, and contains light from different locations along the length of the plasma. Very strong peaks are visible in spectra 8 and 9, with relatively weaker peaks in spectra 7 and 10, and no visible peaks in the remaining six spectra. The P/B ratio as a function of axial position along the plasma is plotted in Figure 6.7. A clear maximum is visible in the plot, indicating that the $MgCl_2$ particle was located at the position of peak signal intensity during the plasma formation.

Another particle hit is shown in Figure 6.8. Again a clear peak in the signal distribution is visible, but at a different location. The variation in Mg signal is not attributed to spatial variations in plasma properties, but rather to variations in the concentration of Mg. It should be noted that the continuum background emission is similar for each shot, indicating that the plasma location, and the position of the fibers relative to the image remain fixed. Plots of the P/B ratio distributions for several particle hits are shown in Figure 6.9. In most of the hits, a single clear peak is visible, though often it is truncated at the edge of the plasma. In some cases, the signal is distributed across the length of the plasma, indicating that sometimes the ablated material does distribute throughout the plasma volume. In other cases, a more complicated signal distribution is seen. These complicated distributions could be due either to the presence

of more than one particle within the plasma volume, or possibly to more complicated mass transport phenomena.

When the ten side-collected spectra of Case 3 are integrated and the resulting P/B ratio compared to the back-collected spectra, the distribution is again skewed towards the back-collection method (Figure 6.10a). However, if the maximum P/B ratio of the ten spectra is compared to the back-collected spectra, as shown in Figure 6.10b, the distribution becomes skewed towards the side-collected spectra. This supports the conclusion that the back-collection method does not image an optimum region of the plasma. When a small region of the plasma is imaged, the signal contains greater variability due to the location of particles, and gives excessively strong signals when particles are located within the imaged region.

These results suggest that the use of spatially resolved measurements could provide a means of improving the precision of single particle measurements. The spatial distribution of the signal gives information about the location of a particle within the plasma, and could be used as a criterion to determine whether the particle was completely vaporized in the plasma, or to reject shots that contain more than one particle. It is expected that proper spatial integration of the signal will also improve the precision of the signal. The spatial integration of the signal should take into account the effective volume imaged by each collected channel as well as spatial variations of plasma properties. Further study using completely monodisperse particles, to remove the uncertainty in particle mass distributions, is necessary to determine a proper signal integration technique.

**6.4 Conclusions**

This work illustrates the important role that plasma imaging methods play in single particle LIBS measurements. It is shown that ablated material from particles engulfed in the plasma does not diffuse uniformly throughout the plasma volume, and that emission from the particle material is not uniform across the plasma volume. This means that the location of the particle within the focal volume of the collection optics has a significant influence on the resulting LIBS signal. It is clear that when light is collected only from a limited region of the plasma volume, particles within the plasma are often undetected. Increasing the area of the plasma imaged results in improved detection efficiency. Imaging a larger area of the plasma also reduces the effect of variation of particle location within the plasma and focal volumes, giving improved precision of the measurements.

Using spatially resolved measurements provides a means of further improving single particle measurements. Spatially resolved detection thresholds used in conjunction with a large imaged area is the optimum method for maximizing particle hit detection rates. Spatially resolved measurements also give information about the location of particles within the plasma volume, and the mass transport within the plasma. This information could be used develop more sophisticated particle hit detection criteria, and improved signal precision through proper spatial integration.

**6.5 Acknowledgement**

Chapter 6, in full, is a reprint of material as it appears in Spectrochimica Acta Part B, vol. 60, nos. 7-8, p. 1060, 2005, Lithgow, G.A., and Buckley, S.G.

**Table 6.1.** Relative hit rates for each optical setup.

| | Total number of hits detected | # of hits detected only by side-collection | # of hits detected only by back-collection | # of hits detected by both methods | % of total particles detected by back-collection | % of total particles detected by side-collection |
|---|---|---|---|---|---|---|
| Previous Study | 522 | 125 | 177 | 220 | 76% | 66% |
| Case 1 | 1155 | 390 | 261 | 504 | 66% | 77% |
| Case 2 | 1435 | 633 | 191 | 611 | 56% | 87% |
| Case 3 | 684 | 298 | 33 | 353 | 56% | 95% |

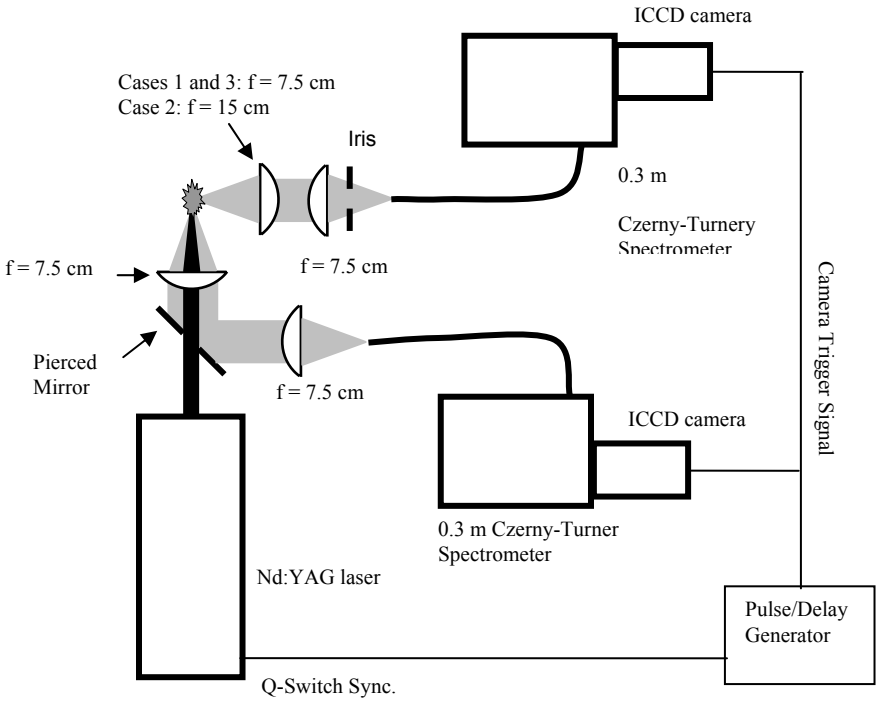


**Figure 6.1.** Schematic of experimental apparatus.

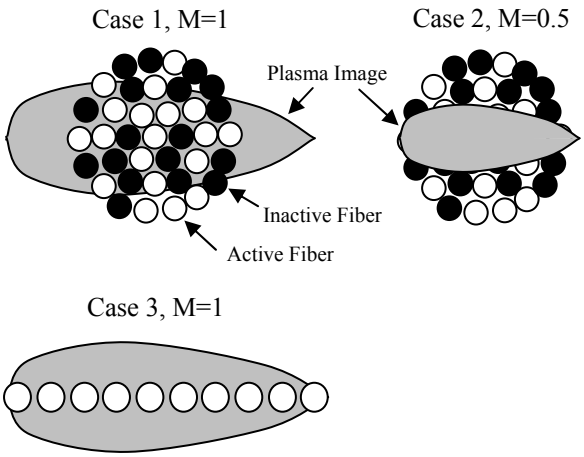


(a)

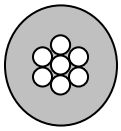

(b)

**Figure 6.2.** Location of fiber bundles with respect to side-collected (a) and back-collected (b) plasma image.

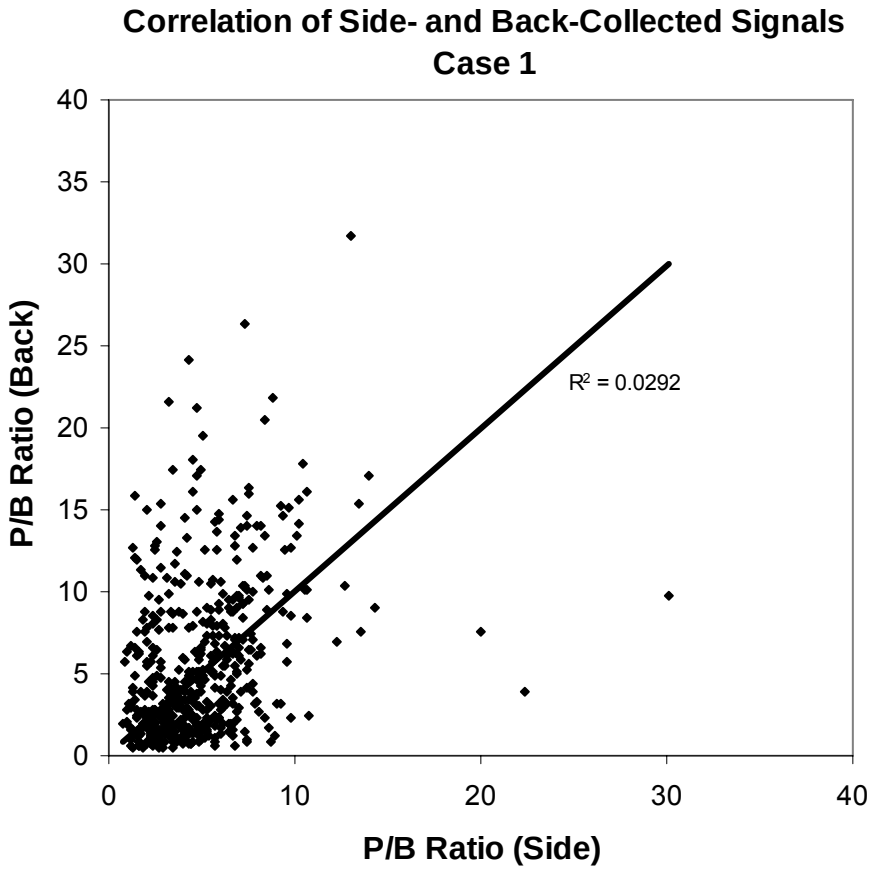


6.3(a)

**Figure 6.3.** Simultaneous side- and back-collected signals of individual particle hits show poor correlation in both for Case 1 (a) and Case 2 (b).

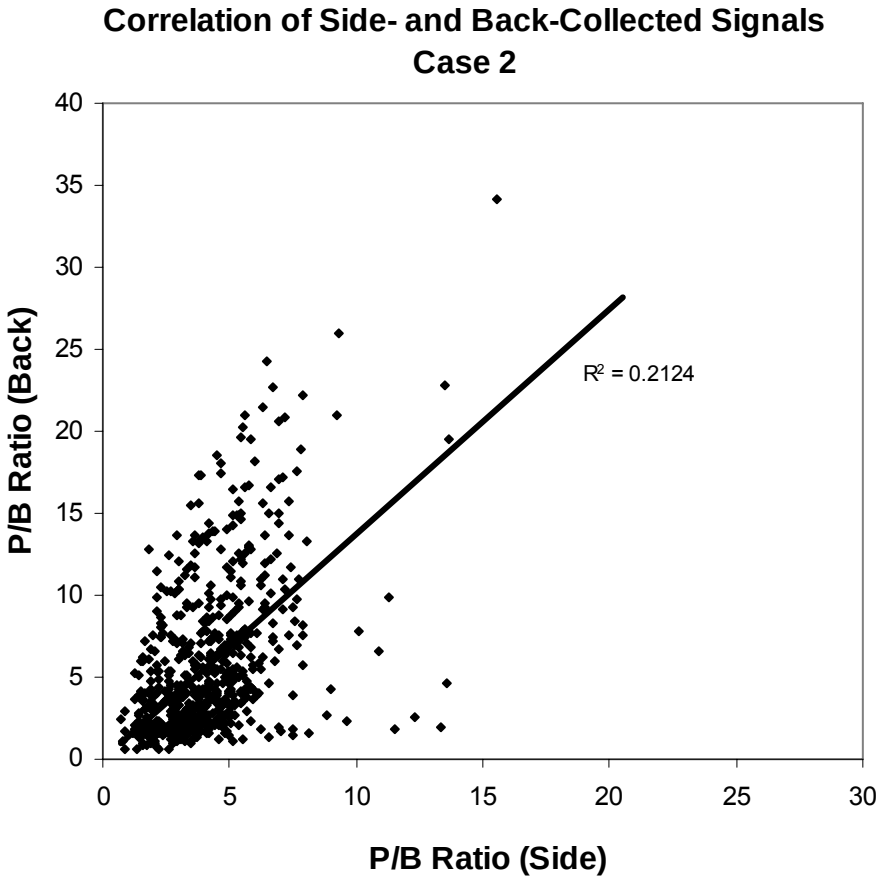


6.3(b)

**Figure 6.3.** (Continued)

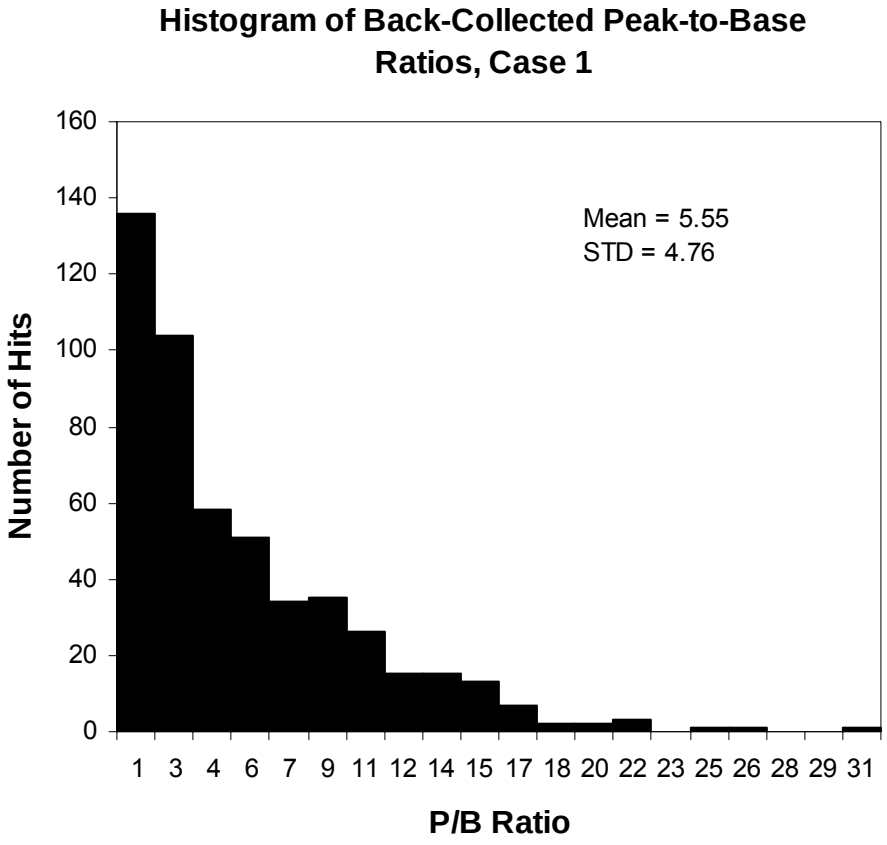


6.4(a)

**Figure 6.4.** In both cases, the single shot peak-to-base ratio distributions from the back-collection method show no clear peak (a,c), while the side-collection method shows a more normal distribution. For the side-collection method, the larger imaged area of Case 2 (d) shows a clearer peak, and a narrower distribution than smaller imaged region of Case 1 (b).

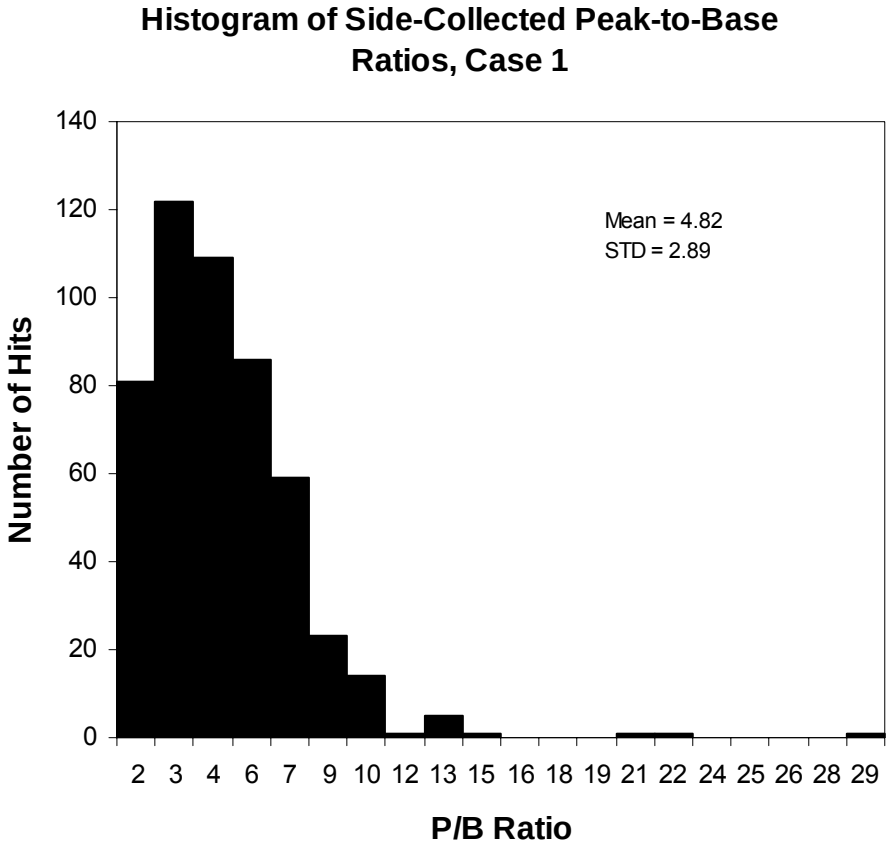


6.4 (b)

**Figure 6.4.** (Continued)

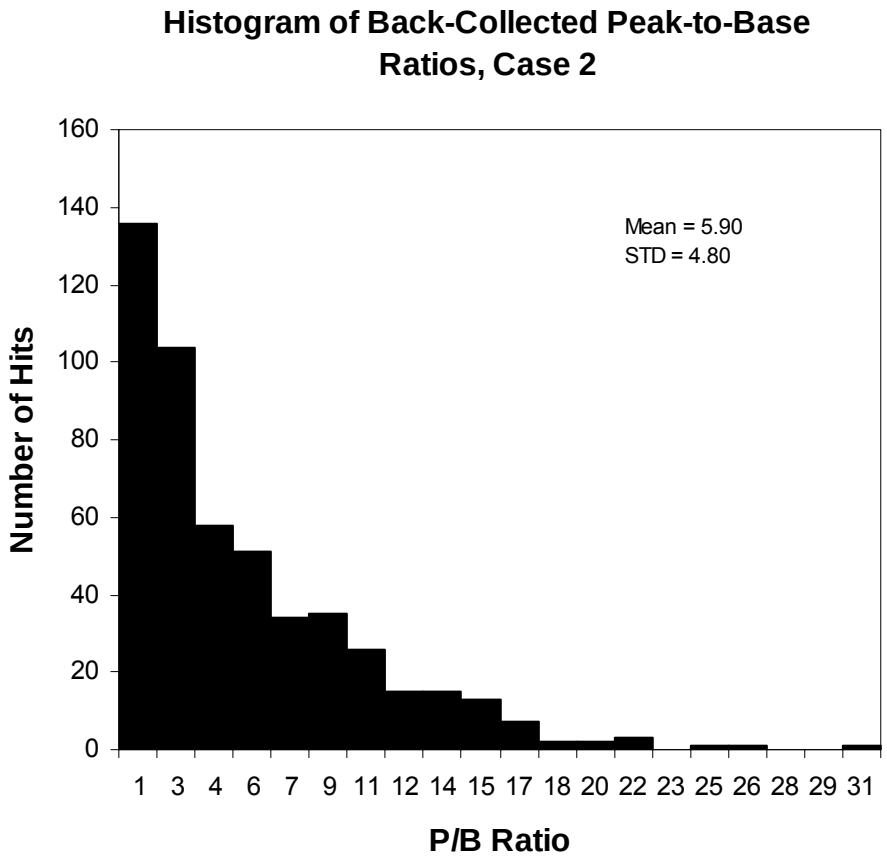


6.4 (c)

**Figure 6.4.** (Continued)

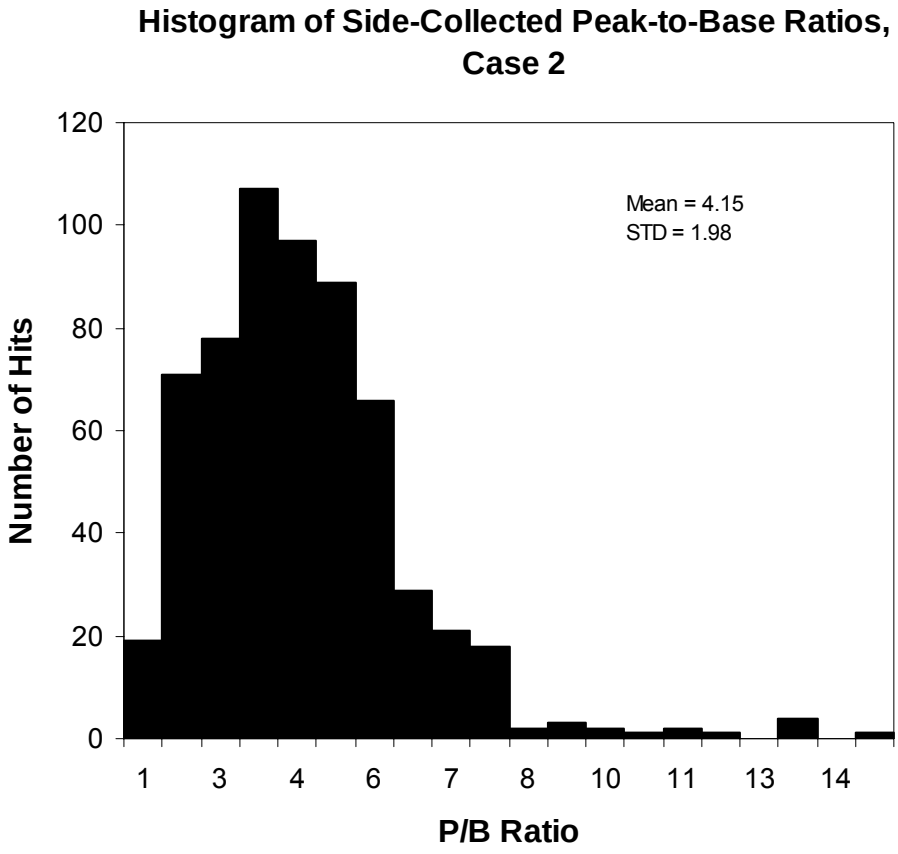


6.4(d)

**Figure 6.4.** (Continued)

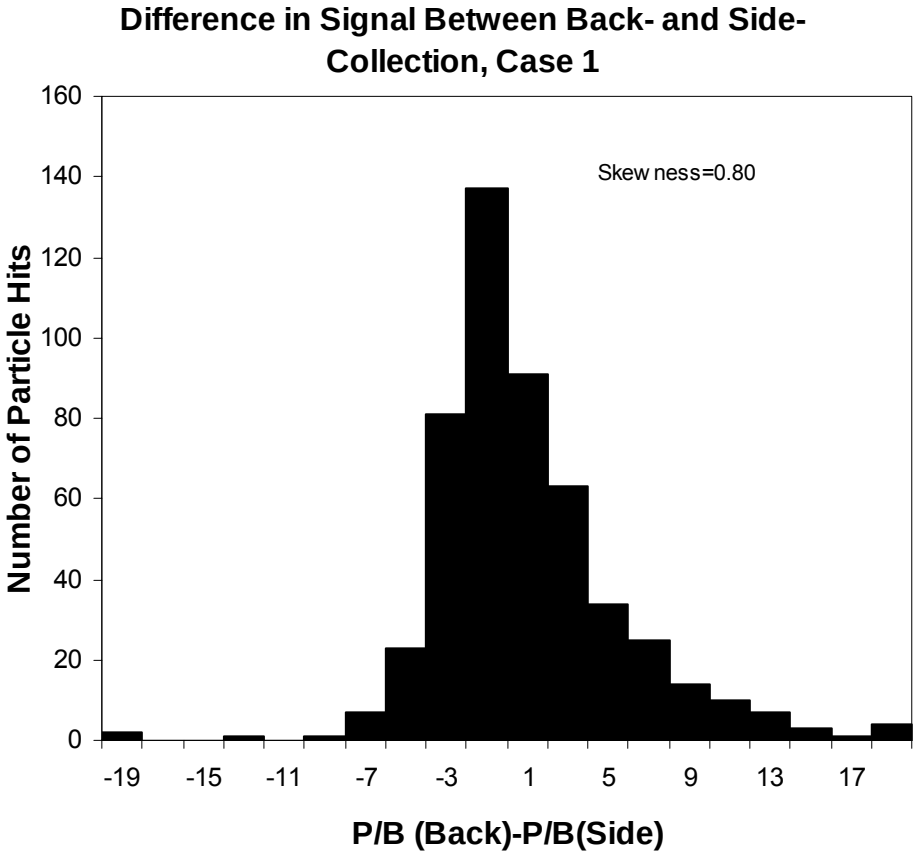


6.5(a)

**Figure 6.5.** The strength of simultaneous side- and back-collected signals from individual laser shots tends to show a bias toward the back-collected method. When a larger area is imaged with the side-collection optics in Case 2 (b), the distribution shows a stronger bias towards the back-collected signal than in Case 1 (a).

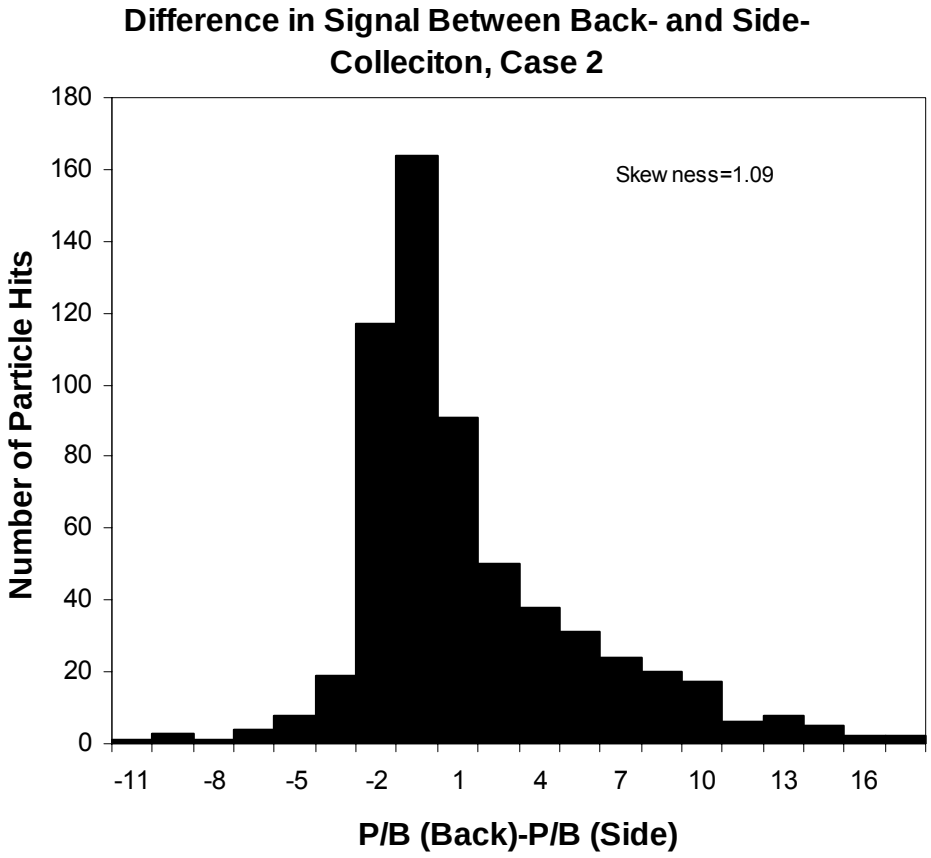


6.5(b)

**Figure 6.5.** (Continued)

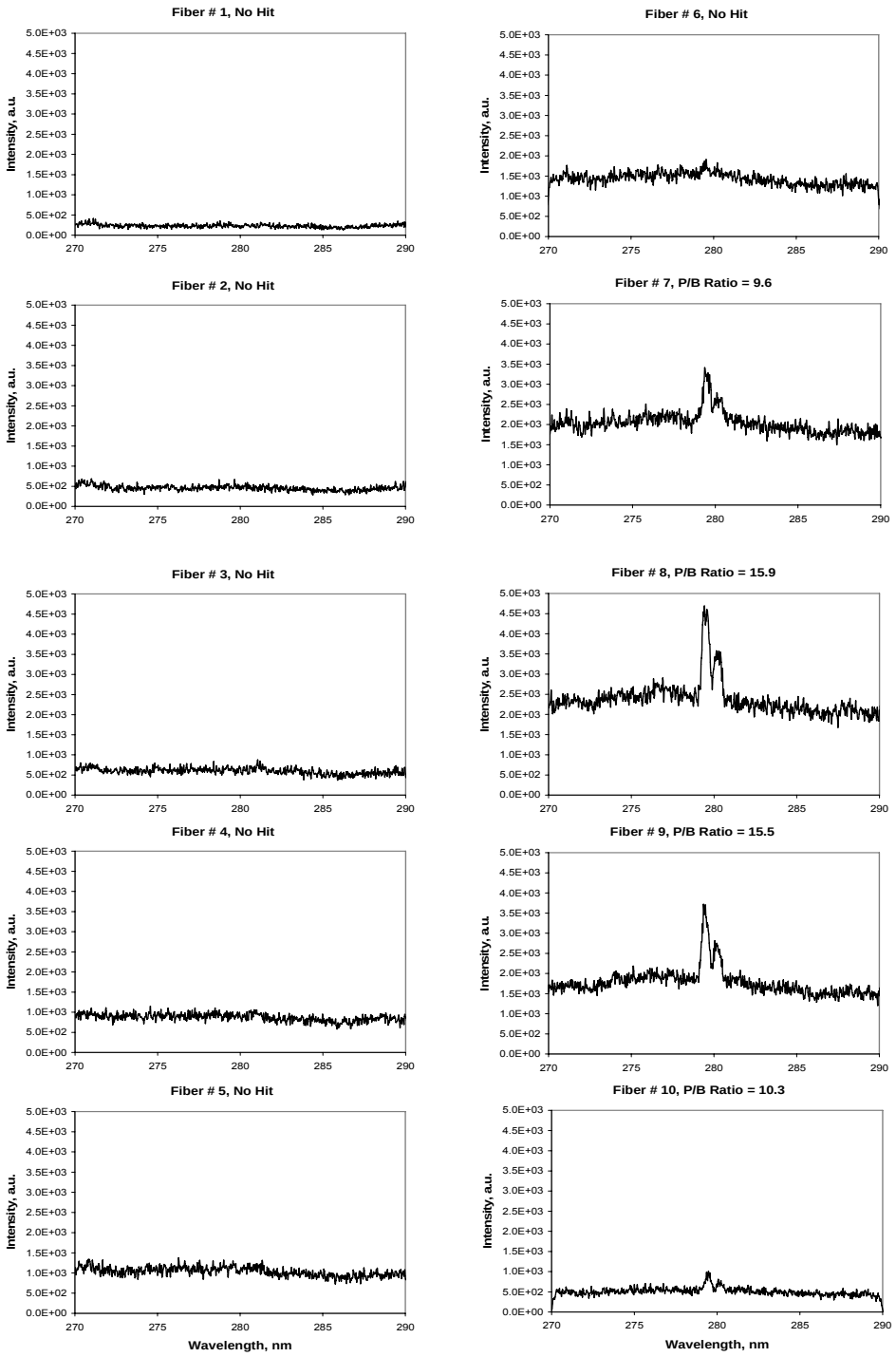


**Figure 6.6.** Ten spectra collected simultaneously at ten locations across the plasma image. Strong Mg peaks are visible in spectra 7,8,9, and 10. Mg peaks are not present in the remaining 6 spectra.

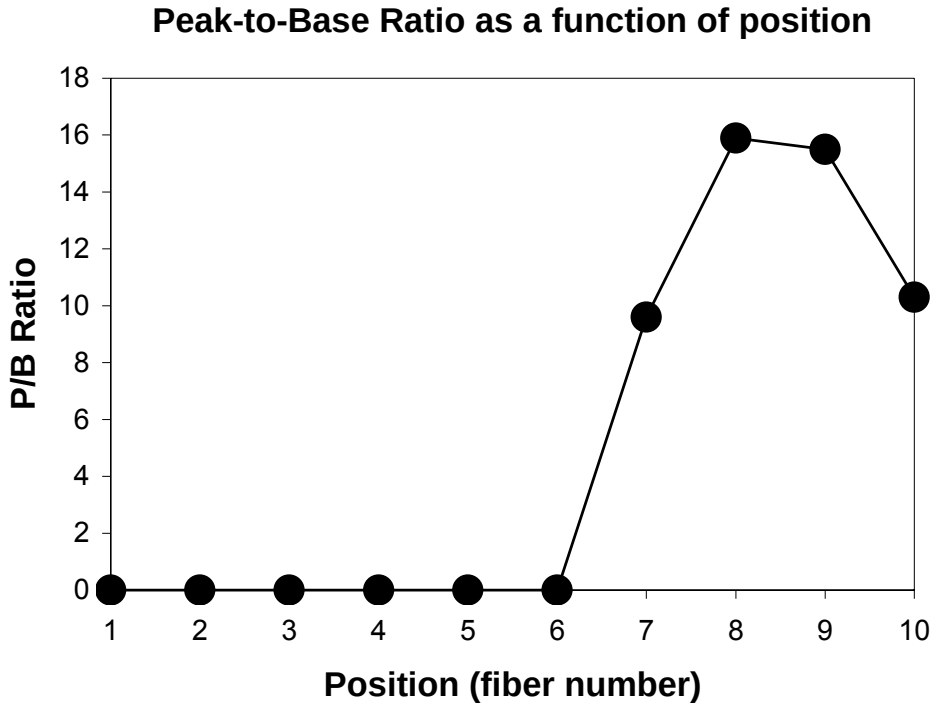


**Figure 6.7.** The LIBS signal from each of ten spectra plotted as a function of position. The signal shows strong variation across the plasma with a clear maximum.

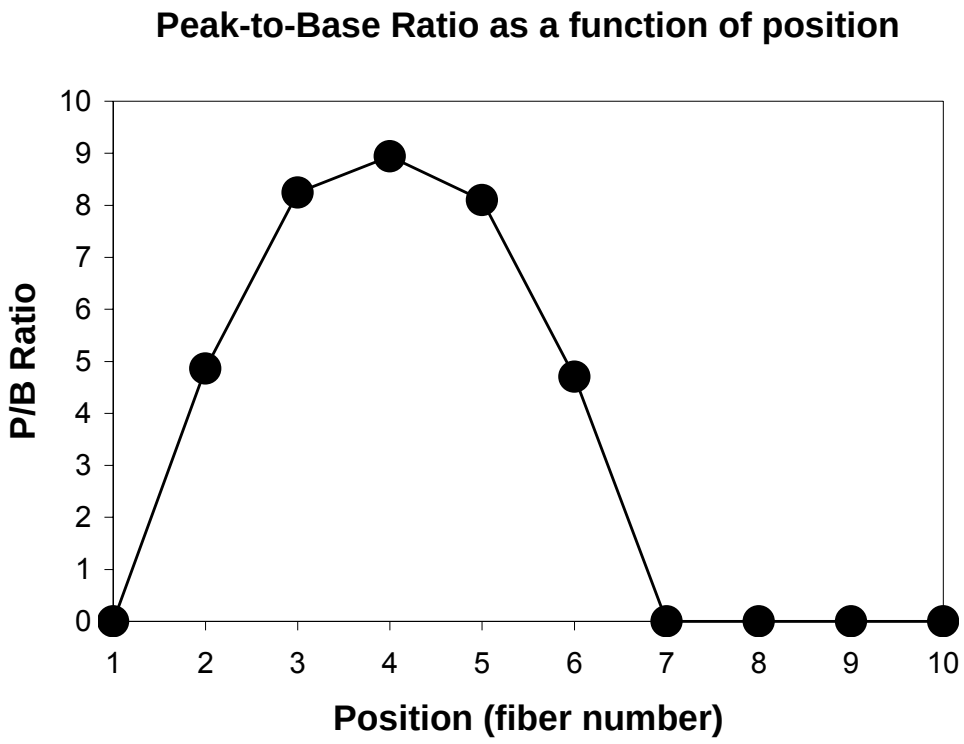


**Figure 6.8**. Signal variation for a second particle hit, located at a different position than Figure 6.7 within the plasma.

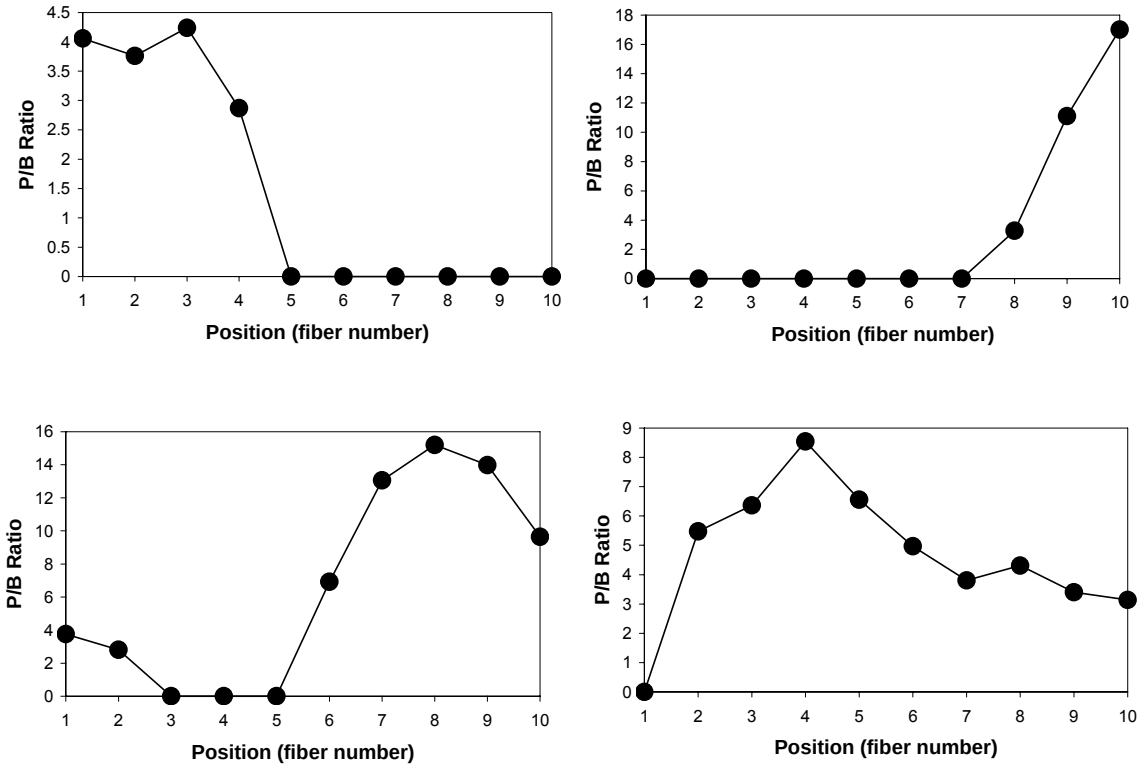


**Figure 6.9.** Several particle hits showing different distributions of peak-to-base ratio across the plasma volume.

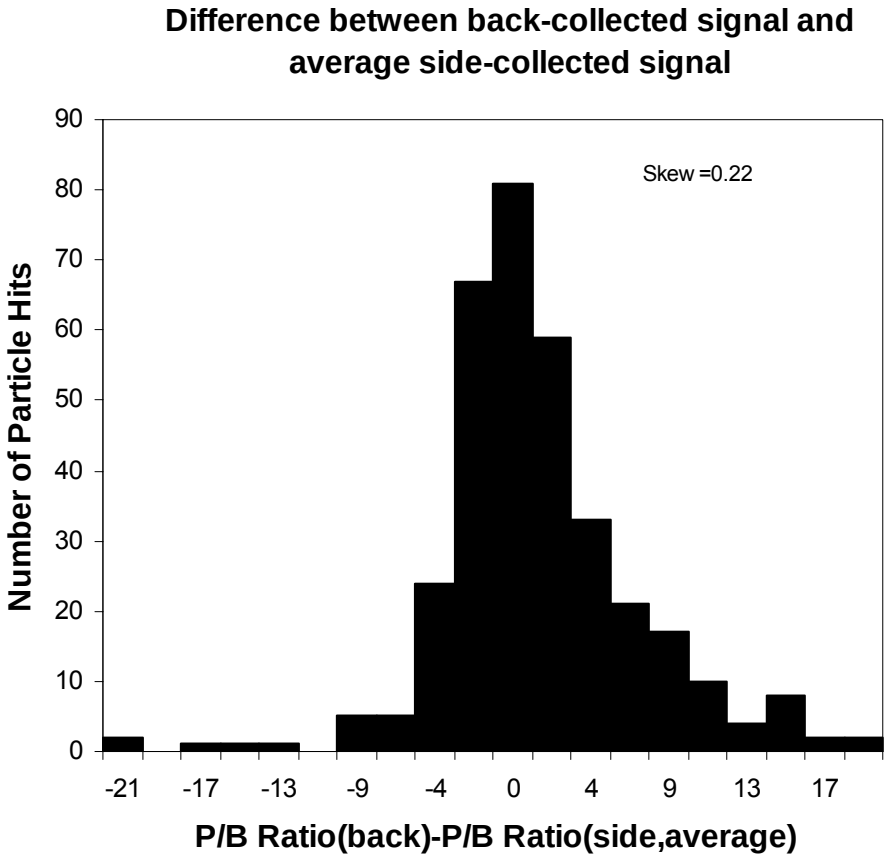


6.10(a)

**Figure 6.10.** The LIBS signal is again skewed towards the back-collection method when compared to the peak to base ratio of the integrated side-collected signal in Case 3 (a). However, when compared to the maximum of the spatially resolved signal, the signal is skewed towards the side-collected measurement (b).

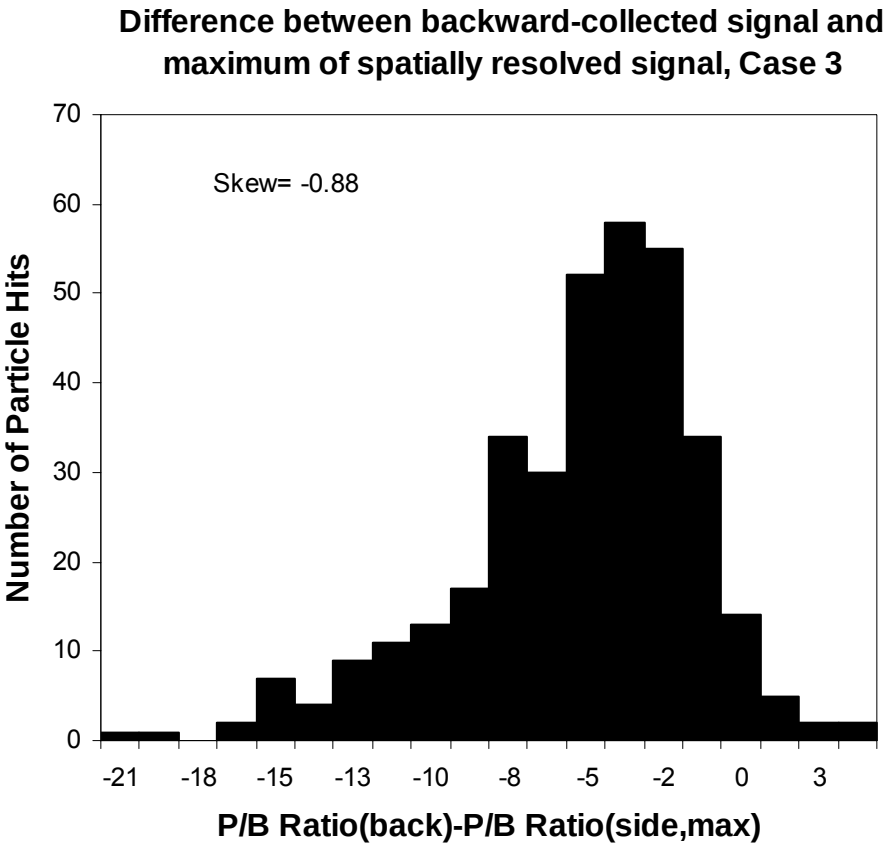


6.10(b)

**Figure 6.10.** (Continued)

**References**

1. S.G. Buckley, *et al.*, Laser-induced breakdown spectroscopy as a continuous emission monitor for toxic metals, *Waste Management*, vol. 20, p. 455, 2000.

2. J.E. Carranza *et al.*, On-line analysis of ambient air aerosols using laser-induced breakdown spectroscopy. *Spectrochimica Acta Part B*, vol. 56, p. 851, 2001.

3. G.A. Lithgow, A.L. Robinson, and S.G. Buckley, Ambient measurements of inorganic species in an urban environment using laser-induced breakdown spectroscopy, *Atmospheric Environment*, vol. 38, p. 3319, 2004.

4. J. Hybl, G.A. Lithgow, S.G. Buckley, Laser-induced breakdown spectroscopy detection of biological material, *Applied Spectroscopy*, vol. 57, no. 10, p. 1207, 2003.

5. S. Morel, *et al.*, Detection of bacteria by time-resolved laser induced breakdown spectroscopy, *Applied Optics*, vol. 42, no. 30, p. 6184, 2003.

6. A. Boyain-Goitia, D.C.S. Beddows, B.C. Griffiths, and H.H. Telle, Single-pollen analysis using laser-induced breakdown spectroscopy and Raman microscopy, *Applied Optics,* vol. 42, no. 30, p. 6119, 2003.

7. A.C. Samuels, F.C. DeLucia Jr., K.L. McNesby, and A.W. Miziolek, Laser-induced breakdown spectroscopy of bacterial spores, molds pollens, and protein: Initial studies of discrimination potential, *Applied Optics,* vol. 42, no. 30, p. 6205, 2003.

8. V. Hohreiter, J.E. Carranza, D.W. Hahn, Temporal analysis of laser-induced plasma properties as related to laser-induced breakdown spectroscopy, *Spectrochimica Acta Part B*, vol. 59, p. 327, 2004.

9. C.V. Bindhu, *et al.*, Laser propagation and energy absorption by an argon spark, *Journal of Applied Physics*, vol. 94, p. 7402, 2003.

10. C.V. Bindhu, *et al.*, Energy absorption and propagation in laser-created sparks, *Applied Spectroscopy*, vol. 58, p. 719, 2004.

11. J.E. Carranza, D.W. Hahn, Assessment of the upper particle size limit for quantitative analysis of aerosols using laser-induced breakdown spectroscopy, *Analytical Chemistry*, vol. 74, p. 5450, 2002.

12. V. Hohreiter, A.J. Ball, D.W. Hahn, Effects of aerosols and laser cavity seeding on spectral and temporal stability of laser-induced plasmas: applications to LIBS, *Journal of Analytic Atomic Spectrometry*, vol. 19, p. 1289, 2004.

13. V. Bulatov, L. Xu, I. Schechter, Spectroscopic imaging of laser-induced plasma, *Analytical Chemistry*, vol. 68, p. 2966, 1996.

14. V. Bulatov, R. Krasniker, I. Schechter, Study of matrix effects in laser plasma spectroscopy by combined multifiber spatial and temporal resolutions, *Analytical Chemistry*, vol. 70, p. 5302, 1998.

15. I.B. Gornushkin, *et al.*, Radiation dynamics of post-breakdown laser induced plasma, *Spectrochimica Acta Part B*, vol. 59, p. 401, 2004.

16. G.A. Lithgow, S.G. Buckley, Effects of focal volume and spatial inhomogeneity on uncertainty in single-aerosol laser-induced breakdown spectroscopy measurements, *Applied Physics Letters,* vol. 87, no. 1, art. no. 011501, 2005.

17. J.E. Carranza, D.W. Hahn, Plasma volume considerations for analysis of gaseous and aerosol samples using laser-induced breakdown spectroscopy, *Journal of Analytic Atomic Spectrometry*, vol. 17, p. 1534, 2002.

18. D.W. Hahn, W.L. Flower, K.R. Hencken, Discrete particle detection and metal emissions monitoring using laser-induced breakdown spectroscopy, *Applied Spectroscopy*, vol. 51, p. 1836, 1997.

19. D.W. Hahn, M.M. Lunden, Detection and analysis of aerosol particles by laser-induced breakdown spectroscopy, *Aerosol Science and Technology*, vol. 33, p. 30, 2000.

# 7. OPTICAL MODELS FOR IDENDIFICATION AND QUANITFICATION OF UNCERTAINTY DUE TO OPTICAL COLLECTION EFFICIENCY

In the preceding chapters, it was observed that when an aerosol particle is vaporized within a LIBS plasma, the material does not become distributed throughout the volume of the plasma, but remains localized. Furthermore, localized effects were found to be a significant source of uncertainty in the LIBS signal. These observations suggest that optimal performance of the technique cannot be achieved by merely reducing the variation in bulk plasma properties such as temperature and density. There are two potential components of the localized effects that may contribute to the uncertainty in the resulting signal. First, the vaporization of the particles and transport of the analyte depend on the time history of temperature, density, and motion of the plasma surrounding the particle. This determines the resulting amount of vaporized material within the plasma and the state of that material. Second, the optical system will not, in general, collect light with equal efficiency across the full extent of the plasma. Stated simply, the two questions are, 1) how much light is emitted from the particle material? and 2) what fraction of the emitted light is collected by the optics? This chapter will address the latter question in detail.

Initially, a simple, one-dimensional model of the optical system was used to estimate the fraction of light collected from a particle as a function of particle distance from the optical axis. Then, a detailed ray-tracing program was developed to model the

optical system more accurately and to characterize the collection efficiency throughout a three-dimensional focal volume. These models were verified by comparison with experimental results and used to quantify the performance the optical system.

### 7.1 One-Dimensional Optical Model

As a first step towards characterizing the behavior of the optical system, a one-dimensional model has been developed. The purpose of the model is to evaluate the relationship between off-axis location of a particle and the fraction of light collected into the optical fiber bundle. This model is compared with the experiment from the previous chapter. The model, illustrated in Figure 7.1, reduces the optical system to a single, ideal lens focusing light from the plasma onto the tip of a fiber bundle. In the model, the vaporized material in the plasma is distributed such that the image of the particle plume at the fiber tip is a circle of uniform fluence, F, and radius $R_p$. The fiber bundle is modeled as a single fiber of radius $R_f$. The particle image and fiber areas are denoted $A_p$ and $A_f$ respectively. The area of intersection of the image and fiber is denoted $A_i$. The model is axisymmetric, and the location of the particle is defined as the distance, $\rho$, of the center of the particle image from the optical axis (i.e. the center of the fiber). It is assumed that the dimensions of the plasma and fiber are small compared to the lens diameter and focal length, so that the solid angle subtended by the lens and the efficiency of the lens are independent of the particle location. The area of intersection of the image and the fiber tip, normalized by the maximum possible area, A (either $A_p$ or $A_f$, whichever is smaller), is defined as the area ratio, $\alpha = A_i/A$.

If the image is located such that the entire image is within the fiber tip, or the entire fiber tip is illuminated, $\rho \leq | R_f - R_p |$, then the maximum signal is collected, $\alpha = 1$.

If ρ is increased such that ρ > | $R_f$ - $R_p$ |, α decreases, approaching 0 at ρ = $R_f$ + $R_p$. The radius at which α begins to decrease is termed the critical radius, $\rho_{crit}$ = | $R_f$ - $R_p$ |. The maximum off-axis particle distance, $\rho_{max}$, is limited by the plasma dimensions. In this simple model, the result is that the signal, S, collected by the optical fiber is a function of only the fluence and the intersection area, S = FAα. The values corresponding to the experiment in Chapter 6, are $R_f$ = 0.35 mm, $R_p$= 0.75 mm. Using these values, α as a function of ρ was solved numerically, and the result is plotted in Figure 7.2.

As shown above, with fixed $R_f$, and $R_p$, S is a function only of ρ and F. By including realistic distributions of ρ and F, the results of a LIBS experiment may be simulated. With F held constant, a probability density function of α may by determined by entering a distribution of particle locations into the optical model. Since in practice particles are introduced randomly to the plasma, the probability density of the particle location is proportional to $\rho^2$. The resulting probability density function p(α), with particle locations restricted to the range $0 \leq \rho \leq \rho_{max}$, is plotted in Figure 7.3. In this model, all particles in the range ρ ≤ | $R_f$ - $R_p$ |, have the maximum area ratio, α = 1. These appear in the probability density as a delta function located at α = 1. The delta function is weighted by the total probability, P, that particles will have the maximum signal, given by

$$P(\alpha = 1) = \left( \frac{\left| R_f - R_p \right|}{\rho_{\max}} \right)^3 . \qquad (7.1)$$

The total probability of the rest of the distribution is P(α<1) = 1 - P(α=1). The behavior in the region where α < 1 is of interest, as it is where uncertainty is introduced into the LIBS signal. Since the probability of finding a particle increases with increasing ρ, while

$\alpha$ decreases with increasing $\rho$ above $\rho_{crit}$, the effect of variation of particle location is not a normally distributed signal. No matter how bright the original emission of the particles, there will always be a significant number of very small signals collected.

A distribution for values of F may be introduced to represent variations in particle size and bulk plasma properties. Recalling that size-selected particles were measured in the experiments in Chapter 6, it is reasonable to assume that the particle sizes approximately follow a normal distribution. Also, it is expected that variations in plasma properties would introduce a normally distributed error in the signal. Finally, it is assumed that the relative standard deviation is independent of the mean particle size. This means that the distribution of F may be characterized by a single parameter, the relative standard deviation $\hat{\sigma} = \sigma / F_0$, where $\hat{\sigma}$ is the relative standard deviation, $\sigma$ is the standard deviation and $F_0$ is the mean fluence.

To obtain the value of $\hat{\sigma}$, the data from the side-collected spectrometer in Case 3 in Chapter 6 is used. In that experiment, the plasma was imaged onto a large fiber bundle such that the entire plasma volume was captured within the fiber bundle. In terms of the model, the locations of the particles were restricted so that $\rho_{max} < \rho_{crit}$. The parameter $\hat{\sigma}$ was obtained by fitting a Gaussian to the data from the previous experiment. The data, reproduced from Figure 6.4d and the fitted Gaussian distribution are shown in Figure 7.4. Once the value of $\hat{\sigma} = 0.33$ is determined, a normalized Gaussian is convolved with the distribution shown in Figure 7.3. This convolution represents a full simulation of the back-collected LIBS data. The data from the back-collected optics from Figure 6.4c.are reproduced in Figure 7.5a, and the model results are shown in Figure 7.5b.

In comparing Figures 7.5 a and b, it can be seen that the general shape of the distribution in the experimental results is captured in the model. The mode near P/B Ratio = 9 from the experiment (Figure 7.5a) can be considered the contribution of the particles that are near the optical axis, and are entirely collected by the optics. The mode at 0 may be attributed to the particles that are located far from the axis. This result indicates that the localized nature of the emission from a vaporized particle will significantly affect the LIBS signal if care is not taken to properly collect light from the plasma. Since the errors introduced by these optical effects are not normally distributed, standard methods of error estimates are not applicable, and it is virtually impossible to properly interpret the LIBS signal for a single particle measurement. It is therefore imperative to fully understand and minimize the uncertainties associated with the optical effects.

### 7.2 Characterization of Three-Dimensional Optical Effects

The results of the simplistic model above confirm that optical effects can introduce a significant error in a LIBS measurement due to the off-axis location of particles. In a real LIBS system, there are additional optical effects that may also contribute to uncertainty in the measurements: the model assumed that light was collected into a single, large fiber, rather than a bundle of discrete, small fibers; the location of the particles along the axial dimension was neglected; realistic particle images were not used; and realistic focusing lenses were not incorporated. This raises the question whether additional optical affects may also play a role. In particular, in the above model, the distribution shown in Figure 7.4 was attributed to variation in F due only to particle size or plasma property variations. However, the detailed optical effects may contribute

uncertainty to the measurement, even if the particle image is located within the diameter of the fiber bundle. To address this question, an experiment was conducted to obtain three-dimensional location of the particles, along with simultaneous measurements of the LIBS signal and images of the material plumes from the vaporized particles. Additionally, a detailed ray-tracing model was developed to characterize the actual optical system used in the LIBS device. The experimental results are used to validate the ray-tracing model, and the model is used to quantify the detailed optical effects on the LIBS signal.

**7.3 Experiment**

An experiment was conducted to simultaneously measure the location of individual vaporized particles and the resulting signals measured by the LIBS device. The experimental setup is a modification of that described in Chapter 6. The setup is shown in Figure 7.6, and uses the same laser, spectrometers, and collection optics as described previously. Spectra were collected simultaneously with two spectrometers from the backward-direction and the side-direction. The ten-fiber array (as in Case 3) was used for the side-collection optics. The side-collected spectra were used only for determining the axial location of the particles within the plasma. For the spectrometer measuring the back-collected signal in these experiments, a 19-fiber bundle was used rather than the 7-fiber bundle used previously. Each individual fiber had a core diameter of 200 μm, and an outer diameter of 250 μm. This type of fiber bundle is commonly used in LIBS systems, and it is expected to collect light more uniformly across a larger volume than a 7-fiber bundle. The back-collection optical setup used in this experiment is the

most common arrangement for LIBS aerosol measurements. The back-collected signal will henceforth be referred to as simply the LIBS signal.

In addition to the spectrometers, an ICCD camera was located in the forward-direction along the laser axis. The residual laser light, transmitted through the plasma, was diverted with a dichroic mirror. A single 75 mm focal length, fused silica lens focused light from the plasma with a magnification factor of approximately 2. The plasma emission was filtered with a narrow bandpass interference filter (3 nm FWHM, 396.2 nm center wavelength) and imaged onto the chip of the ICCD camera. An iris restricted the aperture of the focusing lens such that the depth of field of the ICCD camera was approximately equal to the length of the plasma. The two spectrometers and the ICCD were synchronized with a delay generator. A delay of 5 μs with respect to the laser pulse, and integration time of 0.5 μs was used to so that relatively bright and sharp images could be obtained with the ICCD camera. With these images, the size, shape and intensity distribution of the analyte emission can be measured, along with the location of the particles in the plane normal to the optical axis.

A different aerosol generation system was used than in the previous experiment described in Chapter 6. It was necessary to have strong particle emission in order to obtain useful images with the filter and ICCD. To obtain bright particle emission, borosilicate glass microspheres were used (Duke Scientific, No. 9002). According to the manufacturer, the spheres had a mean diameter of 2.0 ± 0.7 μm, and contained **% calcium by weight. The calcium contained in the particles is the analyte for the experiments. The spectral signal is defined as the integrated intensity of the Ca II emission line at 396.8 nm. Independent tests of the particle properties were not

performed. The spheres were suspended in HPLC grade purified water. The suspension was then nebulized using a medical nebulizer (Hudsen, No. 1724). The aerosol flow was diluted with HEPA filtered air and introduced to the LIBS plasma as a free jet into the laboratory air. The flow was diluted such that particle emissions were seen in approximately 1% of the LIBS spectra.

The back-collected spectrum, ten side-collected spectra along with signal as a function of z-position along the optical axis, and a raw particle image, all from the same single laser-shot, are shown in Figure 7.7 a-d. Note that the raw particle images contain light from the background gas in the plasma along with emission from the particle material. To remove the background light, an average image of 100 laser shots was taken in pure air, and subtracted from the raw particle images. The average background image, and the particle image of Figure 7.7 with the background subtracted are shown in Figure 7.8 a and b.

The integrated intensity of the background-subtracted particle image represents the emission from the particle. With a proper optical system, the integrated particle emission would be exactly correlated with the LIBS signal measured with the spectrometer. As observed in the previous chapters, this is not the case. The integrated image intensity versus the LIBS signal is plotted in Figure 7.9. This figure is similar to Figure 5.2. Each point is a single laser shot with the horizontal axis representing the true particle emission, as measured by the integrated particle image, and the vertical axis representing the LIBS signal measured by the back-collected spectrometer. There is a poor correlation between the two ($R^2 = 0.40$) even using the large fiber bundle. Unlike in Figure 5.2, the data are bounded above by a straight line. The upper bound can be

interpreted as representing the ideal correlation between the signals. The points along this line are particles where the maximum fraction of light was collected by the optics. For all the other points, a smaller fraction of light was collected, thus the LIBS signal was reduced and the point falls below the ideal correlation. This figure illustrates the need to fully understand, and eliminate, these errors caused by inefficient optical design.

### 7.4 Ray-Tracing Model

A ray-tracing model was developed to characterize the detailed performance of the real optical system in the LIBS instrument. In a ray-tracing model, a grid of light rays are emitted from an object. The trajectory of each ray is calculated as it passes through optical surfaces, until the ray reaches the image location. When a ray intersects an interfacial surface between dissimilar materials, Snell's law may be used to calculate the angle of refraction, and Fresnel's equation may be used to calculate the percentages of light transmitted and reflected. Once the rays reach an image surface, the number and intensity of rays at a given location in the image plane determine the intensity of the image at that point.

In this case, the objective is to take particle emission images collected experimentally and use the ray-tracing model to determine what fraction of the light from the particle is collected into the fiber bundle. Instead of running the entire ray-tracing model for each particle image, the model was run once, in the reverse direction, using the fiber bundle tip as the object. Rays from the fibers were traced backwards through the optics, and the focal volume efficiency was mapped out in a three dimensional volume around the plasma location. In the model, the horizontal axis in the image plane is the x-direction, the vertical axis is the y-direction, and the optical axis is the z-direction. The

focal point of the collection optics is located at ($x_0$, $y_0$, $z_0$) = (0, 0, 0). To map the focal volume efficiency, square images, approximately 3mm per side were generated at intervals of 0.275 mm (twice the resolution of the side-collection fiber array). An image of the focal volume efficiency map, located at the focal plane, $z_0$, is shown in Figure 7.10. In this image, the color scale indicates the efficiency with which the collection optics collect light from a given location. In the image, the individual focal volumes of each fiber in the bundle are clearly visible. A larger fraction of light will be collected from a point of higher efficiency, at the center of one of the fiber focal volumes for example. Once the focal volume was mapped, particle images could simply be multiplied by the efficiency map to determine what fraction of light would reach the fiber tip. This method significantly reduces computational time compared to running the ray-tracing model separately for each particle image.

### 7.5 Validation of Ray-Tracing Model

To validate the ray-tracing model, the results of the model were compared with the experimental data. To simulate a LIBS signal with the model, a particle image from the ICCD camera was input into the model, and the amount of light collected by the optical fiber was calculated. To calculate the simulated LIBS signal, the following procedure was followed:

1) The plasma background image was subtracted from the raw particle images.
2) The z-position of each particle was calculated as the weighted average of the ten side-collected spectra. For each particle, a focal volume efficiency map from the ray-tracing model was selected corresponding to the z-position of the particle.

3) The particle image was multiplied by the efficiency map, and the result was integrated. The resulting value is the simulated signal.

A particle image, focal volume efficiency map, and the product of the two are shown in Figures 7.11 a-c. The calculated model signal is plotted vs. the measured LIBS signal in Figure 7.12. With an $R^2$ value of 0.96, there is a very strong correlation between the two. The small error between the two is likely due to three factors. First, the plasma background changes with each laser shot so there is some error associated with subtracting the averaged background image. Second, the particle images are two-dimensional projections of a three dimensional vapor plume, and the two dimensional image is multiplied by a two-dimensional efficiency map. This neglects the distribution of the particle along the z-direction. This error is exacerbated near the ends of the plasma, where the particle plume extends beyond the end of the ten fiber array used to calculate z-position. When only particles with a z-location within the middle 80% of the plasma are used, the correlation coefficient increases to 0.98. This suggests that the errors are introduced in the inputs to the ray-tracing model, and gives confidence that the ray-tracing model itself is highly accurate.

**7.6 Investigation of Optical Performance Using Ray-Tracing Model**

Once validated, the ray-tracing model was used to simulate LIBS experiments and investigate the performance of the optical system in detail. In the one-dimensional model above, it was assumed that any particle image located within the fiber bundle tip would be collected with maximum efficiency. However, a real fiber bundle contains inactive area between the cores of the individual fibers. Also, the collection efficiency will be reduced if the particle is out of focus in the axial direction. Each of these effects were

simulated using the ray-tracing model. Additionally, the effect of defocusing the collection optics to blur the individual focal volumes of each fiber was investigated. Finally, the potential of improving the performance by controlling the location of the particle using a laser-triggering was studied.

*7.6.1 Detailed Effects of Particle Location*

In the experiment, even though the particles were monodisperse, the total integrated emission from each particle varied greatly. Therefore, to isolate the effects of particle location, simulations were run using several of the experimental images. The image in Figure 7.8b represents a large particle plume, and an image with a small plume is shown in Figure 7.13. Each particle plume is roughly circular and they have diameters of approximately 1 mm and 0.25 mm respectively. Random locations throughout a volume representing the plasma volume were selected, and the images were multiplied by the focal volume efficiency map at those locations. The signal was normalized by the maximum value, achieved when the particle is located in the focal point ($x_0$,$y_0$,$z_0$). The results are shown in Figure 7.14a and b for the small and large particle respectively. For the small particle in Figure 7.14a, the size of the plume was approximately equal to the inter-fiber spacing. This resulted in a significant variation in signal even for particles located entirely within the fiber bundle tip, and a distinct bi-modal distribution can be seen. This demonstrates that the fiber bundle does not collect light as efficiently as a single fiber, and a bi-modal distribution may be generated by optical effects alone, without any variation in true particle emission. However, with the larger particle plume, this effect is diminished because the plume is sufficiently large that signal is collected by

several fibers. This demonstrates that uncertainty can arise not only from particles that fall on the edge of the fiber bundle, but also in between the individual fibers of the bundle.

*7.6.2 Effect of Defocusing the Collection Optics*

Both sources of uncertainty, due to off-axis or inter-fiber location, may be reduced if the focal volume of the collection optics can be made larger and more uniform. This may be accomplished by defocusing the collection optics. By defocusing the optics, the individual fiber focal volumes are blurred together, and the entire bundle collection area is increased. This comes at the expense of reduced collection efficiency, and therefore reduced signal. To quantify these effects, simulations similar to those in the preceding section were run, but with the plasma volume located approximately 5 mm from the focal point of the optics. The efficiency map at the axial location z = -5 mm is shown in Figure 7.15. In this case the focal volume is larger and more uniform than that shown in Figure 7.10, however the peak efficiency is also approximately 25% of that near the focal point. Histograms of the signals from the two particles, using the defocused optics, are shown in Figures 7.16a and b. Both show a dramatically improved shape, following nearly a normal distribution, each with relative a standard deviations of 32%. Therefore a significant improvement in the precision of the technique can be achieved with the simple step of defocusing the collection optics. However, the mean values of each distribution are each less than 20% of the maximum signal, meaning that the improved precision comes at the expense of significantly limited sensitivity.

*7.6.3 Reduction of Uncertainty with Particle Triggering Sytem*

As shown above, improvement in signal precision may be achieved by defocusing the collection optics, however, it is desirable to achieve both improved precision and

sensitivity. One proposed method to achieve this is through the use of a triggering system so that the laser fires when a particle is at a specified location. If the position of the particle could be controlled, it would clearly improve the performance of the LIBS device. However, it is unclear exactly how precise the triggering system would need to be. This question was address by again running a simulation, this time with the plasma located at the focal point of the optics, and the particle location restricted to a specified sampling region. The size of the sampling region was restricted in both the axial and radial directions. In this case, only the small particle image was used because of the larger uncertainty associated with the inter-fiber spacing.

Simulations were run with the radial location restricted to values of $\rho_{max}$ from 0.6 mm (the approximate diameter of the fiber bundle) down to 0.1 mm. The signal distribution with $\rho_{max}$ = 0.6 mm is shown in Figure 7.17. As expected, the large number of small signals, due to the particles located at the edge of the bundle, is reduced, and the distribution shows a single mode. As the tolerance on radial location is reduced, the uncertainty is also reduced, and mean signal is increased. The uncertainty can be further reduced by restricting the axial location as well as the radial location. Simulations were run for values of $\rho_{max}$ between 0.1 mm and 0.6 mm and with the axial location restricted to ± 0.5 mm of the focal point ($|z - z_0| \leqslant 0.5\text{mm}$). The mean signals and the relative standard deviations for each case are plotted in Figure 7.18. The blue curves correspond to the case where the axial position is not controlled, and the red curves correspond the case in which both the axial and radial location are controlled. It can be seen that if particle location can be controlled, not only is the uncertainty be reduced, but the signal is also maximized. These results serve as a guide for designing a laser-triggering system.

If the tolerance for the radial position can merely be held within 0.6 mm, the relative standard deviation will be better than that achieved by defocusing the optics, and the sensitivity will be improved such that the mean signal is 65% of the maximum. However, if a tolerance of ± 0.1 mm in the radial direction and ± 0.5 mm in the axial direction were achieved, the uncertainty would be almost completely eliminated and the maximum sensitivity obtained.

**7.7 Conclusions**

By modeling the optics of the LIBS device, the performance of the optical system used to collect plasma emissions can be understood in detail. This investigation has identified and quantified the sources of uncertainty due to the optical design of LIBS devices. Significant uncertainty is introduced into the LIBS signal when the optics only collect light from the center of the plasma and particles located near the edge of the plasma fall only partially within the focal volume of the optics. Furthermore, this effect does not introduce a normally distributed error, making quantification of the uncertainty in the resulting LIBS signal difficult. It was found that defocusing the collection optics is one method that can be used to improve the precision of the technique, and eliminate the edge-effect errors. However, this comes at a significant cost to the sensitivity of the technique. Finally, it was found that if the location of particles can be restricted with the use of a laser-triggering system, the uncertainty due to the optics can be virtually eliminated, while the sensitivity is also maximized. The results provide design criteria for the tolerances in particle location required to achieve a given performance of the device. Finally, with a detailed understanding of the optical effects, the remaining question of the role of particle vaporization and transport may be clearly addressed.

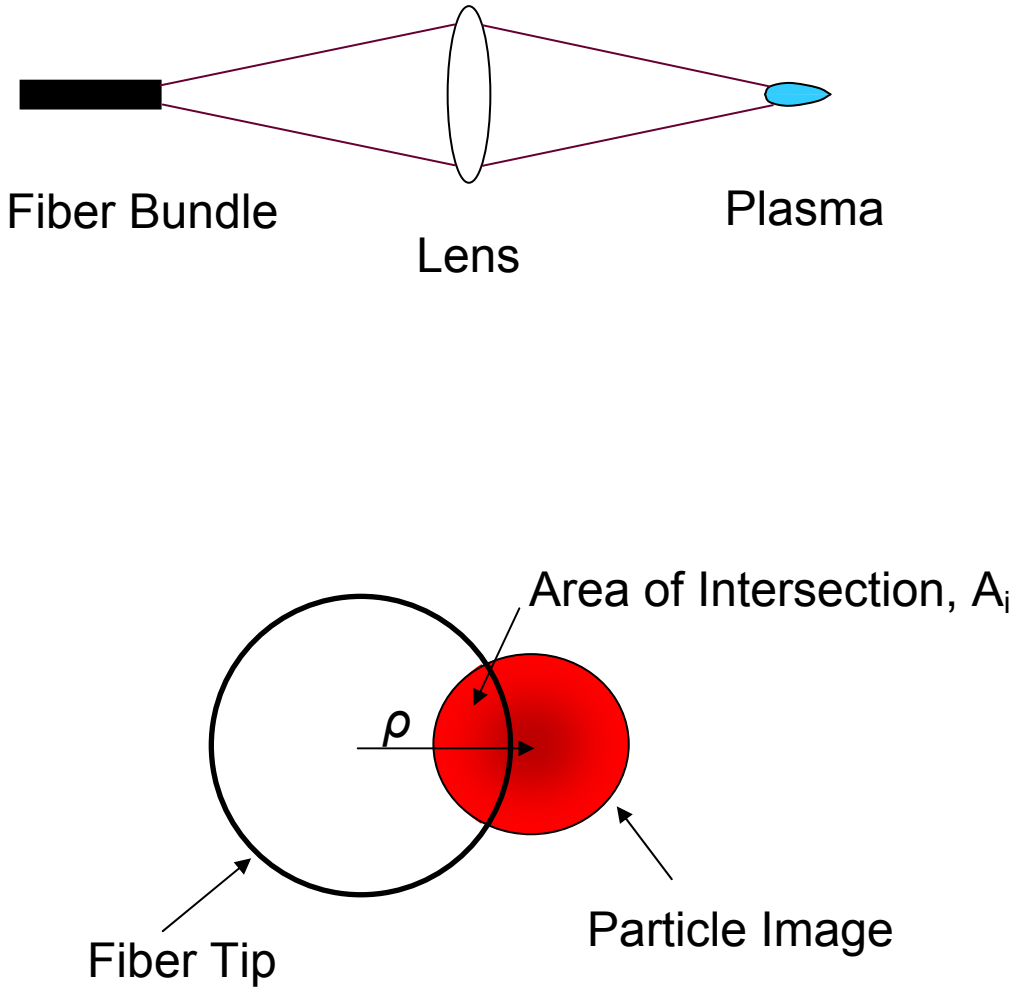


**Figure 7.1.** Schematic diagram of the one-dimensional optical model. A single, ideal lens focuses light from the plasma onto the tip of an optical fiber bundle. The area of intersection, $A_i$, of the particle image and the fiber tip is a function of the radial location, ρ, of the particle image.

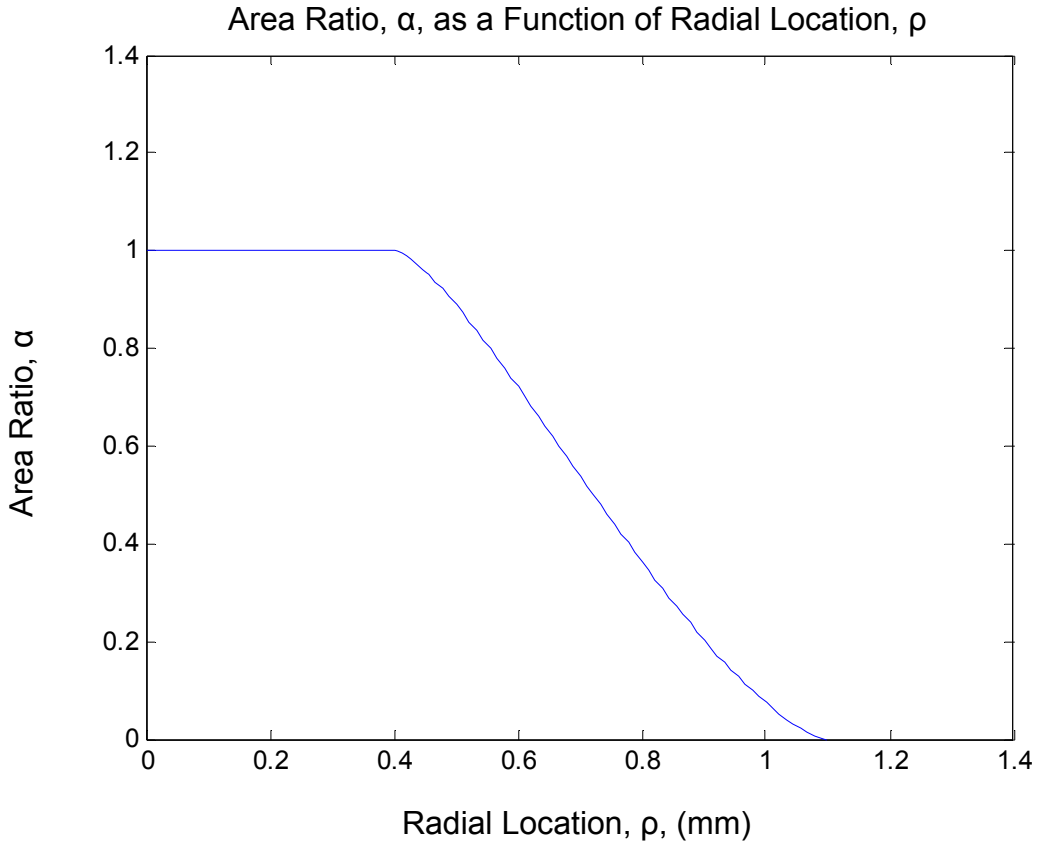


**Figure 7.2.** The area ratio α as a function of radial location ρ, has a constant, maximum value of 1 for $\rho < \rho_{crit}$, and then decreases to 0.

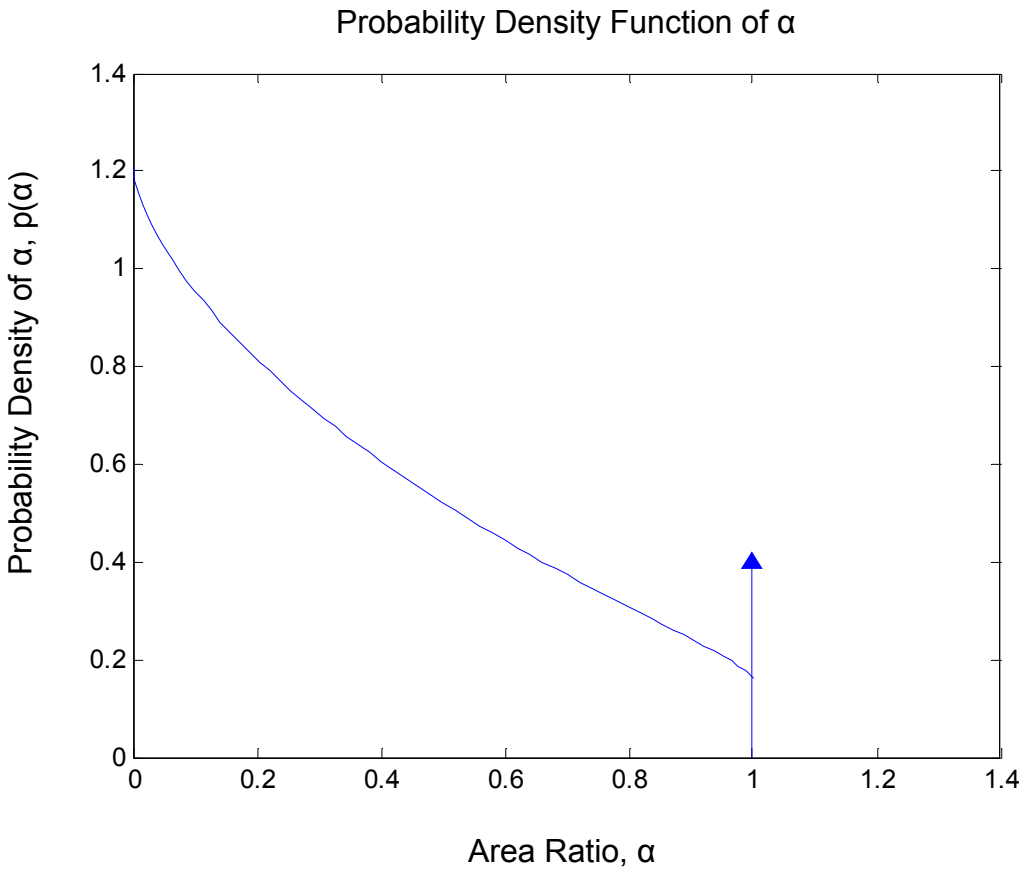


**Figure 7.3.** The probability density function of α. The interval $0 < \alpha < 1$ represents the signals from particles with location $\rho > \rho_{crit}$, whose image is partially collected by the optical fiber. The particle images with $\rho \leq \rho_{crit}$ are represented by a delta function at $\alpha = 1$.

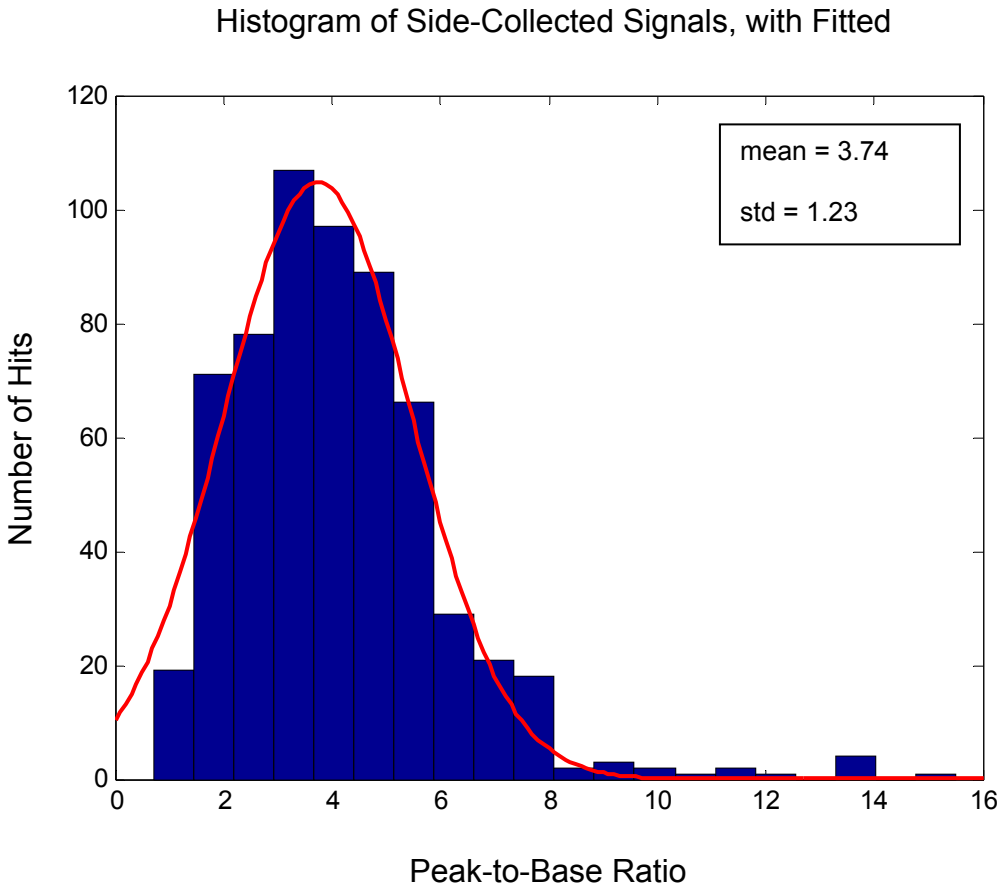


**Figure 7.4.** A Gaussian distribution is fit to the data from Case 3 in Chapter 6, to determine the relative standard deviation, $\hat{\sigma} = 0.33$, of the signal for particle images located entirely within the fiber bundle tip.

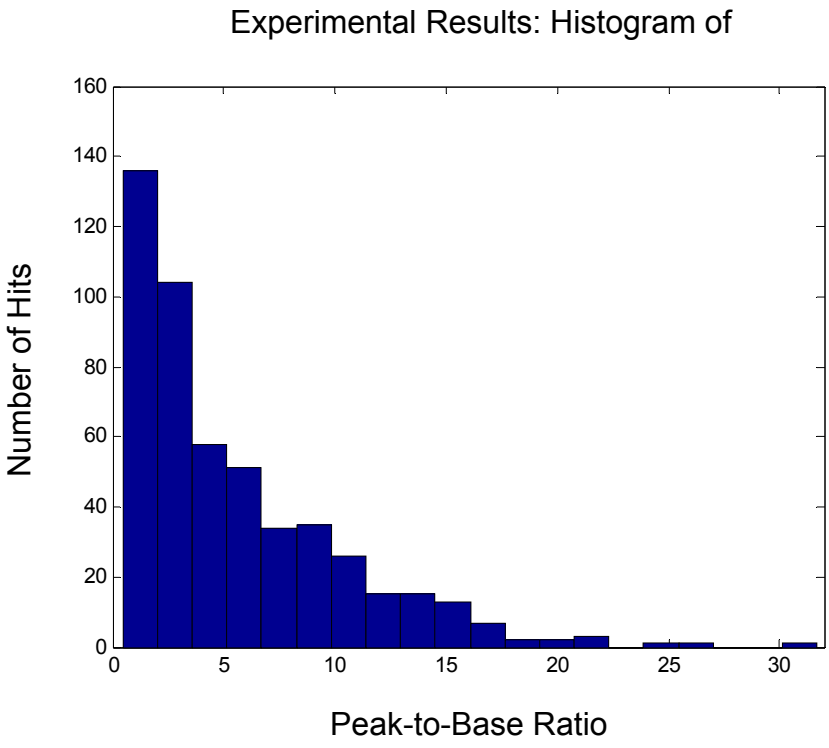


(a)

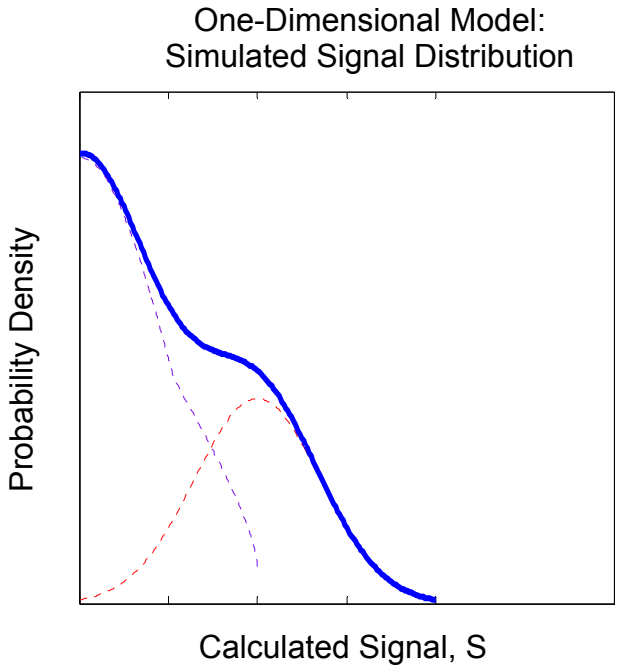


(b)

**Figure 7.5.** The shape of back-collected signal from Case 3 in Chapter 6 (a) captured by the one-dimensional optical model (b).

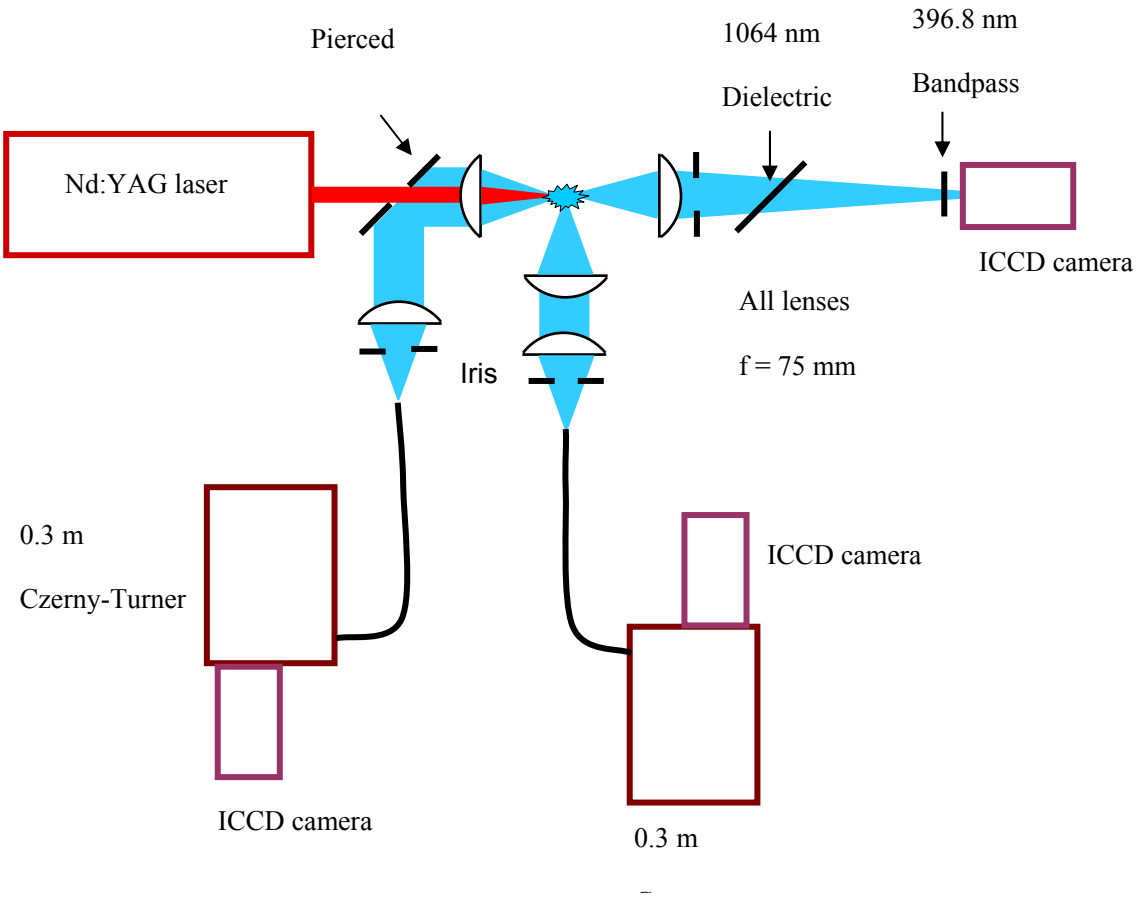


**Figure 7.6.** Schematic of the experimental apparatus.

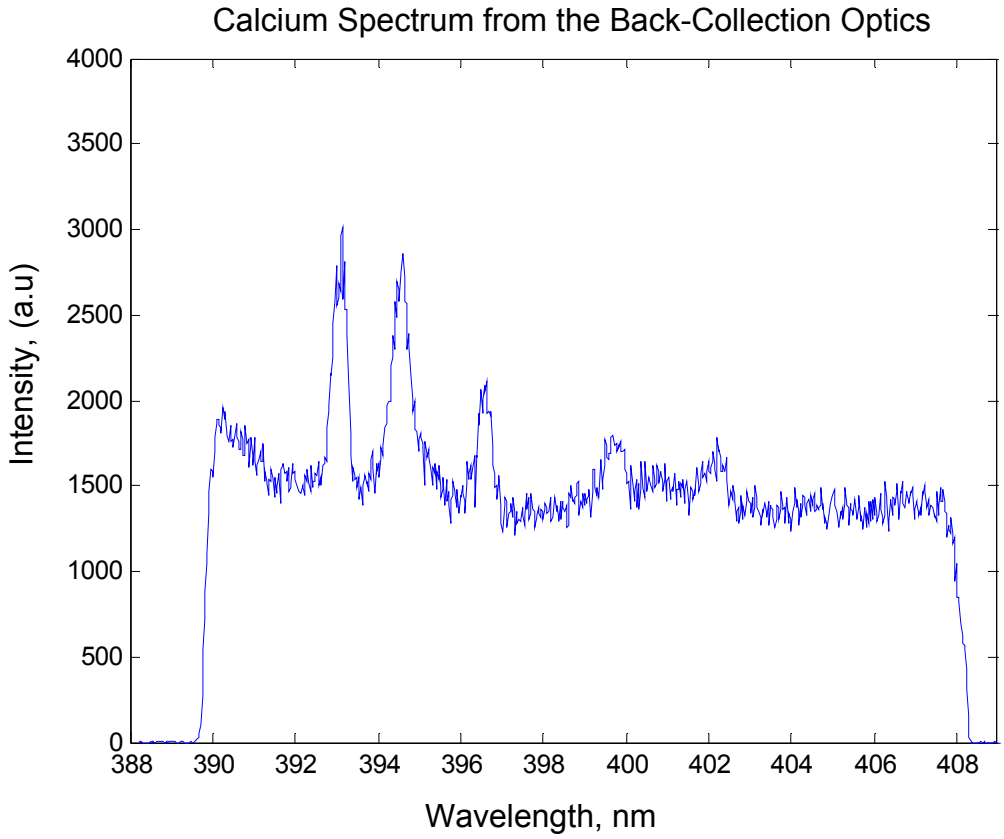


7.7(a)

**Figure 7.7.** In the experiment, the LIBS signal is the back-collected spectrum (a). The axial location is determined from the ten spectra from the side-collection fiber array (b). A raw image of the plasma emission is collected with the ICCD (c). All are collected simultaneously.

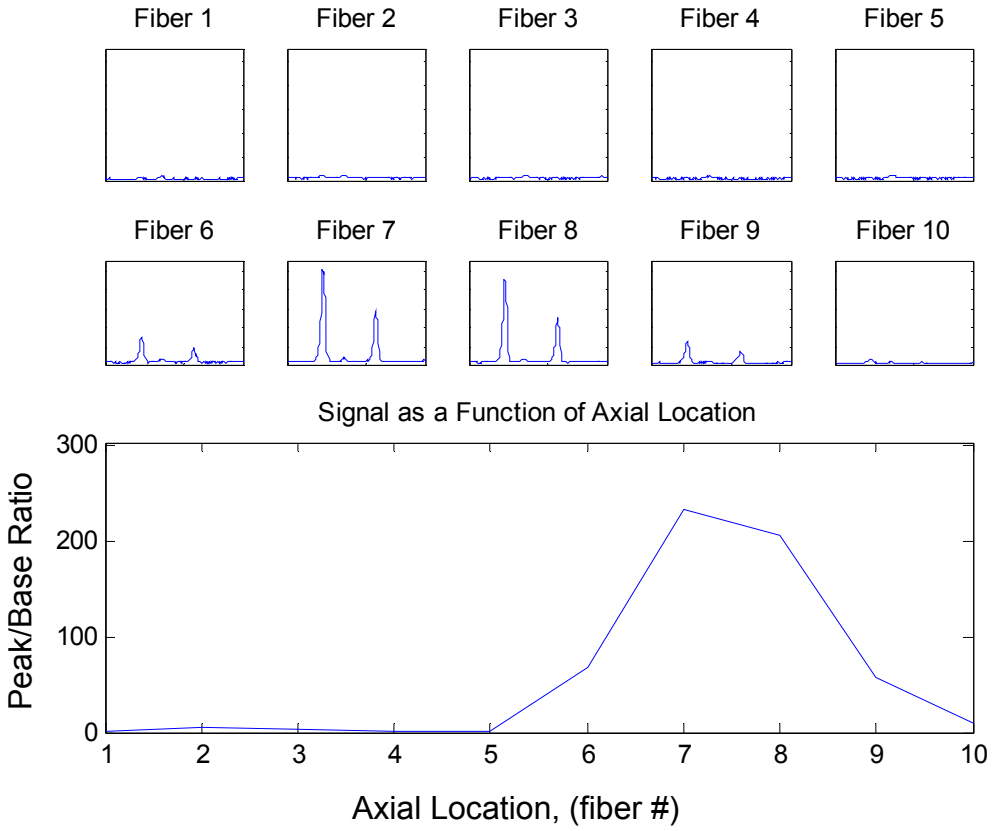


7.7(b)

**Figure 7.7.** (Continued)

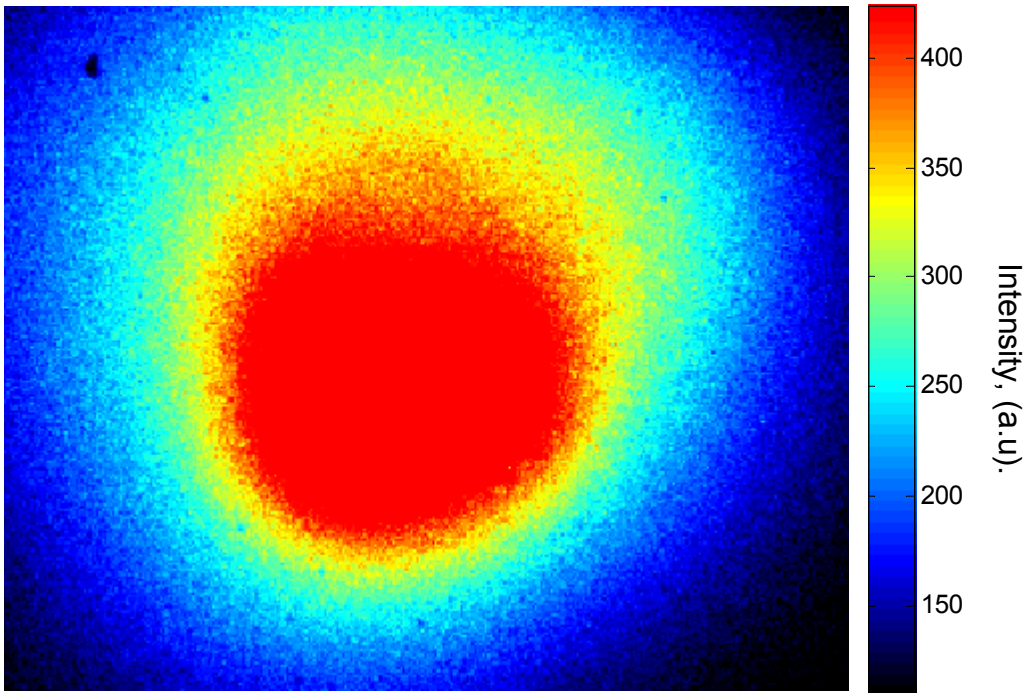


7.7(c)

**Figure 7.7.** (Continued)

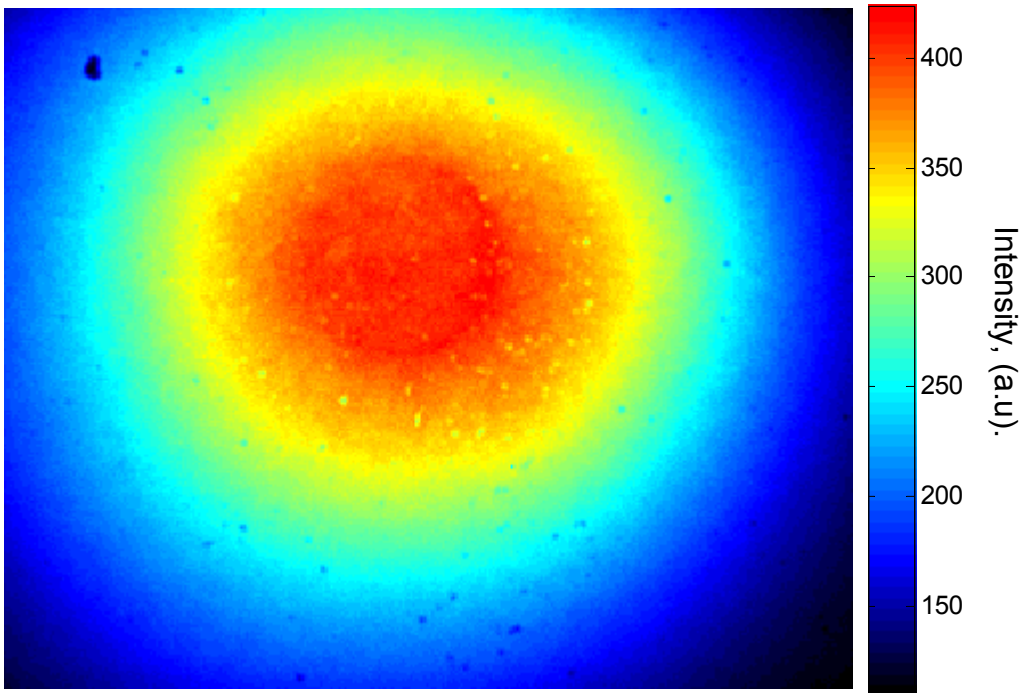


7.8a

**Figure 7.8.** A background images was acquired by averaging 100 plasma images taken in pure air (a). The background image is subtracted from the raw ICCD image of a plasma containing a particle (Figure 7.7c) to give an image of only the particle plume (b). The color-bar is rescaled for each image.

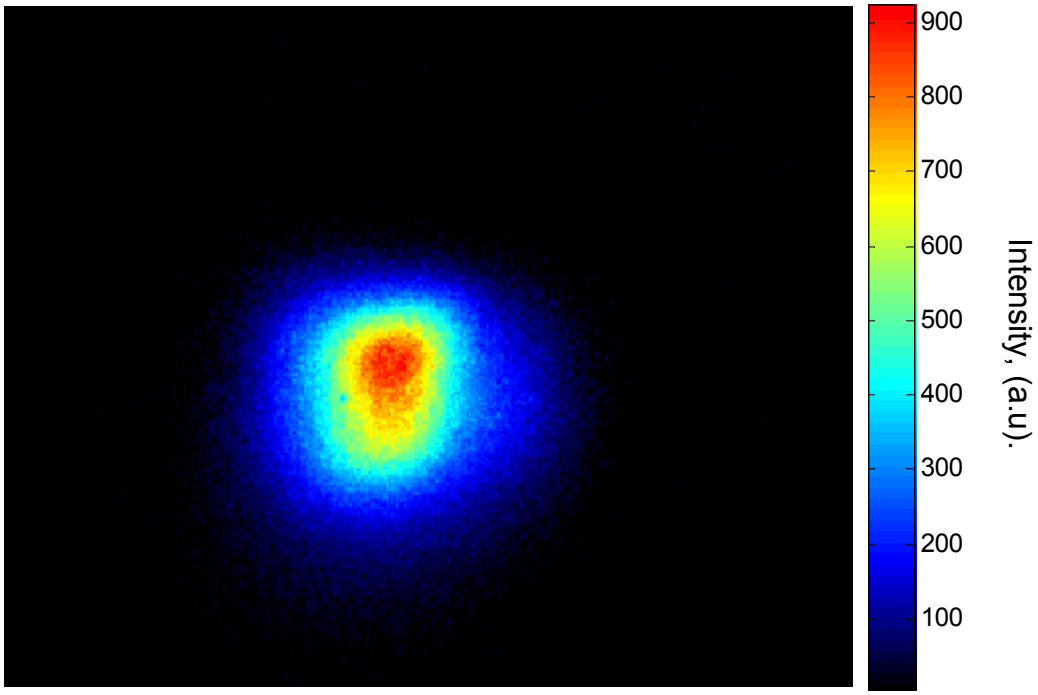


7.8b

**Figure 7.8.** (Continued)

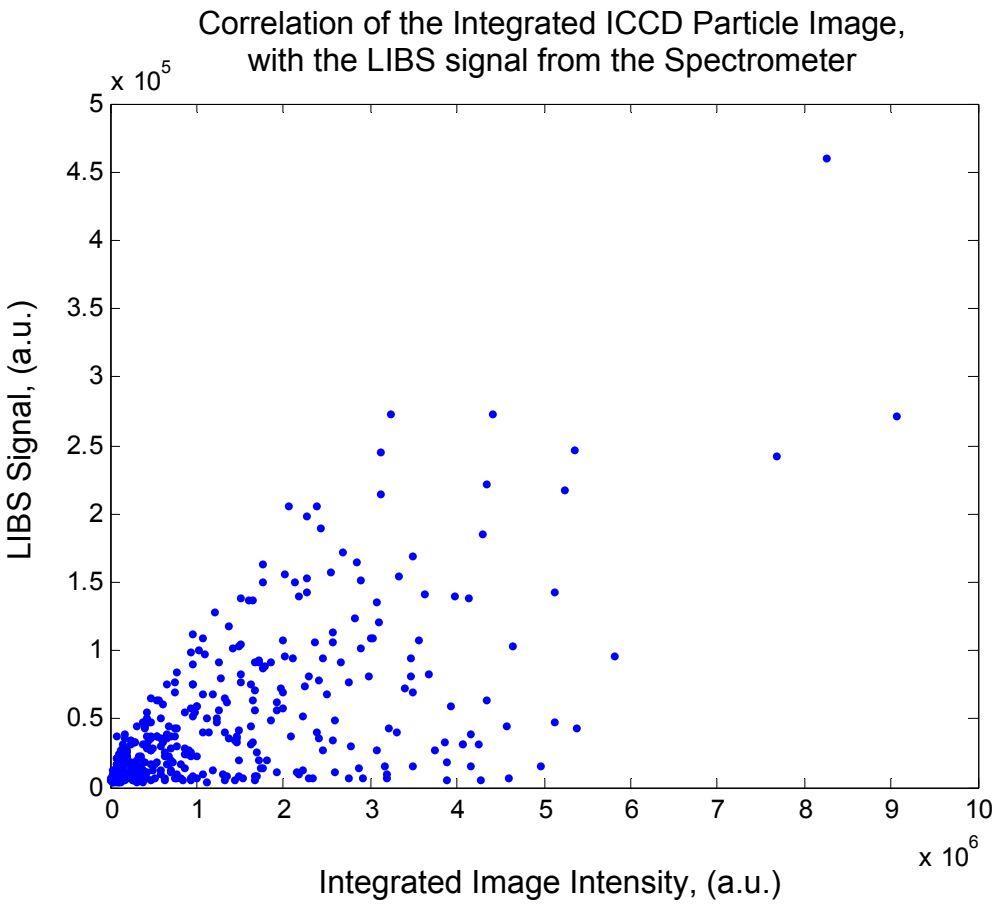


**Figure 7.9.** The integrated image intensity and the collected LIBS signal show poor correlation.

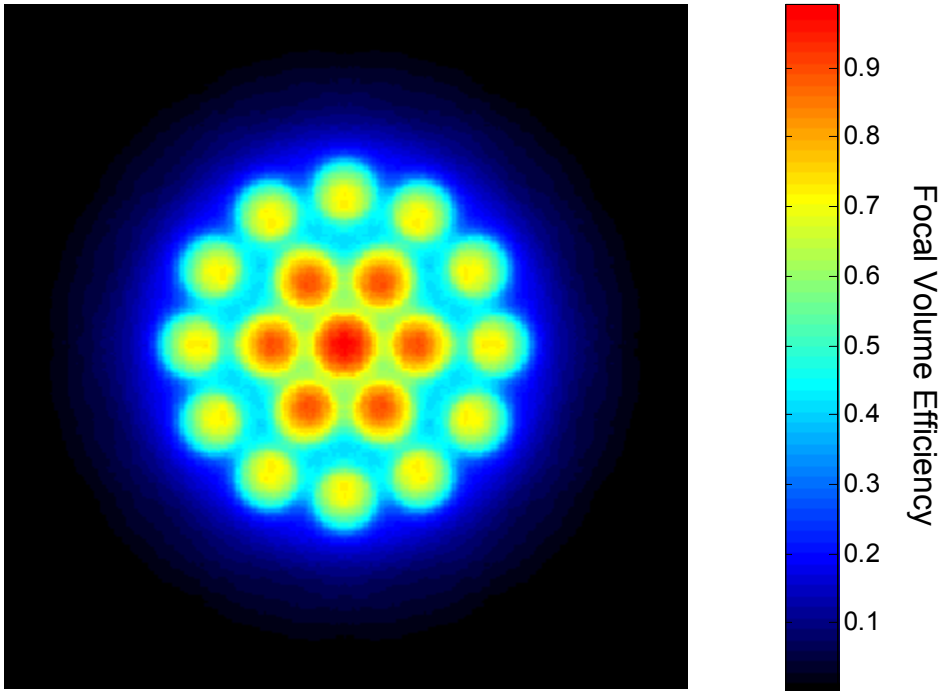


**Figure 7.10.** The focal volume efficiency map located at the focal plane. The focal volume of each of the 19 individual fibers in the bundle are visible.

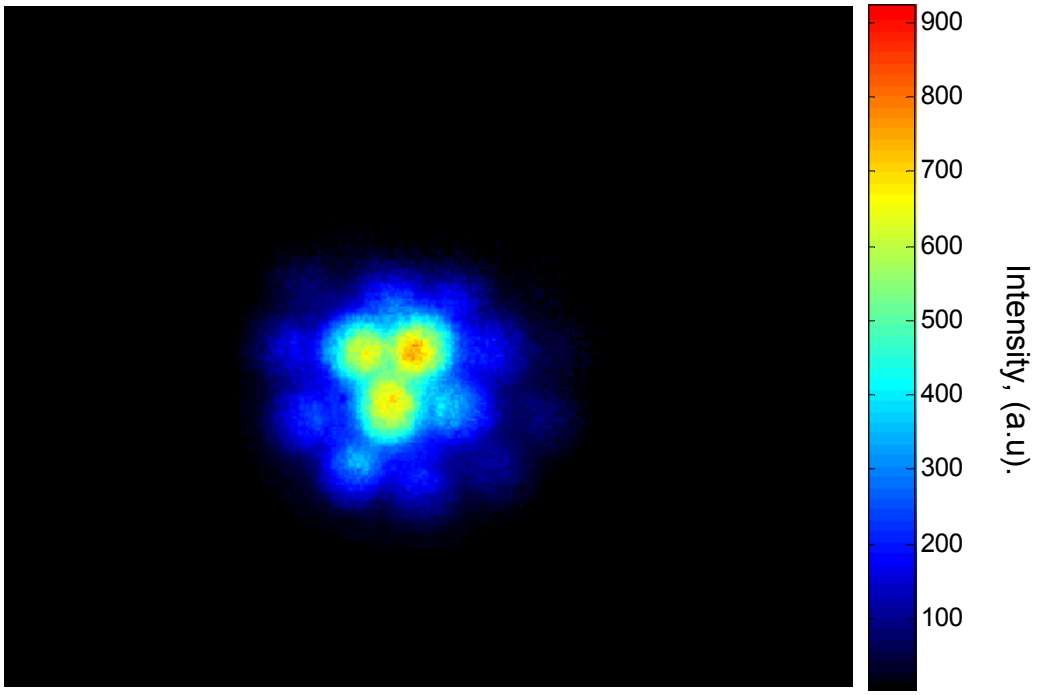


**Figure 7.11.** The product of the particle image (7.8b) and the focal volume efficiency map (7.10). The color scale is the same as in Figure 7.8b. Only the portion of the particle plume located within the focal volume of an individual fiber is collected with high efficiency.

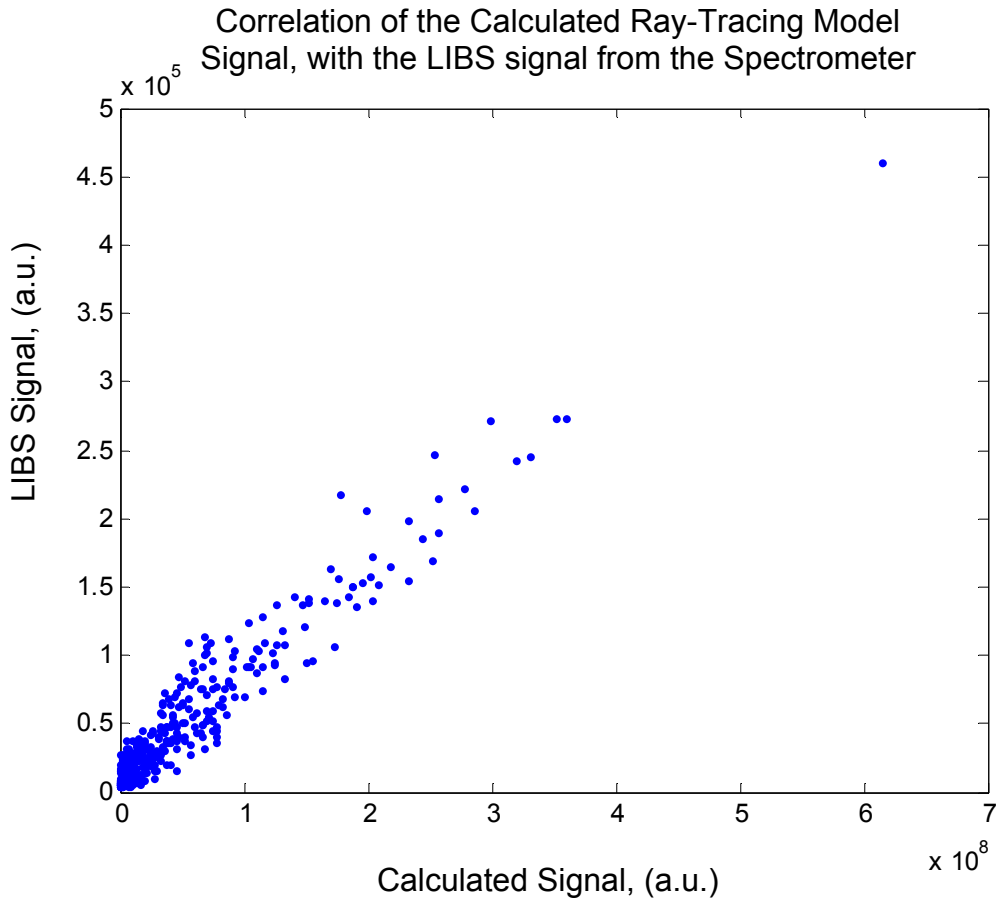


**Figure 7.12.** The results of the ray-tracing model show good correlation with the measured LIBS signal.

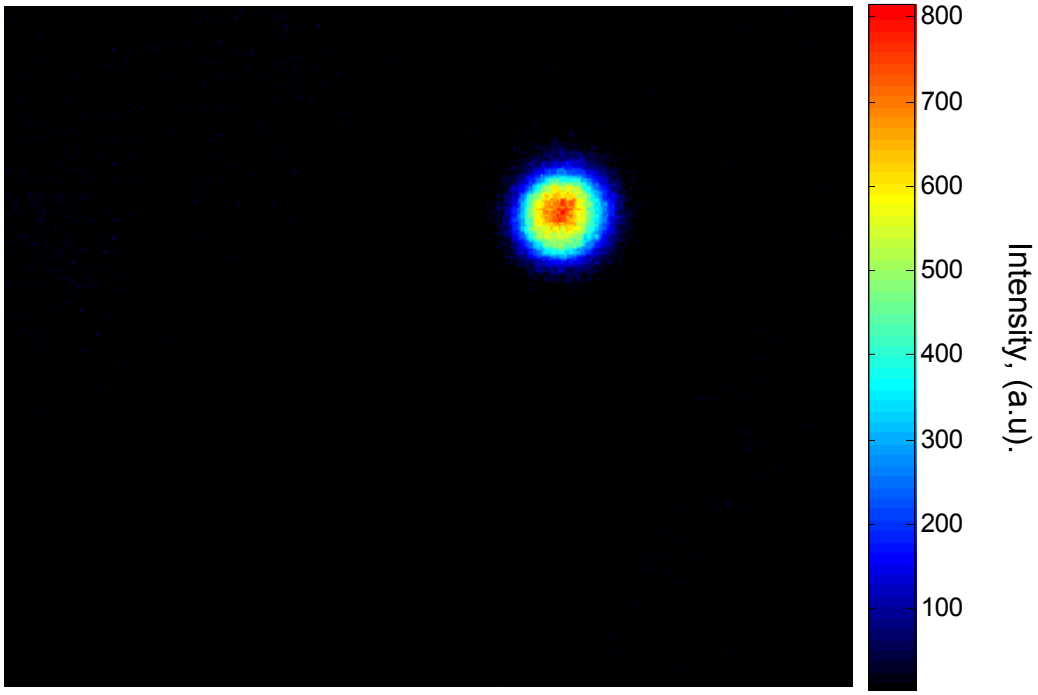


**Figure 7.13.** An image of a small particle plume. The size of the plume is similar to the inter-fiber spacing of the fiber bundle.

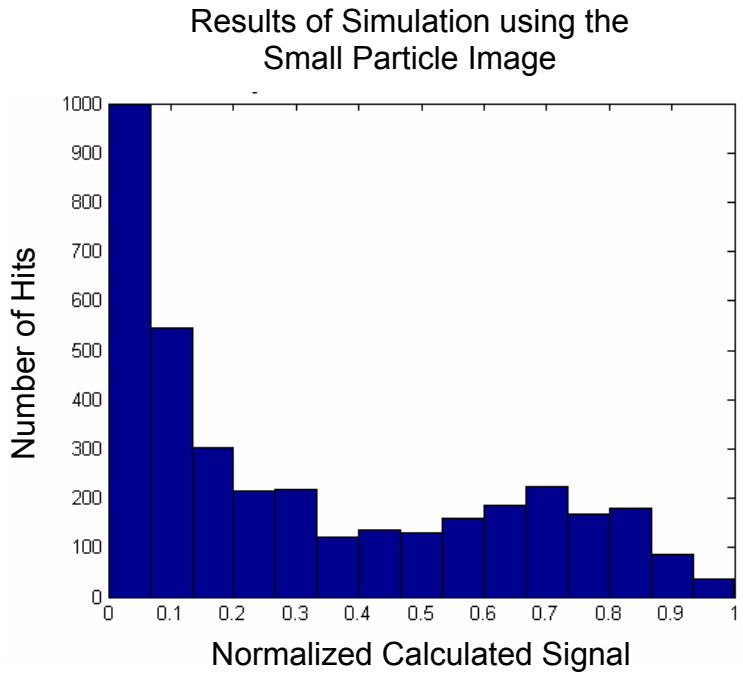


7.14(a)

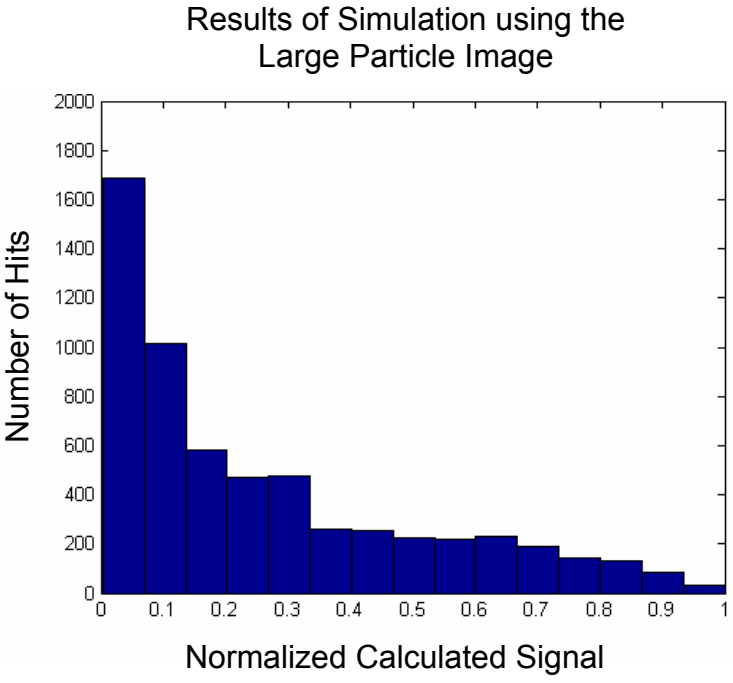


7.14(b)

**Figure 7.14.** The results of the simulation using small (a) and large (b) particle images. A bi-modal distribution is seen with the small image, which is not seen with the large image.

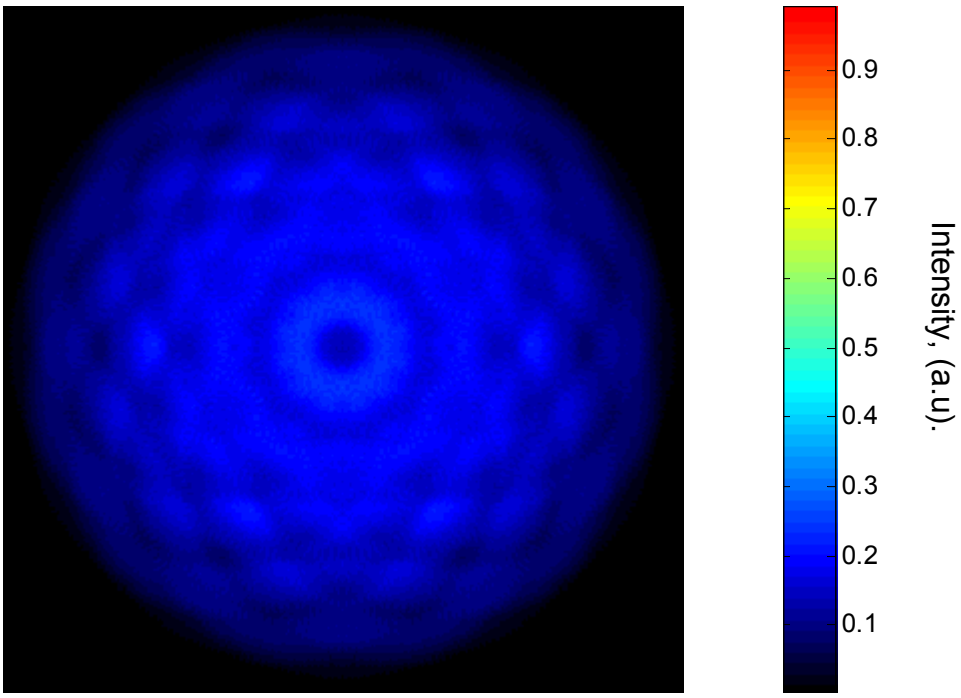


**Figure 7.15.** The focal volume away from the focal plane is more uniform, but the collection efficiency is also significantly reduced.

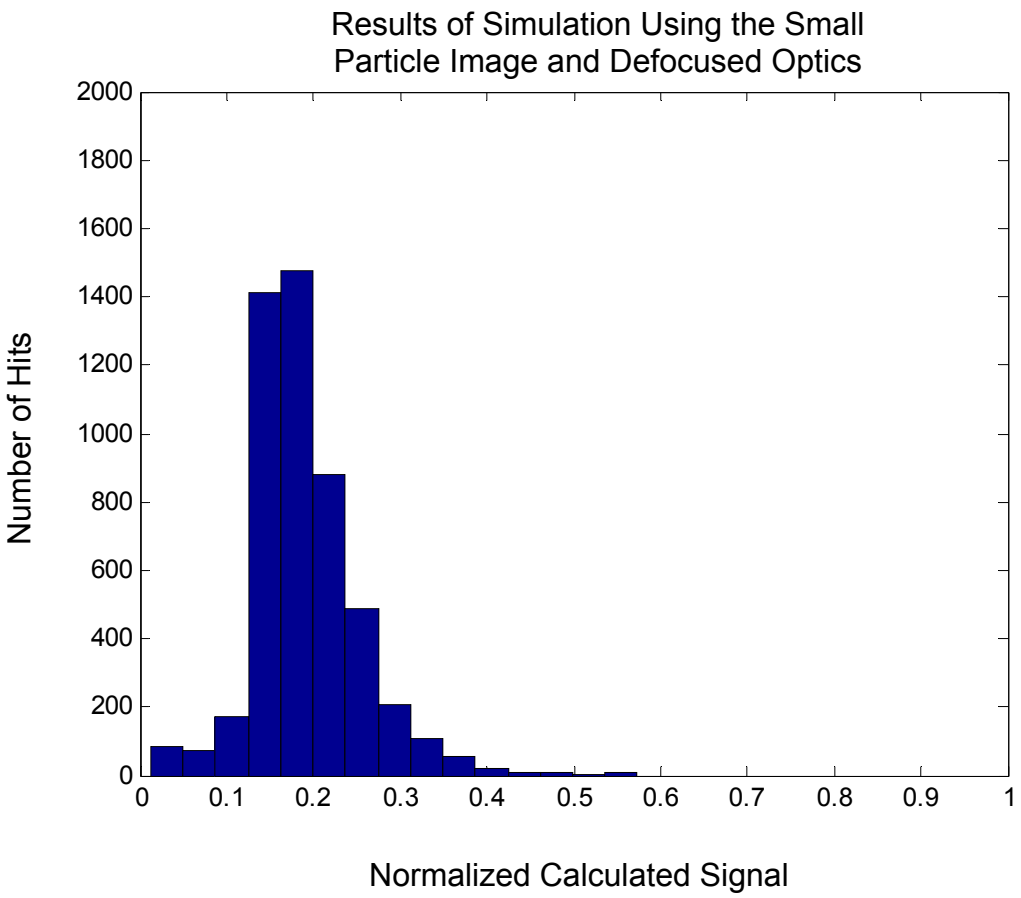


7.16(a)

**Figure 7.16.** By defocusing the optics, the error due to off-axis location of the particles is reduced, and the signal follows nearly a normal distribution, however the sensitivity is significantly reduced.

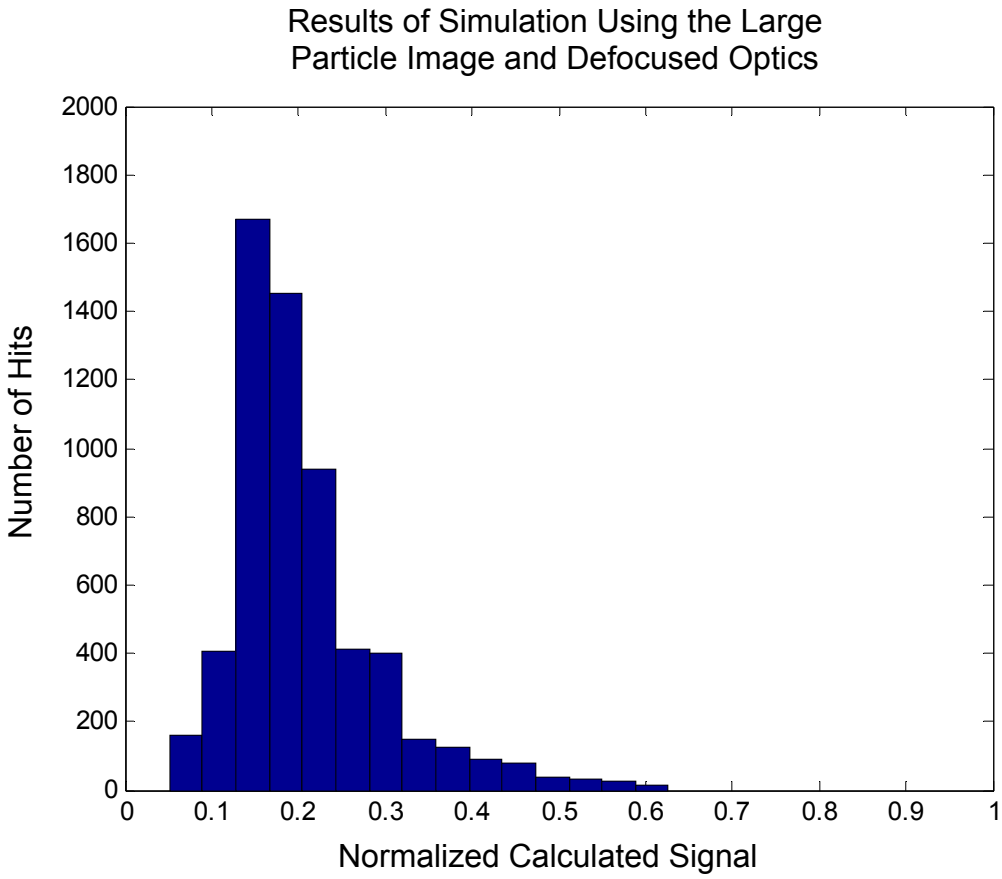


7.16(b)

**Figure 7.16.** (Continued)

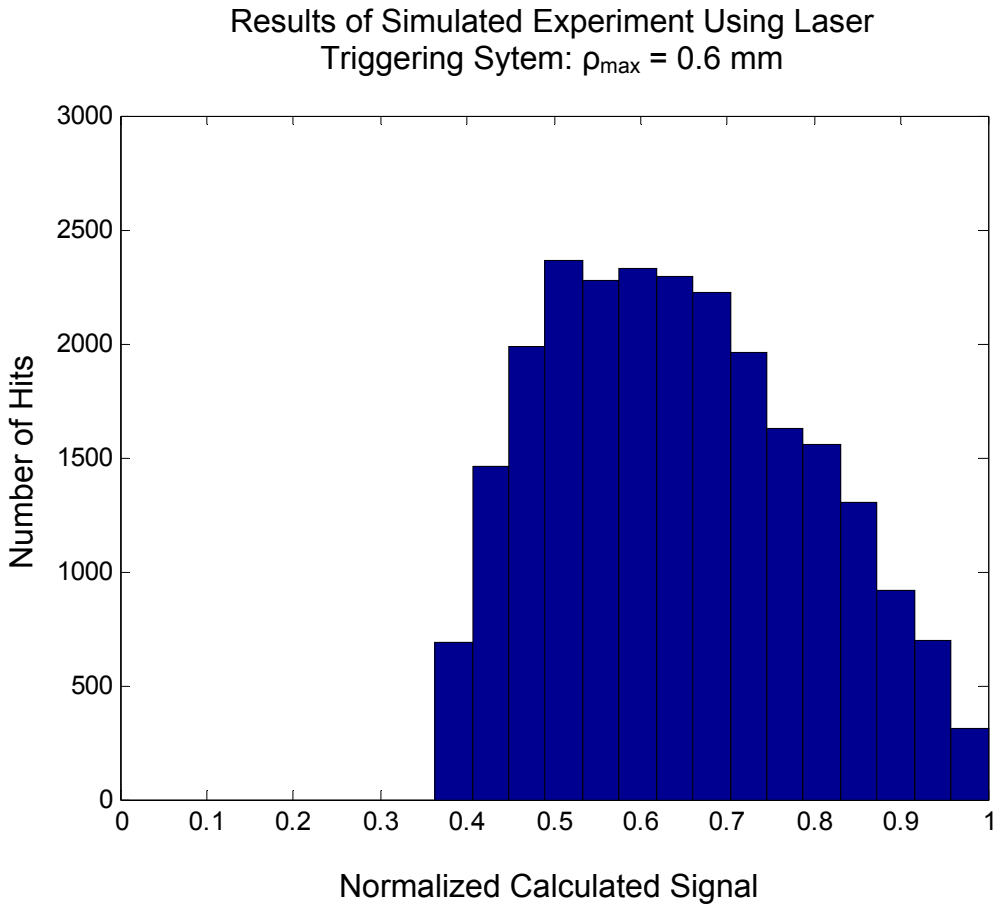


**Figure 7.17.** If the radial position of the particles is controlled with a laser triggering system, both low uncertainty and high sensitivity are achieved. In this simulation, the radial location was restricted to within 0.6 mm of the optical axis. The axial position was not restricted.

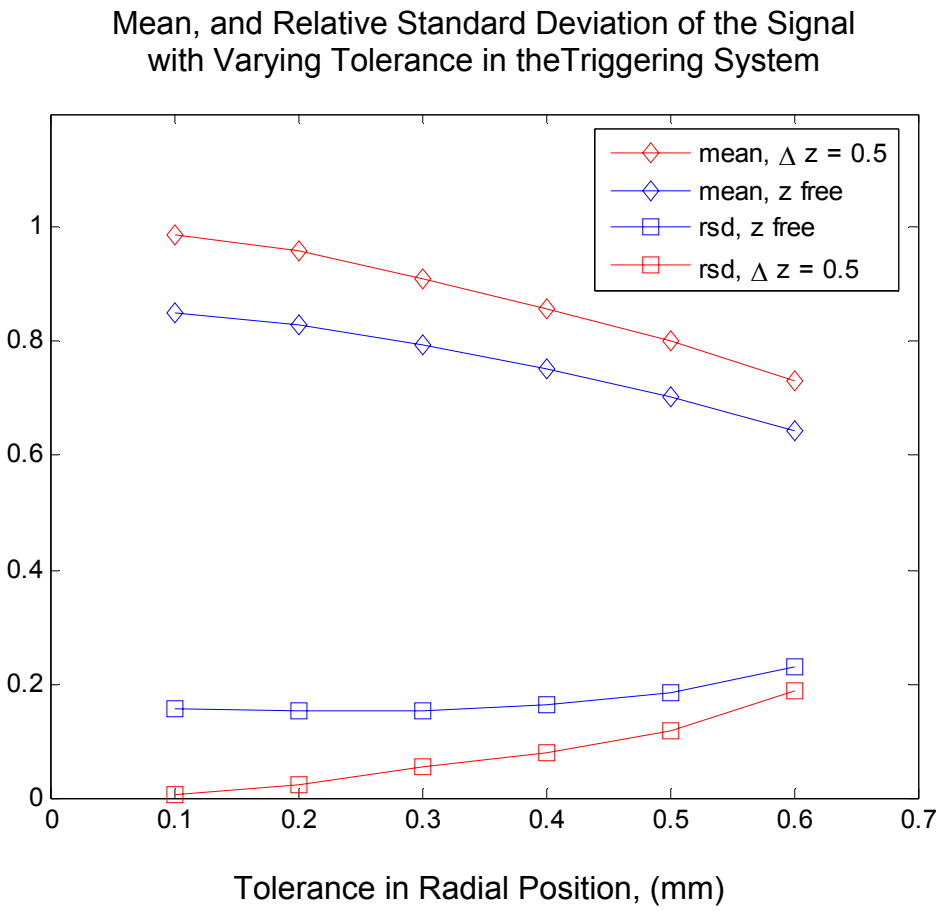


**Figure 7.18.** The mean and relative standard deviation of the signal distribution may be controlled by controlling the location of the particle. The blue curves correspond to the mean and relative standard deviation if the axial position is not controlled. For the red curves, the axial position is controlled to within ± 0.5 mm of the focal plane.

# 8. FUTURE WORK AND CONCLUSIONS

## 8.1 Future Work

There are many attractive qualities of the LIBS technique that make it a promising tool for aerosol measurements. Although the performance is currently inadequate for quantitative analysis, there is much room for improving the technique through several different approaches. The ultimate goals are to control the plasma formation and particle vaporization such that the particle is fully vaporized, that the state of the vaporized material (temperature and density) is repeatable, and that the optical system properly collects the light emitted from the particle material.

As discussed in this dissertation, the typical optical collection systems used in LIBS devices have not been adequately designed to collect light uniformly across the extent of the plasma. Significant improvement in the precision may be achieved by simply redesigning the optical system. For example, by demagnifying the plasma image, it can be fit entirely on the tip of a fiber bundle, or even a single fiber. However, there are significant design constraints on real systems that limit the effectiveness of this approach. Because of the limited numerical aperture of the optical fiber and spectrometer, there is a necessary trade-off between the size of the focal volume that may be collected and the total collection efficiency from that volume. Also, it is desirable to collect the LIBS signal in the backward direction along the laser axis, thus requiring only one optical access point to the sample. In this configuration, the need to separate the high-intensity laser beam from the broadband emissions presents a challenge for selecting appropriate optics. Furthermore, although collecting light from the entire plasma ensures that light from the entire particle plume is collected, it also results in more background plasma

emission being collected, increasing the signal noise. Therefore, if the location of the particle can be controlled, it may be beneficial to collect light from only the portion of the plasma where the particle is actually located. This would require the addition of a triggering system, but would have the effect of both reducing the uncertainty due to out-of-focus location and maximizing the collection efficiency from the particle.

Though not presented in this manuscript, initial efforts have been made to implement a laser-triggering system to reduce the uncertainty particle location. The proposed system is diagramed in Figure 8.1. In this case, a continuous wave (CW), frequency doubled, Nd:YAG laser is aligned with the plasma-forming laser with a dichroic mirror. Light from the CW laser is scattered by a particle passing through the beam and collected by a photomultiplier tube (PMT). The signal from the PMT is amplified and used to trigger a pulse generator, which in turn triggers the LIBS laser. The triggering system would control only the radial position of the particle. Therefore, a small tube or nozzle would be used to introduce the aerosol flow to the spark, limiting the axial position. A prototype of the triggering system was implemented. However, of the pulsed lasers available, none had to ability to both be triggered randomly and deliver sufficient energy to create a plasma. Once fully operational, it is realistic to expect that such a system would be sufficient to control the location of the particle to within several hundred microns in the radial direction and one millimeter in the axial direction. An important next step would be to complete and evaluate a functional LIBS device with a triggering system.

The laser triggering system would control the location of the particle at the moment that the pulsed laser is fired, however it is unclear what the optimal location of

the particle would be, as the motion and vaporization of the particle need to be accounted for. There are likely competing concerns that would need to be balanced. On the one hand, it is important to ensure that particle be fully vaporized. However, it may also be preferable to limit the length scale associated with the transport of the vaporized material away from the original particle to less than the length scale associated with gradients in plasma properties to ensure that the state of the vaporized material was uniform. Once a triggering system is developed, the initial location of the particle can be controlled, and the effects of vaporization and transport carefully studied.

**8.2 Conclusions**

The goal of the work presented has been to apply the technique of Laser-Induced Breakdown Spectroscopy to the diverse and important field of aerosol measurements. The potential for LIBS to detect and classify biological aerosols was demonstrated. It was proposed that LIBS may be used with a technique such as Laser-Induced Fluorescence to identify suspicious aerosols, and serve as a trigger for a more complicated and definitive technique. LIBS was also used to continuously monitor the ambient concentrations of several metals simultaneously, and the ability to measure the composition of individual particles may be useful for source apportionment of atmospheric particulate matter. After attempting these new applications of LIBS, it was discovered that the current performance of LIBS aerosol measurements limits it usefulness for these applications. It is likely that both the sensitivity and precision of the technique need to be improved before LIBS can have a significant impact in the field of aerosol measurements.

After learning the lessons from attempting the new applications, the fundamental aspects of aerosol measurements were investigated to identify sources of uncertainty, and methods of maximizing signal. The variation in the location of particles within the LIBS plasma was found to cause localized effects that contribute to the uncertainty of the technique. These effects are due both to the complicated process of particle vaporization and transport, and the non-uniform efficiency of the collection optics. The contribution of the optical effects was studied in detail, and the sources of uncertainty were identified and quantified through experiment and modeling.

The detailed understanding of the performance was an important step towards optimizing the performance of the LIBS technique, however there is still significant room for improvement. An essential step is to implement a triggering device so that particle location may be controlled. With specific design guidelines for the optical system, and the ability to control the particle location, there is great potential for improvement of aerosol measurements with LIBS. As the performance continually improves, it is expected that LIBS will find use in a variety of aerosol applications.

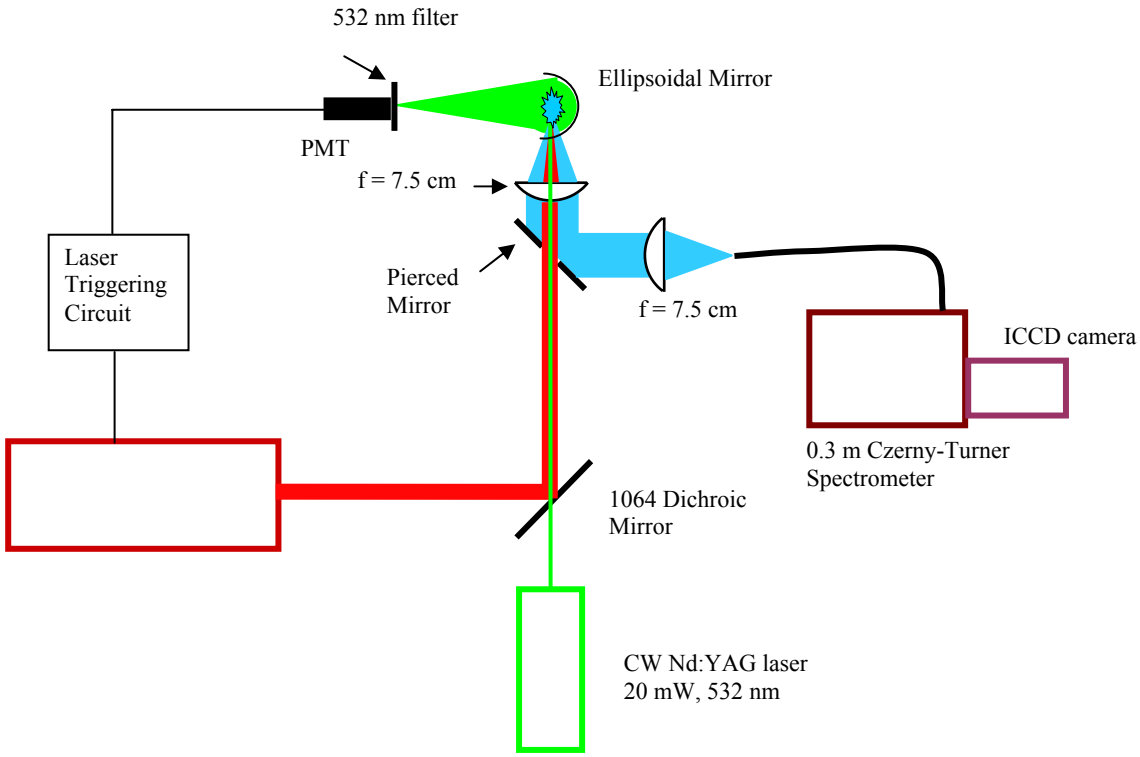


**Figure 8.1.** Schematic of a LIBS apparatus with a laser triggering system.